

University of Genoa

Faculty of Engineering
DICAT

Royal Institute of Technology of Stockholm

Department of Mechanics
Linné Flow Centre



Master's thesis

Symmetry Breaking of a Flexible Filament in a Pulsatile Flow

Supervisors: Prof. Alessandro Bottaro
Prof. Shervin Bagheri

Co-supervisor: PhD stud. Uģis Lācis

Author: Zaccaria Orlando

September 2013

Abstract

Fluid-structure interaction problems are very common in modern engineering and their solution is of crucial importance during the design phase in a broad variety of fields, from aeronautics, to civil engineering, to medicine.

This work focuses on the study of the interaction between a flexible filament and a pulsatile flow inside a two-dimensional channel. The system, even if symmetric in its initial conditions and in the ensuing forcing, can develop an asymmetric behaviour due to the interaction between its components; to quantify asymmetry we choose to observe the average angle during the flapping of the filament and the average flow through the channel during a pulsatile-flow time period.

The investigation is done through virtual experiments, i.e. simulating the system dynamics numerically. We use a modified version of the Fractional Step Method to solve the fluid dynamics in the domain, discretizing the equations on a staggered grid; the Immersed Boundary Method is adopted to take into account the presence of the filament and the interaction between the filament and the fluid.

An existing code has been modified and adapted to the new case of study, yielding two different types of solution, distinguished by the method through which the pulsatile flow is imposed: through velocity boundary conditions or through imposed pressure gradient together with periodic boundary conditions.

We find evidences of symmetry breaking in our case of study and we explore the space of parameters in order to better characterize the occurrence of symmetry breaking and its magnitude. We observe significant asymme-

Abstract

try both in the filament movement and in the average velocity induced in the channel.

We also make use of other techniques such as the Finite Time Lyapunov Exponent to further characterize the effect of the fluid-structure interaction on the flow inside the channel.

Finally, the effects of the filament together with the pulsatile flow are included in a simplified model in order to obtain a better comprehension of the dynamics of this coupled system.

Sommario

I problemi di interazione fluido-struttura sono molto comuni nell'ingegneria moderna e la loro soluzione è di cruciale importanza nella fase di progettazione in una grande varietà di campi, dall'aeronautica, all'ingegneria civile, fino alla medicina.

Questo lavoro riguarda lo studio dell'interazione fra un filamento flessibile e un flusso pulsante in cui è immerso, all'intero di un canale bidimensionale. Il sistema, benché simmetrico nelle sue condizioni iniziali e nelle sollecitazioni imposte successivamente, può sviluppare un comportamento asimmetrico a causa delle interazioni fra le sue componenti. Per quantificare l'asimmetria si è scelto di osservare l'angolo medio formato dal filamento durante il suo movimento e il flusso medio all'interno del canale durante un periodo del flusso pulsante.

La ricerca è stata svolta tramite esperimenti virtuali, ovvero simulando le dinamiche del sistema numericamente. Si è utilizzata una versione modificata del metodo *Fractional Step* per la soluzione della dinamica del fluido all'interno del dominio, discretizzato utilizzando una griglia *staggered*, e il metodo dei *Immersed Boundary* per tenere conto della presenza del filamento e della mutua interazione fra il filamento stesso e il fluido.

Un codice esistente è stato modificato e adattato al caso in studio, fino ad arrivare a due versioni differenti distinte dal modo in cui il flusso pulsante è generato, attraverso condizioni al contorno di velocità oppure attraverso un gradiente di pressione imposto insieme a condizioni al contorno di periodicità.

Si è verificato il manifestarsi di rottura della simmetria nel sistema og-

Sommario

getto dei nostri studi e lo spazio dei parametri è stato esplorato per caratterizzare il verificarsi di tale rottura e il suo ordine di grandezza. Si è osservata una asimmetria significativa sia per quanto riguarda il movimento del filamento, sia nel flusso medio all'interno del canale. Sono state inoltre utilizzate altre tecniche come i *Finite Time Lyapunov Exponent* per analizzare più a fondo gli effetti dell'interazione fluido-struttura sul flusso all'interno del canale.

Infine, gli effetti del filamento insieme al flusso pulsante sono stati semplificati e modellati per permettere una migliore comprensione della dinamica del sistema.

Chapter 1

Introduction

1.1 Aeroelasticity

Aeroelasticity is the science which studies the interactions among inertial, elastic, and aerodynamic forces. It was defined by Arthur Roderick Collar in 1947 as “the study of the mutual interaction that takes place within the triangle of the inertial, elastic, and aerodynamic forces acting on structural members exposed to an airstream, and the influence of this study on design” [1].

The classical theory of elasticity deals with the stress and deformation of an elastic body under prescribed external forces or displacements. The external loading acting on the body is, in general, independent of the deformation of the body. It is usually assumed that the deformation is small and does not substantially affect the action of external forces; in such a case we often neglect the changes in dimensions of the body and base our calculations on the initial shape. Even in problems of bending and buckling of columns, plates, or shells, either the external loading or the boundary constraints are considered as prescribed. The situation is different, however, in most significant problems of aeroelasticity: the aerodynamic forces depend critically on the attitude of the body relative to the flow. The elastic deformation plays an important role in determining the external loading

1.1. Aeroelasticity

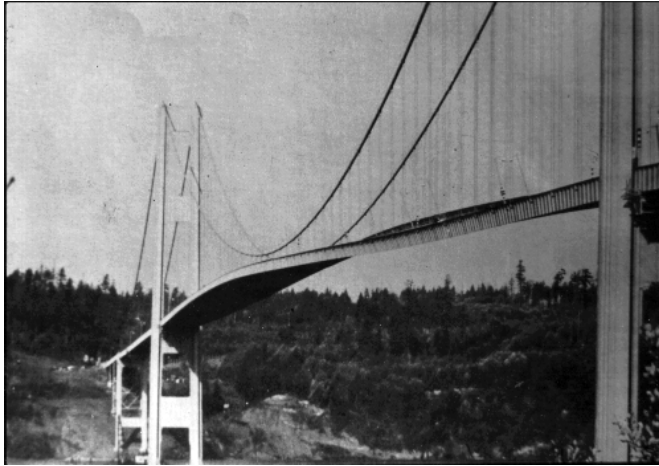


Figure 1.1: Picture of the first Tacoma Narrows Bridge showing the aeroelastic flutter in strong wind that will cause it to collapse. 1940.

itself. The magnitude of the aerodynamic force is not known until the elastic deformation is determined. In general, therefore, the external load is not known until the problem is solved. [2]

There are many scientific fields in which aeroelasticity is fully involved: aircraft designers are concerned with aerodynamic performance of an elastic aircraft, designers of bridges and skyscrapers need to know what the wind will be doing to their structures, designers of artificial heart valves and students of medicine want to know how blood flows in very flexible vessels, naturalists and environmentalists are interested in the locomotion of birds, fishes, and mammals, or the movement of leaves. Scientific study of these problems has to focus on flow in regions with deformable boundaries, and on the deformation of solids subjected to fluid loading, which varies with the deformation itself. This often results in unexpected dynamics that we would not see if we neglect the solid boundaries deformations.

The study of Aeroelasticity can be traced back to the 1920's by aeronautical engineers, but a big push in this field derives from the unexpected

failure of the Tacoma Narrows Bridge in 1940, as a result of aeroelastic flutter caused by a strong wind (fig. 1.1). The failure have been studied, among others, by von Karman [3] and Farquharson [4].

The numerical study of fluid–structure interaction problems began in the 1970’s [7] and since then included studies in aerospace engineering applications [5], in the biomedical field, in arteries [6] and heart valves [7] and in civil engineering applications [8]. Due to advances in computational power and numerical algorithms we are able to simulate increasingly complex problems. The main aspect involved in this kind of problems is computation of the dynamics of different physical domains (multiphysics) and their coupling with moving boundary conditions and meshes.

The case of study object of this thesis work is another problem in which the fluid-structure interaction is essential for an accurate study. The case of study will be explained in the next sections, while the method used to study it will be the object of the next chapter.

1.2 Case of study

The object of this thesis is the study of the interaction between one or more flexible filaments and a pulsatile flow confined in a two-dimensional channel. The case of study consists in three main components, the flexible filaments, the rigid channel walls to which the filaments are clamped, and a fluid inside the channel which is forced in a symmetric pulsatile flow. The main components are characterized by multiple properties, the importance of which in determining the final behaviour of the system will be studied in this work.

The properties that characterize every filament are:

- the length, called L_f
- the density, ρ_f
- the axial elastic stiffness, that defines the relationship between applied tension and axial elongation, K_{elas}

1.2. Case of study

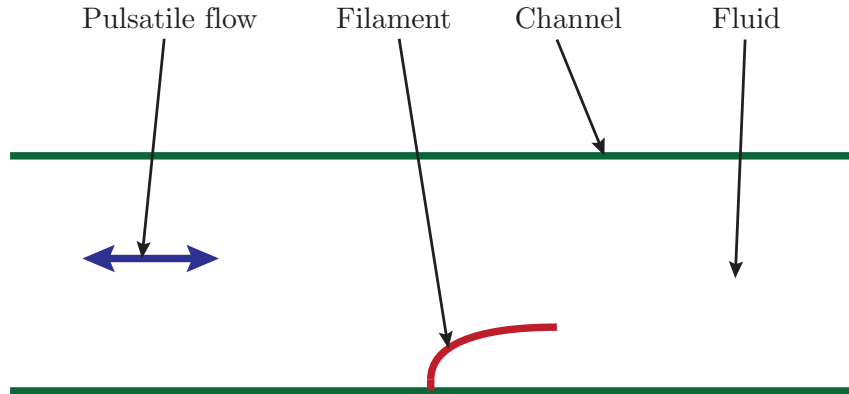


Figure 1.2: Case of study.

- the bending stiffness, that defines the relationship between applied momentum and the resulting curvature, K_{beam}

The channel properties and observables that can be defined are:

- the length (horizontally in fig. 1.2), L
- the height (vertically in fig. 1.2), $2h$
- whether or not the filament(s) are on both sides (top and bottom in fig. 1.2) of the channel
- the number of filaments on each side, N_f
- the distance between two filaments placed side by side, D_f
- the angle that the clamped end of the filament forms with the channel wall, θ_f

The fluid can be characterized by:

- the density, ρ_{flow}
- the dynamic viscosity, μ

As stated above the fluid is given a pulsatile forcing, i.e. it follows a reciprocating motion along the axial direction of the channel. This motion, neglecting the effects of the interaction with the filament, is characterized by:

- the duration of the time period, T_{flow} ;
- being symmetric, that is showing no difference between the the first half period and the second one;
- a velocity value that can be considered representative of the velocity magnitude of the flow.

The definition of the velocity value needs some more specifications. First of all an axial velocity is considered, neglecting any transversal component; then, it has to be taken into account that the velocity field inside the channel will be a function of time and vertical position of any cross-section of the channel. Let's first consider the spatial dependence; considering a cross-section of the channel, the velocity values will vary from the boundaries (where the viscosity of the fluid forces the velocity to vanish) to the center (where the velocity value will be in general non-zero); because of this, a spatial averaged value over a cross-section will be considered. Said spacial averaged value will still be non-constant over time, due to the pulsatile flow, and because of the flow symmetry it will vary between a minimum, negative value and a maximum, positive one, that will have the same absolute value.

The absolute value we just defined is the velocity value that we consider to characterize the pulsatile flow; it will be denoted as \bar{u}_{max} , where the overline symbolise the space averaging, while the subscript denotes the choice of the maximum value over time. This observable will be better defined in sec. 2.5.

1.3 Filament and flow interaction

Once the properties of the main components of our case of study are defined, such components need to be put together in order to form the

1.3. Filament and flow interaction

system we are interested in studying. If we keep on considering the existence of three main components, three mutual interactions between them can be defined and studied.

Two of them, namely filament – channel and channel – fluid, are very much easier to describe compared to the third one, that is filament – fluid, mainly due to fact that we consider the channel as non-deformable.

The filament – channel interaction can be reduced to the force and momentum the channel exerts to the clamped end of the filament. In this process said end will remain still, as desired, while the channel will suffer no modification due to its supposed infinite rigidity.

The channel – fluid interaction is similarly limited to the boundary region, where the presence of the walls forces the fluid to be locally still (no-slip condition), while, again, the channel suffers no modifications.

The filament – fluid interaction is the most interesting one; in this case a two-ways interaction exists, so that the filament position and local velocity modifies the flow properties, while the fluid motion influences the filament position and local velocity. This is due to the fact that the filament can exert forces on the fluid and vice-versa, and both of them respond to the applied forces being modified by them. This fact generates a peculiar loop, very well explained by a simple example. If we imagine that in a given moment the flow presence applies a given force in a specific point of the filament, the filament will be influenced by that force, specifically it will be probably accelerated in a particular direction. The acceleration will generate a movement of the filament, so that the displaced and moving filament will in turn apply a force back to the fluid; this in turn will modify the flow, at least locally. Now the flow is different from the one we considered at the beginning, and due to this difference it will not apply the same force on the filament, starting a potentially infinite loop.

There are configurations where the mutual interaction leads to a steady and stable configuration, but there also are several configurations (that do not need to be very complex) where said equilibrium is never reached, the problem of a flag in a steady wind being one of the best studied and known examples of a non-steady equilibrium. A flag immersed in a steady wind — or a filament in a 2D steady flow, fig. 1.3 — will, in some cases, start

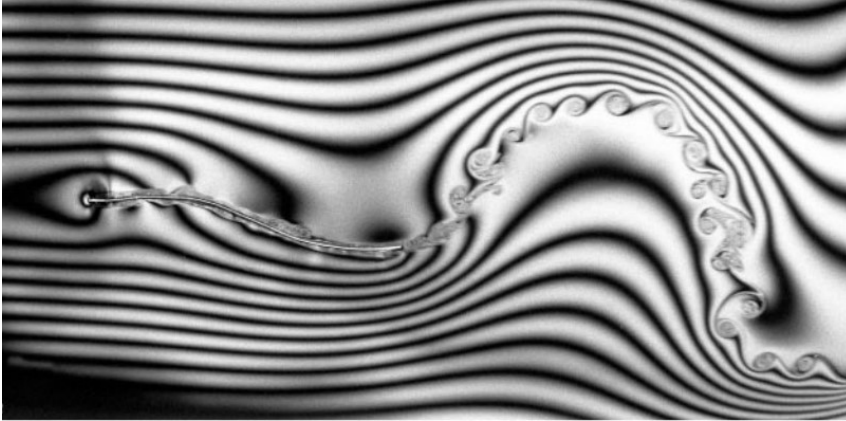


Figure 1.3: Filament flapping in a flowing soapfilm due to two-way interaction [9].

to flap due to the mutual interaction with the flow and the feedback loop that has just been described.

In our case of study, it is then very difficult to distinguish the influence of the fluid on the filament from the influence of the filament on the fluid; however, since the fluid is forced in a pulsatile flow while the filament is passive, the most obvious interaction is the one originating from the pulsatile flow; due to that, the filament will flap roughly in synchronization with the flow.

1.4 Symmetry breaking

Given these preconditions and given the symmetry of the pulsatile flow, in the presence of one or more passive filaments, a symmetric flow and a symmetric movement of the filaments are expected. This is not always the case: sometimes either the filament, the flow or both shows asymmetry in some form. This is not the place where we can analyse in which study-cases asymmetry arises, but it is interesting to describe which kind of asymmetry

1.4. Symmetry breaking

can be expected.

As for the filament, the asymmetry will show up in its flapping movement: as it flaps, the filament free-end (or any other point) can displace more towards one side than to the other, its average position over time can be displaced towards one side with respect to the filament clamped end, the filament can show a greater curvature towards one side, etc. As for the flow, if the pulsatile flow is forced by a pulsatile mass flow, the asymmetry would show up as a non-zero average pressure difference between the two sides of the channel; if the pulsatile flow is forced by a convenient pulsatile pressure gradient, the asymmetry would be more easily noticeable and would show up as a non-zero net flow over time in one direction.

These are the kinds of asymmetry we will look for in our system, the aim being to understand which are the properties of the system that allow a symmetry breaking, to explain how it happens and to analyse its effects.

Chapter 2

Method

The case of study object of this thesis work has not been realised experimentally; we have resorted to Computational Fluid Dynamics, that is taking advantage of numerical simulations.

Computational fluid dynamics, usually abbreviated as CFD, is a branch of fluid mechanics that uses numerical methods and algorithms to solve and analyse problems that involve fluid flows. The fundamental basis of almost all CFD problems are the Navier–Stokes equations, which define any single-phase (gas or liquid, but not both) fluid flow. These equations can be simplified by removing terms describing viscous actions to yield the Euler equations. Further simplification, by removing terms describing vorticity yields the full potential equations. Finally, for small perturbations in subsonic and supersonic flows (not transonic or hypersonic) these equations can be linearised to yield the linearised potential equations.

Historically, methods were first developed to solve the Linearised potential equations: two-dimensional (2D) methods, using conformal transformations of the flow about a cylinder to the flow about an airfoil were developed in the 1930s, while 3D Navier-Stokes equations solvers became available in the 1990s [10].

2.1. *The Navier-Stokes equations*

2.1 The Navier-Stokes equations

The Navier–Stokes equations, named after Claude-Louis Navier (1785 - 1836) and George Gabriel Stokes (1819 - 1903), describe the motion of fluid substances. These equations arise from applying Newton’s second law to fluid motion, together with the assumption that the stress in the fluid is the sum of a diffusing viscous term (proportional to the gradient of velocity) and a pressure term - hence describing viscous flow. The Navier–Stokes equations dictate not position but rather velocity. A solution of the Navier–Stokes equations is called a velocity field or flow field, which is a description of the velocity of the fluid at a given point in space and time. Once the velocity field is solved for, other quantities of interest (such as flow rate or drag force) may be found. The Navier–Stokes equations are nonlinear partial differential equations in almost every real situation. In some cases, such as one-dimensional flow and Stokes flow (or creeping flow), the equations can be simplified and rendered linear. The nonlinearity makes most problems difficult or impossible to solve and is the main contributor to the turbulence that the equations model. The nonlinearity is due to convective acceleration, which is an acceleration associated with the change in velocity over position. Hence, any convective flow, whether turbulent or not, will involve nonlinearity.

Together with supplemental equations (for example, conservation of mass) and well formulated boundary conditions, the Navier–Stokes equations can model fluid motion accurately; even turbulent flows seem (on average) to agree with real world observations. The Navier–Stokes equations assume that the fluid being studied is a continuum (it is infinitely divisible and not composed of particles such as atoms or molecules), and is not moving at relativistic velocities. At very small scales or under extreme conditions, real fluids made out of discrete molecules will produce results different from the continuous fluids modeled by the Navier–Stokes equations.

The derivation of the Navier–Stokes equations begins, as said, with an application of Newton’s second law: conservation of momentum (often alongside mass and energy conservation) being written for an arbitrary

portion of the fluid. A simplification of the resulting flow equations is obtained when considering an incompressible flow of a Newtonian fluid. The assumption of incompressibility rules out the possibility of sound or shock waves to occur; so this simplification is not useful if these phenomena are of interest. The incompressible flow assumption typically holds well also when dealing with a compressible fluid at low Mach numbers. Taking the incompressible flow assumption into account and assuming constant viscosity, the Navier–Stokes equations will read, in vector form:

$$\rho \left(\frac{\partial \mathbf{u}}{\partial t} + \mathbf{u} \cdot \nabla \mathbf{u} \right) = -\nabla p + \mu \nabla^2 \mathbf{u} + \mathbf{f}, \quad (2.1)$$

where \mathbf{u} is the velocity vector, p is the pressure, \mathbf{f} represents other body forces (forces per unit volume), such as gravity or centrifugal force, μ the (constant) dynamic viscosity of the fluid and ∇ is the derivative operator $\frac{\partial}{\partial x} + \frac{\partial}{\partial y} + \frac{\partial}{\partial z}$. \mathbf{u} and p are function of the spatial position, \mathbf{x} , and time, t .

Together with this equation, the continuity equation holds, which for incompressible flow reads:

$$\nabla \cdot \mathbf{u} = 0. \quad (2.2)$$

2.1.1 Non-dimensionalization of the Navier-Stokes Equations

Non-dimensionalization of the Navier–Stokes equations is the conversion of the Navier–Stokes equations to a form which is easier to use and reducing the number of free parameters in the problem to be studied. The non-dimensionalized Navier–Stokes equations are beneficial to use when posed with similar physical situations, that is problems where the only change are in the basic dimensions of the system. In addition to reducing the number of parameters, non-dimensionalized equations help to gain a greater insight into the relative size of various terms present in them. Following appropriate selection of scales for the non-dimensionalization process, this leads to identification of relative magnitude of the terms in the equations.

In order to non-dimensionalize (2.1), appropriate scales have to be chosen and applied to dimensional quantities as follows:

2.1. The Navier-Stokes equations

- length scale: L
- velocity scale: U_∞ , which is usually the velocity of the undisturbed flow
- time: L/U_∞
- pressure: $\rho_\infty U_\infty^2$, which is double the dynamic pressure of the undisturbed flow

This yields, asterisk indicating non-dimensional quantities:

$$\begin{aligned}
 \mathbf{x}^* &= \frac{\mathbf{x}}{L}, \\
 \mathbf{u}^* &= \frac{\mathbf{u}}{U_\infty}, \\
 t^* &= \frac{t}{L/U_\infty}, \\
 p^* &= \frac{p}{\rho_\infty U_\infty^2}.
 \end{aligned} \tag{2.3}$$

Substituting (2.3) into (2.1), the non-dimensionalized equations obtained are:

$$\frac{\partial \mathbf{u}^*}{\partial t^*} + \mathbf{u}^* \cdot \nabla \mathbf{u}^* = -\nabla p^* + \frac{1}{Re} \nabla^2 \mathbf{u}^* + \mathbf{f} \frac{L}{U_\infty^2}. \tag{2.4}$$

From now on when using these equations the asterisks will be omitted. If the additional body forces \mathbf{f} , mainly gravitational forces, can be neglected, (2.4) simplifies to:

$$\frac{\partial \mathbf{u}}{\partial t} + \mathbf{u} \cdot \nabla \mathbf{u} = -\nabla p + \frac{1}{Re} \nabla^2 \mathbf{u}. \tag{2.5}$$

Correspondingly, the conservation of mass reads:

$$\nabla \cdot \mathbf{u} = 0. \tag{2.6}$$

2.2 Numerical method

Since there is no analytical solution for (2.5), exception made for a few very simple cases, it is usually solved using a numerical code. In most of them the same basic procedure is followed.

- The geometry (physical bounds) of the problem is defined.
- The volume occupied by the fluid is divided into discrete cells (the mesh). The mesh may be uniform or non uniform.
- The physical modelling is defined, usually based on discretized Navier-Stokes equations.
- Boundary conditions are defined. This involves specifying the fluid behaviour and properties at the boundaries of the problem. For transient problems, the initial conditions are also defined.
- The simulation is started and the equations are solved iteratively as a steady-state or transient process.
- Finally a postprocessor is used for the analysis and visualization of the resulting solution.

Dealing with complex and turbulent flows, where the scale of small perturbations is many orders of magnitudes smaller than the domain scale asks for the mesh to be sufficiently fine in order to capture the smallest-scale dynamics. This can lead to the need of some form of simplification and modelling, in order to be able to run simulations using technically available computational power; most notably the Reynolds Averaged Navier-Stokes (RANS) approach and the Large Eddy Simulation (LES) approach can be cited.

The RANS method is based on the Reynolds decomposition, whereby an instantaneous quantity is decomposed into its time-averaged and fluctuating components. A model is used to take into account the effects of all fluctuating quantities. Doing this, a big computational power saving can

2.2. Numerical method

be exploited, at the cost of less accuracy. LES approach models only the smallest scales in the field (Kolmogorov scales) while simulating all other scales. This approach is computationally more expensive than the RANS method (in time and computer memory), but produces generally better results since the larger turbulent scales are explicitly resolved.

In our case another approach, known as Direct Numerical Simulation (DNS), is followed. A direct numerical simulation is a simulation in which the Navier–Stokes equations are numerically solved without any additional model. This means that the whole range of spatial and temporal scales must be resolved; this lead to the need of a comparatively very big number of cells or nodes. This approach, even if very demanding of computational resources, shows some very important advantages for our work. Recalling that our first goal is to look for symmetry breaking bifurcations in an apparently symmetric system, the main prerogatives a code should have in order to be apt for our investigation are best available accuracy and simplicity, so that the numerical approach can be ruled out from the possible causes of said symmetry breaking. DNS approach perfectly responds to these two requirements, being more accurate than the other methods and not generating possible spurious effects due to the models implemented models. Also, our domain is not overly complex, so that the simulations, while being still demanding, are not impossible to run on commercially available workstations.

2.2.1 The fractional step method

There are many methods to discretize and solve our model equations, and their description falls outside the present work. The method that will be described and used here is the “fractional step method”, first introduced independently by Chorin [11] and Temam [12] in 1968-69 and later improved by Perot [13]. The algorithm of the projection method is based on the Helmholtz decomposition of any vector field into a solenoidal part and an irrotational part. Typically, the algorithm consists of two stages. In the first stage, an intermediate velocity that does not satisfy the incompressibility constraint is computed at each time step. In the second, the pressure is

used to project the intermediate velocity onto a space of divergence-free velocity fields to get the next update of velocity and pressure.

Let's start with the non-dimensionalized Navier-Stokes equations together with the continuity equation for incompressible flows:

$$\begin{cases} \frac{\partial \mathbf{u}}{\partial t} + \mathbf{u} \cdot \nabla \mathbf{u} = -\nabla p + \frac{1}{Re} \nabla^2 \mathbf{u}, \\ \nabla \cdot \mathbf{u} = 0. \end{cases} \quad (2.7)$$

These differential equations need to be conveniently discretized in order to convert them into algebraic systems that will be then solved numerically.

We can conveniently define the matrices G , D , L and the function N as the discrete counterparts of the following operators:

$$\begin{aligned} \nabla p &\rightarrow Gp, \\ \nabla \cdot \mathbf{u} &\rightarrow Du - b_1, \\ \nabla^2 \mathbf{u} &\rightarrow Lu + b_2 Re, \\ \nabla \cdot (\mathbf{u}\mathbf{u}) &\rightarrow N(u). \end{aligned} \quad (2.8)$$

where the terms b_1 and b_2 depends on the choice of boundary conditions. The Navier-Stokes and mass-conservation equations (2.7) can be written as a semi-discrete system:

$$\begin{cases} \frac{\partial u}{\partial t} + N(u) = -Gp + \frac{1}{Re} Lu + b_2, \\ Du = b_1. \end{cases} \quad (2.9)$$

Using an explicit Adams-Bashforth scheme for the non-linear convective terms and an implicit Crank-Nicholson (trapezoidal) scheme for the diffusive terms, (2.9) can be discretized in time as:

$$\begin{cases} \frac{u^{n+1} - u^n}{\Delta t} + \frac{3}{2}N(u^n) - \frac{1}{2}N(u^{n-1}) = -Gp^{n+1} + \frac{Lu^{n+1} + Lu^n}{2Re} + b_2, \\ Du^{n+1} = b_1. \end{cases} \quad (2.10)$$

Manipulation of (2.10) leads to:

2.2. Numerical method

$$\begin{cases} \frac{u^{n+1}}{\Delta t} - \frac{Lu^{n+1}}{2Re} + Gp^{n+1} = \frac{u^n}{\Delta t} - \left[\frac{3}{2}N(u^n) - \frac{1}{2}N(u^{n-1}) \right] + \frac{Lu^n}{2Re} + b_2, \\ Du^{n+1} = b_1. \end{cases} \quad (2.11)$$

Defining:

$$A = \frac{I}{\Delta t} - \frac{L}{2Re} \quad ; \quad r^n = \frac{u^n}{\Delta t} - \left[\frac{3}{2}N(u^n) - \frac{1}{2}N(u^{n-1}) \right] + \frac{Lu^n}{2Re},$$

(2.11) becomes:

$$\begin{cases} Au^{n+1} + Gp^{n+1} = r^n + b_2, \\ Du^{n+1} = b_1. \end{cases} \quad (2.12)$$

The fully time and spatial discrete system can be written as an algebraic linear system:

$$\begin{bmatrix} A & G \\ D & 0 \end{bmatrix} \begin{bmatrix} u^{n+1} \\ p^{n+1} \end{bmatrix} = \begin{bmatrix} r^n \\ 0 \end{bmatrix} + \begin{bmatrix} b_2 \\ b_1 \end{bmatrix}. \quad (2.13)$$

It's not worthwhile to solve this system, instead its LU decomposition can be written. An appropriate approximation of (2.13) has been proposed [13]:

$$\begin{bmatrix} A & (\Delta t A)G \\ D & 0 \end{bmatrix} \begin{bmatrix} u^{n+1} \\ p^{n+1} \end{bmatrix} = \begin{bmatrix} r^n \\ 0 \end{bmatrix} + \begin{bmatrix} b_2 \\ b_1 \end{bmatrix}. \quad (2.14)$$

This is acceptable since $(\Delta t A)G = (I - \frac{\Delta t}{2Re}L)G \simeq G$.

It should be noted that only the momentum equations are approximated, while the discrete continuity equation remains unaltered, since it is important to satisfy it (and not create mass) if a realistic solution is desired.

The approximation given by (2.14) can be factored into the block LU decomposition

$$\begin{bmatrix} A & 0 \\ D & -\Delta t DG \end{bmatrix} \begin{bmatrix} u^* \\ p^{n+1} \end{bmatrix} = \begin{bmatrix} r^n \\ 0 \end{bmatrix} + \begin{bmatrix} b_2 \\ b_1 \end{bmatrix}, \quad (2.15)$$

and

$$\begin{bmatrix} I & \Delta t G \\ 0 & I \end{bmatrix} \begin{bmatrix} u^{n+1} \\ p^{n+1} \end{bmatrix} = \begin{bmatrix} u^* \\ p^{n+1} \end{bmatrix}. \quad (2.16)$$

This can be further simplified and written as:

$$\begin{aligned} Au^* &= r + b_2, \\ \Delta t DGp^{n+1} &= Du^* - b_1, \\ u^{n+1} &= u^* - \Delta t Gp^{n+1}. \end{aligned} \quad (2.17)$$

These equations represent the step that are actually performed in the numerical code used: the first equation generates an intermediate velocity u^* that does not satisfy the continuity constraint; the second is solved in order to get the new pressure field p^{n+1} ; in the third the pressure p^{n+1} is used to project the intermediate velocity u^* onto a space of divergence-free velocity fields to get the updated velocity field u^{n+1} .

2.2.2 Staggered grid

Initial attempts to solve the Navier–Stokes equations employed straight-forward centered finite differences for the spatial operators on a regular grid, with the pressure and velocity components being unknown at the corners of each cell. Two typical terms in the equations would then be discretized as follows in a uniform 2D grid:

$$\begin{aligned} \left[\frac{\partial p}{\partial x} \right]_{i,j} &\simeq \frac{p_{i+1,j} - p_{i-1,j}}{2\Delta x} \\ \left[\frac{\partial^2 u}{\partial y^2} \right]_{i,j} &\simeq \frac{u_{i,j-1} - 2u_{i,j} + u_{i,j+1}}{(\Delta y)^2} \end{aligned} \quad (2.18)$$

where the subscripts i, j denotes the point with the spatial index (i, j) at which the function is evaluated and Δx and Δy are the uniform spatial

2.2. Numerical method

cell sizes. This spatial discretization leads to an instability problem known as pressure checkerboard mode [14], that produces unphysical oscillations in the pressure field yielding to a checkerboard-like pressure distribution. The reason for this phenomenon is that the symmetric difference operator (2.18) will annihilate checkerboard pressures, i.e. pressures which oscillate between two different but fixed values on each grid line connecting the grid points. In fact, if we imagine to color our grid in a checkerboard pattern, we can soon discover that the pressure at the black vertices will not be related to the pressure at the white ones. The remedy for oscillatory or checkerboard pressure solutions can be to introduce a staggered grid in space (fig. 2.1), first introduced by Harlow and Welch in 1965 [15]. This means that the primary unknowns, the pressure and the velocity components, are sought at different points in the grid. In Cartesian coordinates the staggered grid offers the advantage of a strong coupling between the velocity components and the pressure, avoiding undesired oscillations in the pressure field.

Discretizing the terms $\partial p/\partial x$ and $\partial^2 u/\partial y^2$ on a staggered grid at a point with spatial indices $(i, j + \frac{1}{2})$ results in:

$$\begin{aligned} \left[\frac{\partial p}{\partial x} \right]_{i, j + \frac{1}{2}} &\simeq \frac{p_{i + \frac{1}{2}, j + \frac{1}{2}} - p_{i - \frac{1}{2}, j + \frac{1}{2}}}{\Delta x} \\ \left[\frac{\partial^2 u}{\partial y^2} \right]_{i, j + \frac{1}{2}} &\simeq \frac{u_{i, j - \frac{1}{2}} - 2u_{i, j + \frac{1}{2}} + u_{i, j + \frac{3}{2}}}{(\Delta y)^2} \end{aligned}$$

The staggered grid is convenient for many of the derivatives appearing in the equations: pressure and diffusion terms are very naturally approximated by central differences without interpolation, since the pressure nodes lie at cell centers and horizontal and vertical velocity components lie at the center of cell faces, but for the nonlinear terms it will be necessary to introduce averaging.

This kind of grid has a few side effects on the data structure: depending on the boundary conditions imposed, the computational domain of pressure and velocity fields may vary (fig. 2.2).

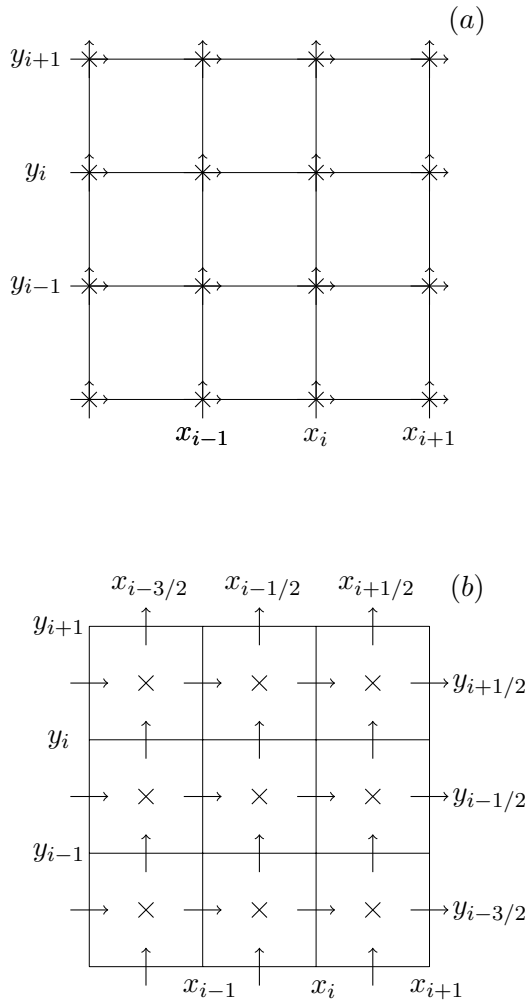


Figure 2.1: Colocated (a) and staggered (b) grid. x -velocity component is evaluated at \leftarrow , y -velocity component at \uparrow , whereas pressure at \times .

2.2. Numerical method

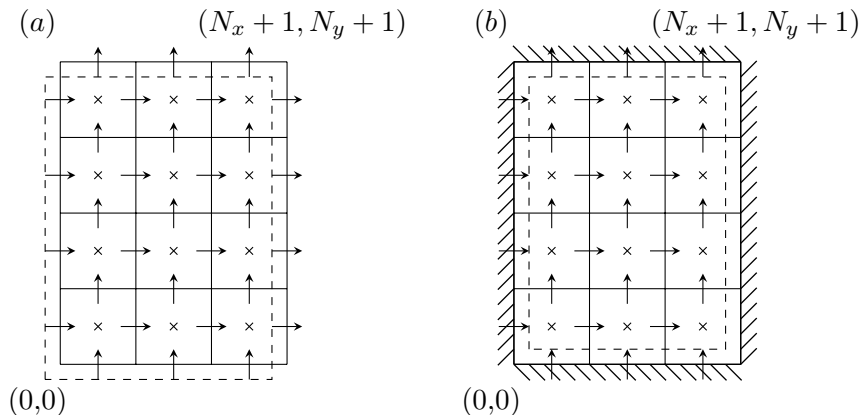


Figure 2.2: Staggered grid with periodic (a) and Dirichlet boundary conditions (b). The dashed line border the computational domain.

2.2.3 Boundary conditions

In (2.8) boundary terms appeared. To understand why they do it is useful to look at the computational domain, which is the whole set of grid nodes at which variables are unknown. In fig. 2.2 two examples are given: in the left case, periodic boundary conditions are imposed, so that the computational domain corresponds to the whole grid exception made for the last row and column, where velocities are considered to be known, being imposed to be equal to the value in the first row and column; in the right one, imposing Dirichlet boundary conditions (for example to enforce a no-slip condition at solid boundaries), the computational domain does not contain nodes on boundaries, where the velocities are known and their value is set equal to zero. Due to the specific structure of the Cartesian staggered grid, only velocity needs boundary conditions, pressure values being always inside the computational domain.

In the present work, mainly two types of boundary conditions will be used: imposed boundary conditions (that is inhomogeneous Dirichlet conditions) and periodic boundary conditions.

Usually at inlets the velocity of the fluid is known, so it is convenient to use it as a boundary condition:

$$\mathbf{u}|_{\partial\Omega} = f(x, y \in \partial\Omega),$$

where $\partial\Omega$ denotes the boundaries of the domain and \mathbf{f} gives the imposed boundary values for every point of the boundary.

These conditions lead to a non-zero boundary condition vector in the numerical model. Dirichlet boundary conditions are also used, as stated earlier, to enforce no-slip conditions at solid boundaries, giving raise to boundary terms involving wall absolute velocity (in particular a non-moving wall causes homogeneous boundary conditions, thus an empty boundary vector).

Periodic boundary conditions are defined so that the velocity values of one part of the boundaries will be imposed to be equal to those on the corresponding part. In our case, these two parts will be the left side and the right side of the channel. In this case the condition would read:

$$\mathbf{u}(-L/2, y) = \mathbf{u}(L/2, y),$$

L being the channel length and $x = 0$ being in the middle of the channel.

2.2.4 The Immersed Boundary Method

Having discussed the numerical implementation of the Navier-Stokes equations and their spatial discretization, we will now move to the problem of simulating the filament and its two-way interaction with the fluid. The method we will use is known as Immersed Boundary Method (IBM) and it has been first introduced by Peskin [7] who used it to simulate blood flow interacting with flexible heart-valves. Ever since, it has been used in a wide variety of applications where complex geometries and immersed elastic membranes or structures are present.

The Immersed Boundary Method uses an Eulerian grid for the fluid region, while it represents the immersed surface with a set of Lagrangian points that follow the surface in its movement. The Eulerian grid does not

2.2. Numerical method

need to be in specific relation with the Lagrangian one, due to the fact that the interactions between fluid and immersed boundary are managed through a discrete delta function that overcome the non-correspondence between Eulerian and Lagrangian points. At every time step the code needs to simulate the fluid-surface interaction in both ways: the surface applies a force to the fluid due to its position and its deformation with respect to its original shape; on the other hand, since the immersed boundary is in contact with the surrounding fluid, its velocity must be consistent with the no-slip boundary condition, thus the immersed boundary moves at the local fluid velocity.

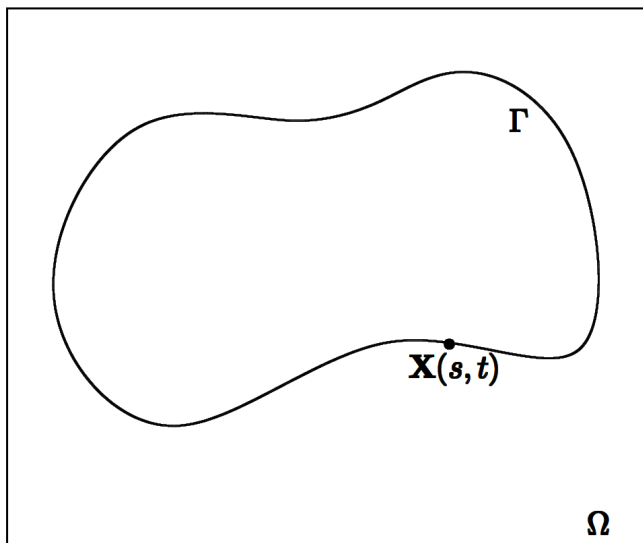


Figure 2.3: Example immersed boundary curve, Γ , described by the function $\mathbf{X}(s, t)$, immersed in a fluid-filled region Ω .

Calling Γ an immersed boundary (fig. 2.3), this results in the following

set of equations [16]:

$$\mathbf{F}(s, t) = A_f \mathbf{X}(s, t), \quad (2.19)$$

$$\mathbf{f}(\mathbf{x}, t) = \int_{\Gamma} \mathbf{F}(s, t) \delta(\mathbf{x} - \mathbf{X}(s, t)) ds, \quad (2.20)$$

$$\begin{cases} \frac{\partial \mathbf{u}}{\partial t} + \mathbf{u} \cdot \nabla \mathbf{u} = -\nabla p + \frac{1}{Re} \nabla^2 \mathbf{u} + \mathbf{f}, \\ \nabla \cdot \mathbf{u} = 0 \end{cases}, \quad (2.21)$$

$$\frac{\partial \mathbf{X}(s, t)}{\partial t} = \mathbf{u}(\mathbf{X}(s, t), t) = \int_{\Omega} \mathbf{u}(\mathbf{x}, t) \delta(\mathbf{x} - \mathbf{X}(s, t)) dx, \quad (2.22)$$

where lower-case letters are used for Eulerian variables and upper-case letters for Lagrangian ones; $\mathbf{X}(s, t)$ is the vector function giving the location of points on Λ as a function of arclength s and time t ; \mathbf{f} is the forcing term which serves to model the effects of the boundary; \mathbf{F} is the force applied by the boundary to the fluid. A_f is the force generation operator and it is problem dependent: it depends on the structure and properties of the membrane.

These equations closely represents the basic steps of the immersed boundary method we described. Equation (2.19) calculates the force that the boundary curve applies due to its current configurations; equation (2.20) spreads said force, defined on the Lagrangian point, to the nearby Eulerian point through the discrete delta function δ ; equation (2.21) are the well known Navier-Stokes and continuity equations that solve the flow to which the forcing term \mathbf{f} just obtained is applied; equation (2.22) interpolate the velocity from the Eulerian field to the Lagrangian one in order to get a velocity vector on each point of the membrane.

The discrete delta function has to satisfy a set of properties in order to be suitable for our scope. The discrete delta function that will be used here is the one proposed by Roma et al. [17], which has the size of its support equal to three mesh widths in each space direction, while previous immersed boundary computations have used delta functions whose support was four mesh widths in each direction.

2.3. Filament governing equations

2.3 Filament governing equations

The A_f operator was defined in the previous section as a problem dependent operator: it enforces the structure and properties of the immersed boundaries that need to be studied. In our case, the filament is considered as elastic (it reacts to an axial stretch) and flexible (it can bend, and when doing so a restoring force is generated). Also it is clamped at one end: the clamping condition will be enforced by virtually pinning the first few point to their original position. A curvilinear coordinate s is used to specify the position along the filament; s is the arclength.

Beginning with the elastic force, we can consider every small section of the filament as a Hooke's spring, of given stiffness K_{elas} ; that is, we assume that the material behaves like a fibre under elastic tension, so that the force it generates (per unit s) is given by: [16]

$$\mathbf{F}_s(s, t) = \frac{\partial}{\partial s}(T(s, t)\boldsymbol{\tau}(s, t)), \quad (2.23)$$

where $T(s, t)$ is the tension and $\boldsymbol{\tau}(s, t)$ is the tangent unit vector to the boundary at the point $\mathbf{X}(s, t)$. The tangent unit vector is defined as:

$$\boldsymbol{\tau}(s, t) = \frac{\frac{\partial \mathbf{X}}{\partial s}}{\left\| \frac{\partial \mathbf{X}}{\partial s} \right\|}. \quad (2.24)$$

Since the initial straight position is considered to be unstressed, then $\left\| \frac{\partial \mathbf{X}}{\partial s} \right\| - 1$ represents the strain. As stated before, we will consider an elastic filament subject to Hooke's law, so that the tension is proportional to the strain, i.e.

$$T(s, t) = K_{elas} \left(\left\| \frac{\partial \mathbf{X}}{\partial s} \right\| - 1 \right). \quad (2.25)$$

The elastic stiffness K_{elas} is chosen so that the filament is inextensible: it must be large enough so that the force exerted by the fluid only generates negligible elongations.

The bending force of the filament is computed following the method of Zhu and Peskin [18], based essentially on the principle of virtual work. First the bending energy is defined as:

$$E_b = \frac{1}{2} K_b \int \left| \frac{\partial^2 \mathbf{X}(s, t)}{\partial s^2} \right|^2 ds, \quad (2.26)$$

so that the bending force is:

$$\mathbf{F}_b = -\frac{\partial E_b}{\partial \mathbf{X}}. \quad (2.27)$$

This is numerically discretized as:

$$E_b = \frac{1}{2} K_b \sum_{m=2}^{n_f-1} \left[\frac{|\mathbf{X}_{m+1} - 2\mathbf{X}_m + \mathbf{X}_{m-1}|^2}{(\Delta s)^4} \right] \Delta s \quad (2.28)$$

and on the lagrangian point l we have:

$$(\mathbf{F}_b)_l = \frac{K_b}{(\Delta s)^4} \sum_{m=2}^{n_f-1} (\mathbf{X}_{m+1} - 2\mathbf{X}_m + \mathbf{X}_{m-1}) (-\delta_{m+1,l} + 2\delta_{m,l} - \delta_{m-1,l}), \quad (2.29)$$

where $\delta_{m,l}$ is the Kronecker symbol, its value being 1 if $m = l$ and 0 otherwise.

The clamped end is kept in its position by a virtual spring that connects every ‘‘clamped’’ point to its original position, so that:

$$\mathbf{F}_t(i) = -K_{targ}(\mathbf{X}(i, t) - \mathbf{X}_t(i - t)), \quad \text{for } i = 1, \dots, n_{targ}, \quad (2.30)$$

where the index i denotes a points in the discretized filament, n_{targ} is the number of point that are considered pinned in order to enforce the clamping condition and K_{targ} is the spring stiffness, its values being chosen so that the displacement of the targeted points from the initial position is negligible.

If the filament is considered to have mass, then an inertial force will exist:

$$\mathbf{F}_i(s, t) = -\rho_f \mathbf{a}(s, t) \quad (2.31)$$

2.4. Numerical implementation

\mathbf{F}_i being the force per unit length, ρ_f the linear density of the one dimensional filament and \mathbf{a} its local acceleration. In the code, this is implemented my means of a second fictitious filament that is linked by stiff springs to the first one. While the first one interact with the fluid, the second one does not; instead, they interacts between each other so that the first one makes the second one move following its movement; the second one, on the other hand, applies to the first one the forces that are due the real filament inertia.

If we add to the acceleration of the second filament another constant term in the right direction we can also take into account and model buoyancy effects. In our work buoyancy is always considered to be zero.

2.4 Numerical implementation

All the things that have been defined in the previous sections have to be implemented into a code that will be executed by one or more workstations. The code is written in the *MATLAB* programming language, so that it will be executed in the MATLAB numerical computing environment [20]. The code used for this work has been modified starting from the existing code used by Bagheri, Mazzino and Bottaro [21].

2.5 Velocity driven code

Having explained the ways we can impose boundary conditions in sec. 2.2.3, now we need to impose the right ones in order to generate the desired pulsatile flow of period T and characteristic velocity \bar{u}_{max} (see sec. 1.2).

Referring to fig. 2.4 and its Cartesian coordinates, we can now better define \bar{u}_{max} as

$$\bar{u}_{max} = \max \left(\frac{1}{2h} \int_{-h}^h u(x, y, t) dy \right),$$

which is obviously constant with x because of the incompressibility of the flow.

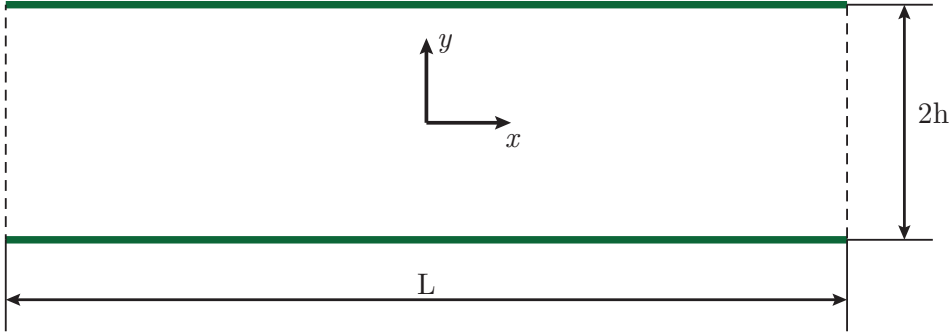


Figure 2.4: Representation of the channel with its dimensions and coordinates system.

In the first place, two Dirichlet conditions had been imposed both at the inlet and at the outlet of the channel; they were identical to each other and consisted in two parabolic profiles modulated in time by a sine function and scaled with \bar{u}'_{max} which will be the resulting velocity magnitude:

$$\begin{aligned} u(-L/2, y, t) = u(L/2, y, t) &= \frac{3}{2}\bar{u}'_{max} \left(1 - \frac{y^2}{h^2}\right) \sin\left(\frac{2\pi t}{T}\right) \\ v(-L/2, y, t) = v(L/2, y, t) &= 0 \end{aligned} \quad (2.32)$$

This leads to the desired value of \bar{u}_{max} :

$$\begin{aligned} \bar{u}_{max} &= \max\left(\frac{1}{2h} \int_{-h}^h \frac{3}{2}\bar{u}'_{max} \left(1 - \frac{y^2}{h^2}\right) \sin\left(\frac{2\pi t}{T}\right) dy\right) = \\ &= \frac{1}{2h} \int_{-h}^h \frac{3}{2}\bar{u}'_{max} \left(1 - \frac{y^2}{h^2}\right) dy = \frac{1}{2h} \left(\frac{3}{2}\bar{u}'_{max} 2h + \frac{3}{2h^2}\bar{u}'_{max} \frac{2h^3}{3}\right) = \\ &= \bar{u}'_{max} \end{aligned}$$

The parabolic profile is the profile that builds up in a steady stream inside a channel; due to the pulsatile flow, it turns out that the parabolic profile is not the one that would develop in a very long channel. This lead

2.5. Velocity driven code

to the fact that it is necessary to simulate a very long channel in order to have a central zone in which the flow is not affected by the inlet/outlet areas. The result of a simple channel simulation is shown in fig. 2.5, where the black lines are vorticity contour-lines; the presence of vorticity due to the inlet/outlet areas is an unwanted effect of the choice of the parabolic profile and clearly affects the central zone of the channel.

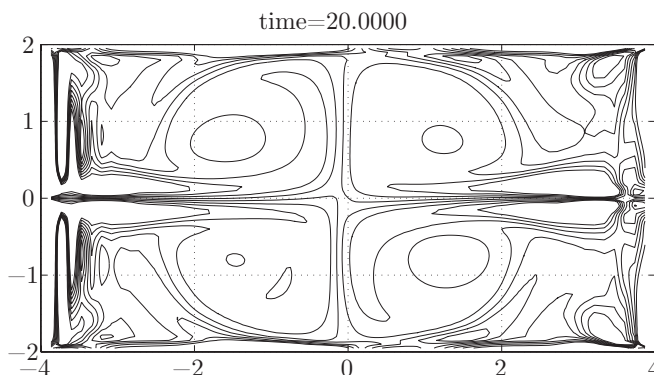


Figure 2.5: Unwanted vorticity due to the inlet and outlet velocity profiles. Black lines are vorticity contour-lines. $Re = 200$.

After some tests with channels of different lengths, measuring the velocity profiles in the central section as a function of time, it appeared clear not only that the velocity profile that develops is not parabolic, but also that it cannot be represented as some kind of profile multiplied a sine function over time. In fig. 2.6 the velocity profiles have been plotted every 1/4th of period, for a long channel at $Re = 200$.

2.5.1 Velocity profile generation

Our goal is now to generate a profile that is as similar as possible to the one that would be found in an undisturbed pulsatile flow in a channel. To do this, we will, prior to start the actual simulation, simulate a long and empty channel, to obtain the a set of velocity profiles (at $x = 0$, center of this long

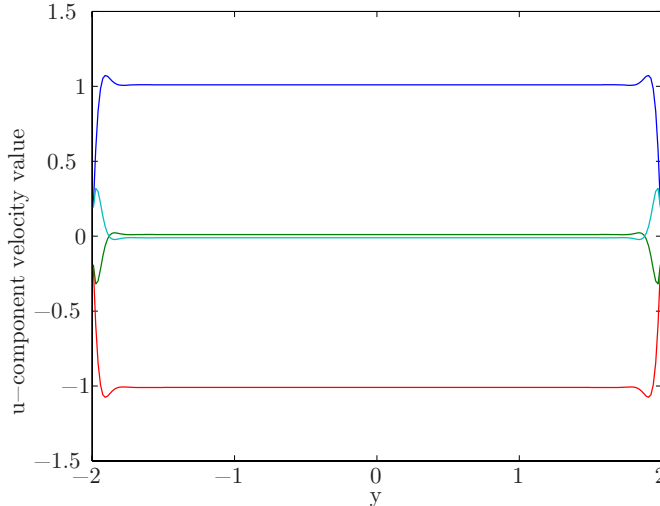


Figure 2.6: Velocity profiles for $t/T=0.25$ (blue), $t/T=0.5$ (green), $t/T=0.75$ (red), $t/T=1$ (light blue), $L = 8$, $h = 2$, $Re = \frac{\bar{u}_{max} h \rho_{flow}}{\mu} = 200$

channel) over time. In order not to capture transient effects, the velocity profiles in $x = 0$ are recorded and, after every pulsatile period, compared to the corresponding ones of the period before, waiting enough time so that they do not differ more than a certain threshold. If this happens, the velocity profile for every time-step of the last pulsatile period is saved and used as inlet and outlet boundary conditions. The set of values that will be saved and used will be denoted:

$$u_j^k \quad j \in [1, ny], \quad k \in [1 : nT],$$

where ny is the number of nodes in y direction and nT is the number of time-steps contained in a pulsatile time period, so that:

$$nT = \frac{T}{\Delta t}.$$

This method worked very well for reducing (almost eliminating) vorticity in inlet and outlet zone (fig. 2.7, same parameters as fig. 2.5), but does

2.5. Velocity driven code

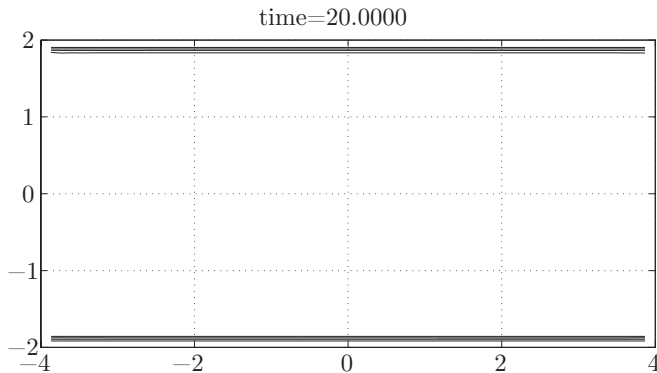


Figure 2.7: No unwanted vorticity outside the boundary layer. Black lines are vorticity contour-lines. $Re = 200$.

not guarantee the symmetric pulsatile flow we need. First of all, it does not guarantee that the velocity profiles of the first half of the pulsatile period are the same in absolute value compared to the ones of the second half, due to persistent transient effects, even if small. This can be a problem, since minor differences could generate symmetry breaking that would not be interesting for our investigation. Also, for very high Reynolds number it has been seen that the velocity profile can show some little asymmetry, over y . To enforce symmetry the velocity profiles set is modified as follows:

$$\bar{u}_j^k = \begin{cases} \frac{1}{4} \left(u_j^k + u_{ny-j+1}^k - u_j^{k+\frac{nT}{2}} - u_{ny-j+1}^{k+\frac{nT}{2}} \right), & 1 \leq k \leq \frac{Nt}{2}, i \in [1, ny], \\ \frac{1}{4} \left(u_j^k + u_{ny-j+1}^k - u_j^{\frac{nT}{2}-k} - u_{ny-j+1}^{\frac{nT}{2}-k} \right), & \frac{Nt}{2} \leq k \leq nT, i \in [1, ny]. \end{cases}$$

This mostly eliminates vorticity outside the filaments zone (fig. 2.7) and guarantees a pulsatile flow with no net flow, with two semi period which are exactly one the opposite of the other and with no asymmetries along y , by construction. Since the velocity profile does not depends on any filament properties nor on the number of filaments that are simulated, once obtained it can be used for other simulations, saving computational time.

2.6 Grid and convergence study

To test the convergence of the code, four different grids have been tested, varying the value of the minimum distance between nodes between $1/20$ and $1/80$. The channel has been simulated with a single flexible filament clamped on the bottom side; the pulsatile flow was characterized by a time period of 1, $Re = 200$ and $\bar{u}_{max} = 1$. The angle formed by the free-end of the filament with respect to the clamping point and the bottom wall of the channel have been measured in four different simulations, with grid spacing of $1/20$, $1/40$, $1/60$, $1/80$.

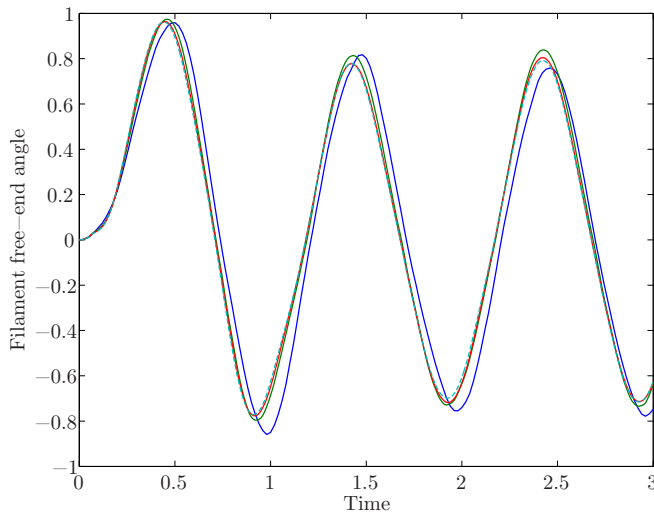


Figure 2.8: Convergence study for various grid spacings: $1/20$ (blue), $1/40$ (green), $1/60$ (red), $1/80$ (light blue, dashed).

The results are plotted in fig. 2.8 and, with better details, in fig. 2.9; in both of them different grid spacings are represented in different colors: $1/20$ (blue), $1/40$ (green), $1/60$ (red), $1/80$ (light blue, dashed).

Taking the results of the finest grid ($1/80$) as a reference, we calculated the difference between the reference and the results of other grid spacings,

2.7. Comparison with previous works

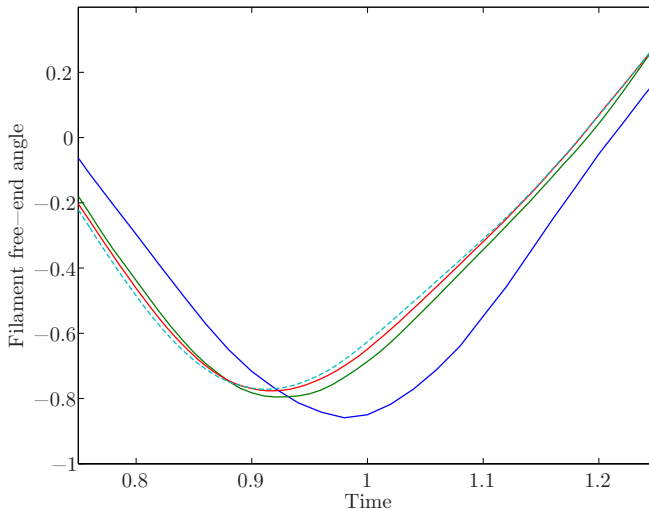


Figure 2.9: Convergence study for various grid spacings: 1/20 (blue), 1/40 (green), 1/60 (red), 1/80 (light blue, dashed). Detail.

calculating the root mean square value of the angular error. The results are shown in tab. 2.1.

Grid spacing	1/20	1/40	1/60
Average angular error, RMS	$9.46 \cdot 10^{-2}$	$2.08 \cdot 10^{-2}$	$9.62 \cdot 10^{-3}$

Table 2.1: Average error values for various grid spacings, with respect to 1/80 grid spacing.

From this results, we can be confident in the results obtained from grid with spacing equal or smaller that 1/40.

2.7 Comparison with previous works

The code has been compared with the work of Yu [22]. In that work, a single filament with given characteristics has been simulated inside a

long channel with parabolic pulsatile flow. Because of this, the parabolic inlet/outlet boundary conditions has been used in our code.

Yu simulated a filament with these dimensionless parameters:

$$\begin{aligned}\rho_r &= 1, \\ \bar{G} &= 10^3, \\ Th &= 0.0212, \\ L_f &= 0.8.\end{aligned}$$

where ρ_r is the ratio between filament and fluid densities, \bar{G} is the shear stress modulus, Th is the filament thickness and L_f its length.

The filament is immersed in a pulsatile flow defined as follows:

$$\begin{aligned}Re &= 100, \\ U_{max} &= 1.5, \\ T &= 10,\end{aligned}$$

where T is the period of the pulsatile flow. The channel is defined by:

$$\begin{aligned}H &= 2, \\ L &= 8,\end{aligned}$$

where H is the total height of the channel and L its length.

Most parameters can be imposed directly in the code we are using, but some calculations have to be done to find the corresponding filament density and bending stiffness. Regarding filament density, it should be noted that the parameter in our code is the linear density. So, simulating a filament with unitary surface density and $Th = 0.0212$ lead to a linear density of $\rho = 0.0212$, which has been used in our code.

Regarding the bending stiffness, we need to relate \bar{G} with $Kbeam$ used in our code. As for Euler–Bernoulli beam theory, we know that, for a constant properties beam:

$$EI \frac{\partial^4 w}{\partial x^4} = q(x),$$

2.8. Pressure driven code

where E is the the elastic modulus, I is the second moment of area (in a three-dimensional case), w is the deflection of the beam and q is the distributed load.

Our code is made to approximate the relation:

$$k_{beam} \frac{\partial^4 w}{\partial x^4} = q(x),$$

so that we end up with:

$$EI = k_{beam}.$$

Assuming a Poisson coefficient $\nu = 0.5$ we have:

$$E = 2\bar{G}(1 + \nu) = 3 \cdot 10^3,$$

and being, in this two-dimensional case:

$$I = \frac{Th^3}{12} = 7.94011 \cdot 10^{-7}$$

we have:

$$k_{beam} = EI = 2.3820 \cdot 10^{-3}.$$

which is the value we will use.

The simulation has been done with $dt = 1 \cdot 10^{-3}$ and a grid spacing near the filament of 1/60.

The results are very similar to those obtained in [22], as can be seen in figs. 2.10 and 2.11, the filament is moving in a physically reasonable manner and the simulation is stable.

2.8 Pressure driven code

One of the interesting displays of symmetry breaking we enlisted in section 1.4 was the existence of a non-zero mean flow inside the channel. In the previous section we described one way to impose the pulsatile flow, that is, imposing a time dependent velocity profile on the left and right boundaries of the channel, generating the desired oscillating flow. Since the

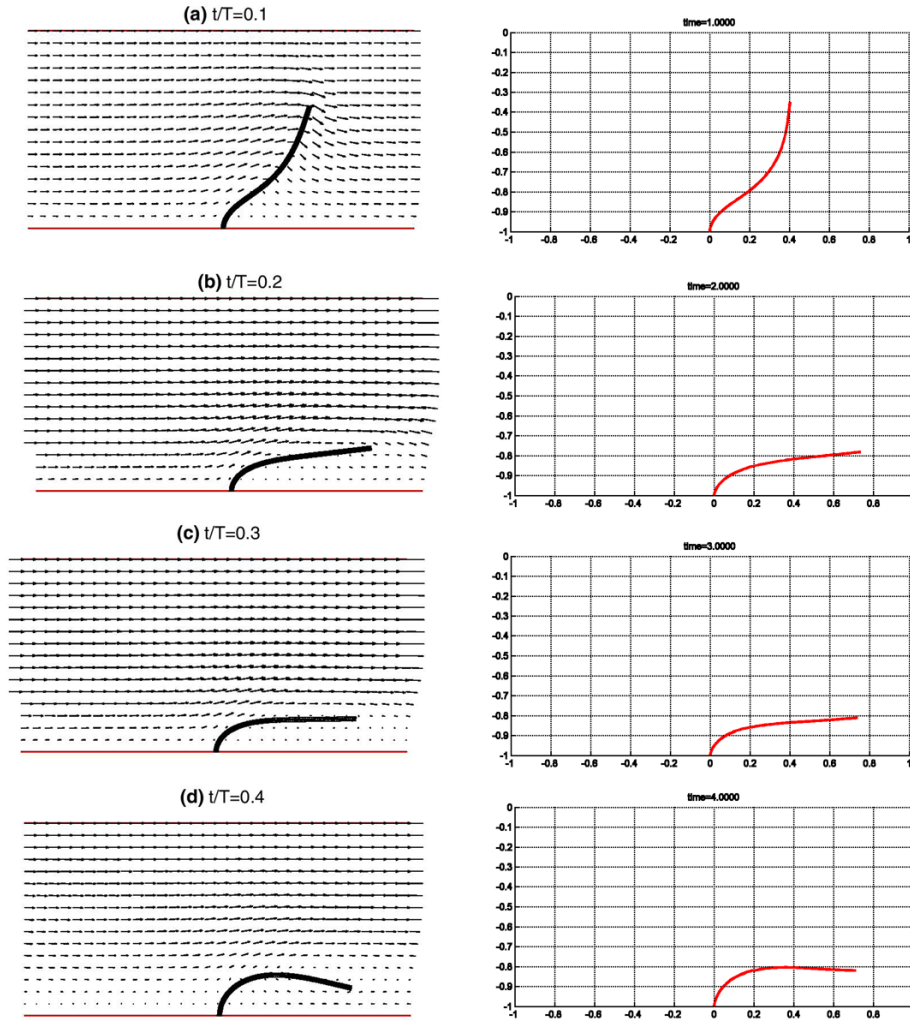


Figure 2.10: Comparison between Zu's results (left) and ours' (right) at various time-steps.

2.8. Pressure driven code

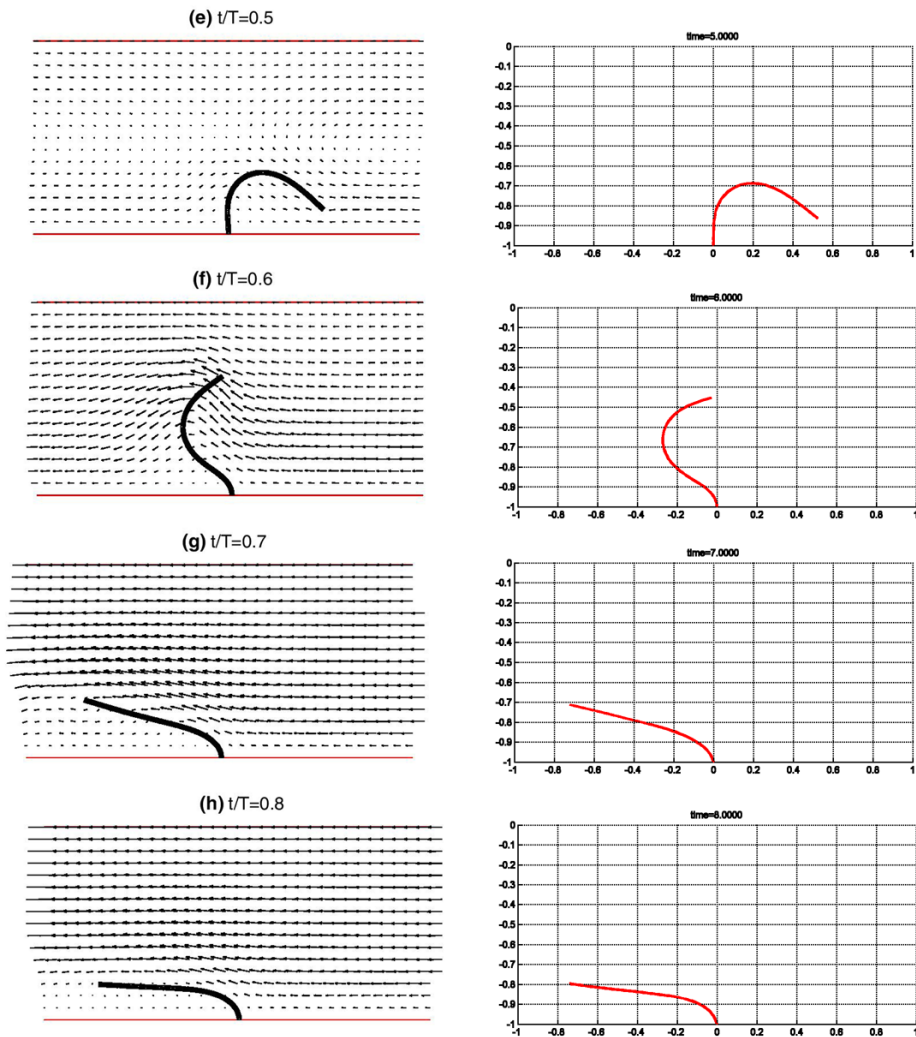


Figure 2.11: Comparison between Zu's results (left) and ours' (right) at various time-steps, continued.

pulsatile flow we need is symmetric (both y -wise and in time), the velocity profiles were symmetric y -wise and in time; because of these requirements, no net flow can be expected in the channel over time whatsoever. Something that is related to the net flow, and that can be observed in the velocity-driven version of the code, is a net pressure gradient over time, that is a non zero pressure gradient averaged over an integer number of pulsatile time-periods. Such a thing, that has been observed for some parameters sets, could mean that if the flow were driven by a symmetric (over time) pressure gradient, there would be a non zero net flow in one direction. If the pulsatile flow is implemented by means of a pulsatile pressure gradient, a net flow could exist without infringing boundary conditions; in order to further investigate this, the code has thus been modified. The boundary conditions on the left and right sides of the channel have been changed to periodic conditions (that is, the u and v at the left edge of the domain are due to be equal to the ones at the right edge, see (2.19)) and a pressure gradient is added as a known term \mathbf{p}_g .

$$\frac{\partial \mathbf{u}}{\partial t} + \mathbf{u} \cdot \nabla \mathbf{u} = -\nabla p + \frac{1}{Re} \nabla^2 \mathbf{u} + \mathbf{p}_g. \quad (2.33)$$

2.8.1 Steady flow

The next step is to quantify the value of the needed pressure gradient in order to get the desired flow, pulsatile or not. Starting from the steady case, we can derive the required value from the Navier-Stokes equations. Starting from non-dimensionalized NS equations plus the continuity equation:

$$\begin{cases} \frac{\partial \mathbf{u}}{\partial t} + \mathbf{u} \cdot \nabla \mathbf{u} = -\nabla p + \frac{1}{Re} \nabla^2 \mathbf{u} + \mathbf{f}, \\ \nabla \cdot \mathbf{u} = 0, \end{cases} \quad (2.34)$$

and knowing that:

$$\frac{\partial \mathbf{u}}{\partial t} = 0; \quad \frac{\partial u}{\partial x} = 0; \quad v \equiv 0; \quad \mathbf{f} \equiv 0,$$

2.8. Pressure driven code

then (2.34) becomes:

$$\begin{cases} \nabla p = \frac{1}{Re} \nabla^2 \mathbf{u}, \\ \nabla \cdot \mathbf{u} = 0. \end{cases} \quad (2.35)$$

Knowing the parabolic velocity distribution along y direction and imposing an average u velocity equal to one:

$$u(y) = \frac{3}{2} \left[1 - \left(\frac{y}{h} \right)^2 \right]; \quad \nabla^2 \mathbf{u} = - \left(0, \frac{3}{h^2} \right),$$

where h is the channel half-height. From these latest relations and (2.35) we can derive:

$$\frac{\partial p}{\partial x} = - \frac{3}{Re \cdot h^2}. \quad (2.36)$$

This is the pressure gradient we need to impose in our code for a given Reynolds number and a given channel height. The comparison of the resulting velocity profile and the velocity profile from the previous version of the code is shown in fig. 2.12; the profile is identical in shape and magnitude.

2.8.2 Pulsatile flow

For the pulsatile flow we will use some results from Kerczek [23] and Schmid & Henningson (sec. 6.4.1) [24].

Given a pressure gradient of the form:

$$\frac{\partial p}{\partial x} = - \frac{2}{Re} \Lambda \cos \Omega t, \quad (2.37)$$

it generates the velocity:

$$u(y', t) = \frac{\Lambda}{\gamma^2} u_1(y', t) \quad (2.38)$$

where:

$$u_1(y', t) = \Re \left\{ \left[\frac{\cosh(\gamma(1+i)) - \cosh(\gamma(1+i)y')}{i \cosh(\gamma(1+i))} \right] e^{i\Omega t} \right\} \quad (2.39)$$

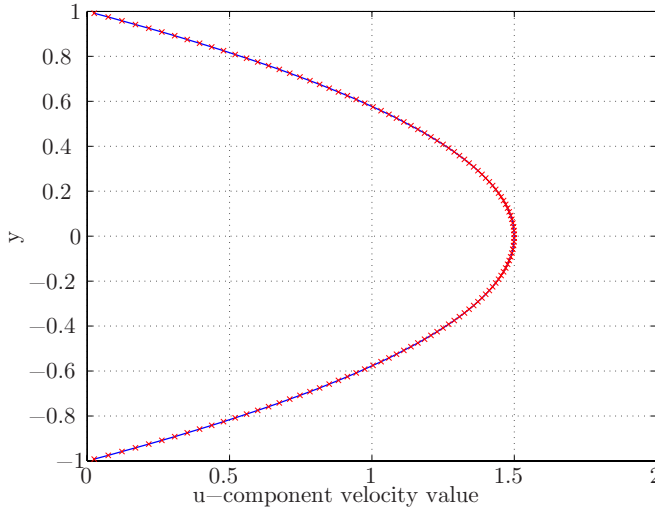


Figure 2.12: Velocity profiles comparison between the pressure driven code (blue line) and the velocity driven code (red crosses).

with $Re = U_0 h / \nu$, U_0 is the maximum bulk velocity ($U_0 = 1$), $\gamma = h / \delta$ is the ratio of the channel half-width to Stokes-layer thickness $\delta = (2\nu / \omega)^{1/2}$, $\Omega = h\omega / U_0$ is the dimensionless frequency of the imposed pressure gradient and $y' = y/h$.

Our goal is to find the right pressure gradient in order to generate a pulsatile flow characterized by a maximum y -averaged x -component velocity equal to one; that is a pulsatile flow which maximum 2D-flow (in both direction) is $2h$. In order to get the desired pressure gradient we need to give the right value of Λ , which modifies the amplitude of the pulsatile pressure gradient.

Again, as in section 2.5, we can define a single useful value describing the amplitude of $u_1(y', t)$, that is defined with close correspondence with equation (2.32). As stated, the overline indicates the y -wise averaging operation, while the subscript indicates that we take the maximum value over a pulsatile time period.

2.8. Pressure driven code

It can be shown that the maximum values of (2.39) are obtained for $\omega t = \pi/2 + k\pi$, for integer values of k ; this means that in order to calculate \bar{u}_{1ax} we can substitute $e^{i\omega t}$ with $\pm i$; we will use $+i$. Equation (2.39) becomes:

$$u_{1ax}(y') = \Re \left[\frac{\cosh(\gamma(1+i)) - \cosh(\gamma(1+i)y')}{\cosh(\gamma(1+i))} \right]. \quad (2.40)$$

Now we need to integrate (2.40) y -wise, in order to average it:

$$\begin{aligned} \bar{u}_{1max} &= \frac{1}{2} \int_{-1}^1 \Re \left[\frac{\cosh(\gamma(1+i)) - \cosh(\gamma(1+i)y')}{\cosh(\gamma(1+i))} \right] dy' = \\ &= \frac{1}{2} \Re \left[\int_{-1}^1 1 - \frac{\cosh(\gamma(1+i)y')}{\cosh(\gamma(1+i))} dy' \right] = \\ &= \frac{1}{2} \Re \left[2 - \left[\frac{\sinh(\gamma(1+i)y')}{(\gamma(1+i)) \cosh(\gamma(1+i))} \right]_{-1}^1 \right] = \\ &= \frac{1}{2} \Re \left[2 - \frac{2 \tanh(\gamma(1+i))}{(\gamma(1+i))} \right]. \end{aligned} \quad (2.41)$$

In fig. 2.13 the value of \bar{u}_{1max} is plotted for γ between 0 and 100.

From equation (2.38) we can derive that:

$$\bar{u}_{Max} = \frac{\Lambda}{\gamma^2} \bar{u}_{1max}. \quad (2.42)$$

As already stated, we want \bar{u}_{Max} , which is the time-maximum, y -wise averaged velocity in the channel, to be equal to one; so we need to impose:

$$\frac{\Lambda}{\gamma^2} \bar{u}_{1max} = 1, \quad (2.43)$$

that is:

$$\Lambda = \frac{\gamma^2}{\bar{u}_{1max}} = \frac{h^2}{\left(\frac{2\nu}{\omega}\right) \bar{u}_{1max}} = \frac{Re \cdot \omega h}{2U_0 \bar{u}_{1max}} = \frac{Re \cdot \Omega}{2\bar{u}_{1max}}. \quad (2.44)$$

Substituting (2.44) into (2.37) we obtain:

$$\frac{\partial p}{\partial x} = -\frac{2}{Re} \frac{Re \cdot \Omega}{2\bar{u}_{1max}} \cos \Omega t = -\frac{\Omega}{\bar{u}_{1max}} \cos \Omega t. \quad (2.45)$$

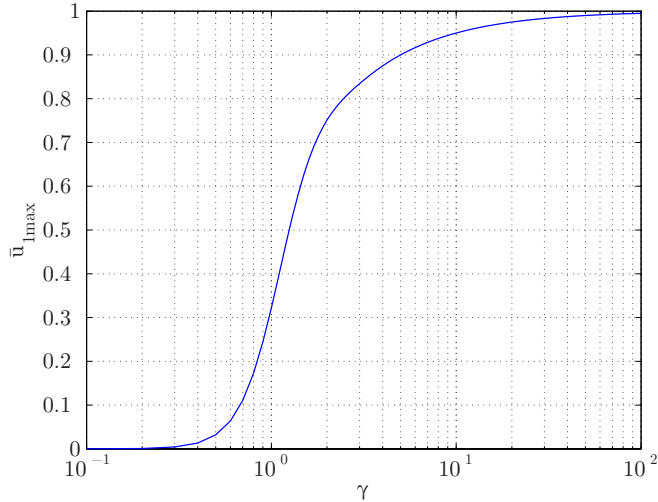


Figure 2.13: Value of \bar{u}_{1max} for γ between 0 and 100.

The results obtained have been used in the code to generate the pulsatile flow. The velocities obtained have been compared to those obtained with the original version of the code. In figure 2.14 the two velocity profiles measured at $x = 0$ are plotted for the time step corresponding to a quarter of a period: the plot shows a very good agreement between the two methods.

2.9 Validation with COMSOL

Even if the basic comparisons made between the two codes showed very positive results, they can not be considered a good validation test since they are overly simple: there are many terms in the Navier-Stokes equations that vanish in this scenario, beginning with those containing the v -component of the velocity. To validate the new pressure-driven code we have chosen to compare its results with the ones obtained with the commercial code *COMSOL Multiphysics* [25] in a test case scenario that has to be simple enough to be easily created both in MATLAB and COMSOL, but also

2.9. Validation with COMSOL

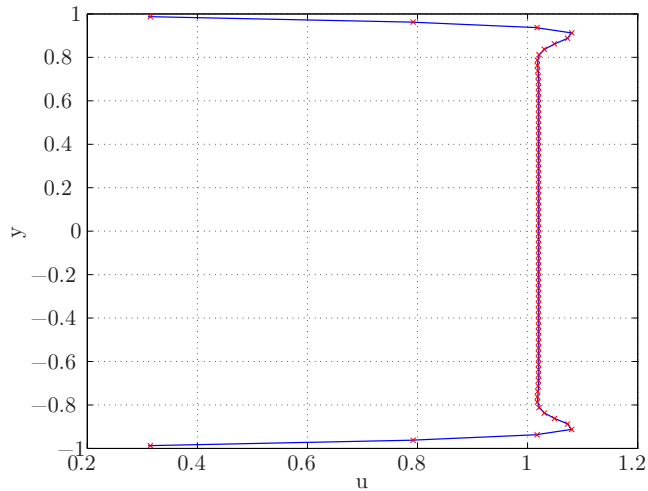


Figure 2.14: Velocity profiles comparison between the pressure driven code (blue line) and the velocity driven code (red crosses).

complex enough to fully put our code to the test. The setup chosen consists in a periodic series of cylinders put inside an horizontal channel in which there is a steady streaming. Both simulations are run with the same size of the channel ($L = 2$, $2h = 2$), the same cylinder radius ($r = 0.25$) and the same flow properties ($Re = 100$, $\bar{U} = 1$). In fig. 2.15 the two velocity fields are shown side by side, underlining very good agreement. In order to obtain a more quantitative result, the velocity profiles along two lines have been plotted; the two lines are, with respect to the usual cartesian coordinates, at $y = 0.5$ (fig. 2.16) and $x = -1$ (fig. 2.17). The differences are negligible, so that the validation can be considered positive.

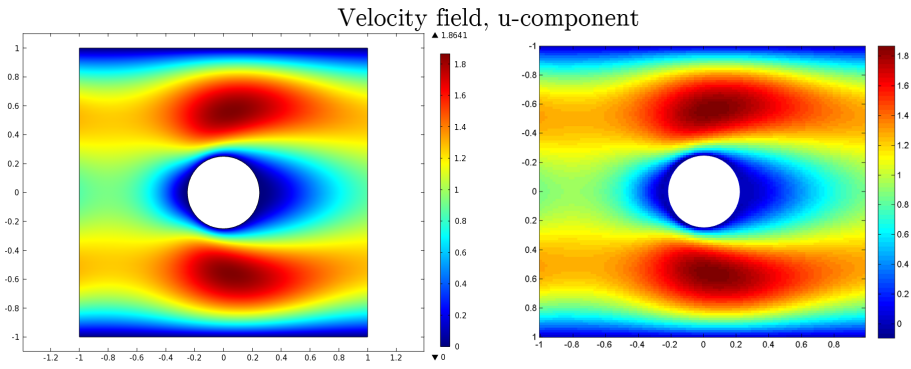


Figure 2.15: Velocity fields comparison, using COMSOL code, left, and our MATLAB code, right.

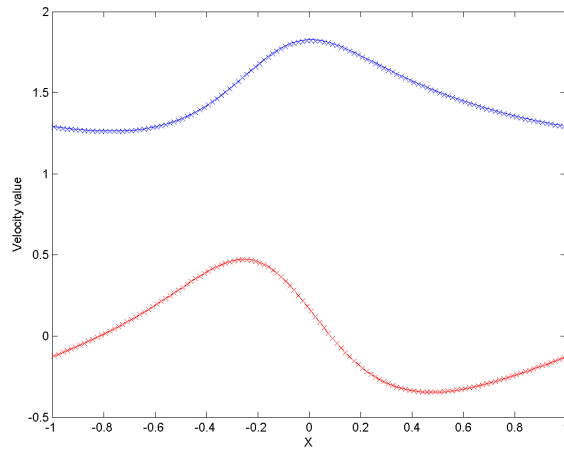


Figure 2.16: Velocity profiles comparison between the two codes at $y = 0.5$. In continuous lines the results from the MATLAB code, in crossed lines the ones from COMSOL. In blue the u -component, in red the v -component.

2.9. Validation with COMSOL

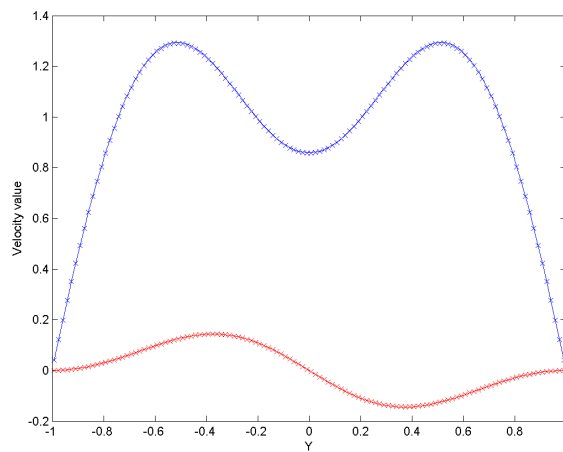


Figure 2.17: Velocity profiles comparison between the two codes at $x = -1$. In continuous lines the results from the MATLAB code, in crossed lines the ones from COMSOL. In blue the u -component, in red the v -component.

Chapter 3

Results - Velocity driven code

The first simulations have been run using the velocity driven code. Out of the many properties we can vary, we decided to start varying the pulsatile-flow time period, T . This parameter modifies strongly the behaviour of the system, so it has a big influence on the simulation outputs, making it reasonable to investigate its effects first. We can define an adimensional number related to the pulsatile-flow time period, i.e. the Strouhal number. It is generally defined as follows:

$$St = \frac{fL}{U} = \frac{L}{TU}$$

where f , L , U and T are, respectively, the characteristic frequency, length, velocity and time of the system. In our case it is defined as:

$$St = \frac{L_f}{T\bar{u}_{max}} \quad (3.1)$$

L_f being the filament length, T the pulsatile-flow time period and \bar{u}_{max} the characteristic velocity we defined in sections 1.2 and 2.5. The choice of using the filament length as a length scale instead of the usual channel half

3.1. One filament

Parameter	Value
<i>Channel</i>	
Length, L	12
Height, $2h$	4
Number of filaments, N_f	1
<i>Filament</i>	
Length, L_f	0.8
Density, ρ_f	0.05
Elastic stiffness, K_{elas}	100
Bending stiffness, K_{beam}	$5 \cdot 10^{-3}$
<i>Flow</i>	
Characteristic velocity, \bar{u}_{max}	1
Reynolds number, Re	80, 120, 240, 400
Time-period, T	∞

Table 3.1: Parameters used for the simulations.

height h may seem odd, but since the phenomenons we are investigating depends on the filament length more strongly than on the channel height, this can be a good definition.

The number and position of the filament(s) has been varied too.

3.1 One filament

In the basic configuration just one filament is clamped to the bottom wall of the channel, in central position.

3.1.1 Steady-flow case

We will first consider a steady-flow case, in which the fluid simply moves inside the channel bending the filament towards one side. The flow is imposed through boundary conditions, so that a parabolic velocity profile is imposed at the inlet of the channel. We can consider this as a limit for very

low values of the Strouhal number: since there is no pulsatile flow we can consider it as a pulsatile flow of infinitely long time-period T , so that the Strouhal number would be *zero*. In table 3.1 the parameters used for this simulation are listed.

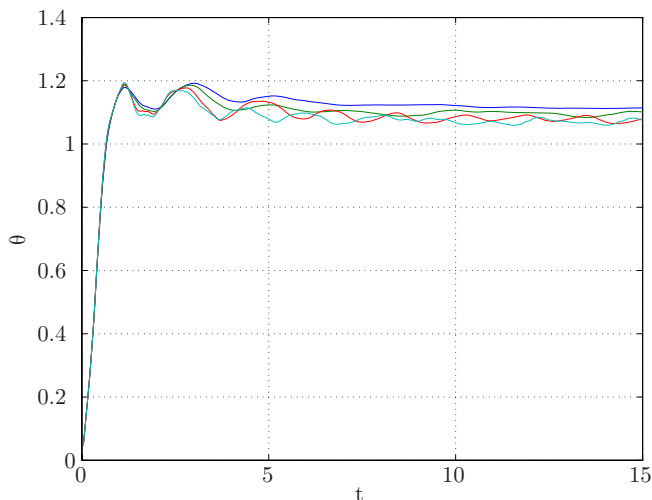


Figure 3.1: Filament free end angle θ (in radians) versus time for Reynolds number 80 (blue), 120 (green), 240 (red) and 400 (light blue).

The results of this preliminary simulation are shown in fig. 3.1, where the angle formed by the free end of the filament, the position at the wall where the filament is clamped, and the bottom wall of the channel, θ , is plotted against time for various Reynolds numbers. As the Reynolds number grows, a small unsteadiness can be seen as the θ angle starts fluctuating around its average value. This is due to vortex shedding, as can be seen in fig. 3.2, where the vorticity value is plotted for $Re = 400$. Also, the angle decreases as the Reynolds number increases, due to the decreasing force exerted by the low-viscosity fluid.

3.1. One filament

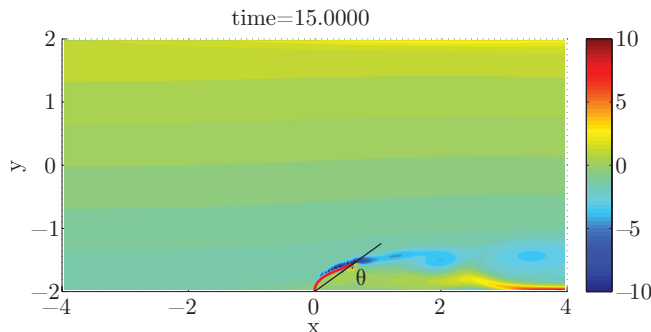


Figure 3.2: Snapshot of the vorticity in the channel $Re = 400$.

3.1.2 Strouhal number bifurcation

A set of simulations varying the pulsatile time period, and thus the Strouhal number have been done. The parameters that have been used are listed in table 3.2. As for the filament density, no significant differences appeared using the previous value, 0.05, or setting it to *zero*, so from now on the latter value will be used in order to take away one spatial dimension from the parameters space. It is to be noted that this does not mean that the filament will now exhibit buoyancy: the density imposed in the code is responsible for filament inertia, while the filament is always considered mono-dimensional and neutrally buoyant. The channel length is chosen to be 8: multiple value of it have been tested and this value is the smallest one that ensures no significant boundary effects.

In figure 3.3 the average angle θ is plotted for different pulsatile time periods. The filament shows a symmetric behaviour for short and long time periods, while for intermediate values of T it behaves asymmetrically. The sign of the average angle depends on the initial conditions: applying a $T/2$ time shifting to the pulsatile flow determines an average angle of same amplitude but opposite sign. Thus this symmetry breaking happens through what is called a bifurcation; its peak is reached for $T = 2.1$ when the average angle reaches a value of 0.148 rad or 8.5° .

Chapter 3. Results - Velocity driven code

Parameter	Value
<i>Channel</i>	
Length, L	8
Height, $2h$	4
Number of filaments, N_f	1
<i>Filament</i>	
Length, L_f	0.8
Density, ρ_f	0
Elastic stiffness, K_{elas}	100
Bending stiffness, K_{beam}	$5 \cdot 10^{-3}$
<i>Flow</i>	
Characteristic velocity, \bar{u}_{max}	1
Reynolds number, Re	200
Time-period, T	0.6, 0.9, 1.2, 1.5, 1.8, 1.95, 2.1, 2.25, 2.4, 2.55, 2.7, 3, 3.6

Table 3.2: Parameters used for the simulations.

3.1. One filament

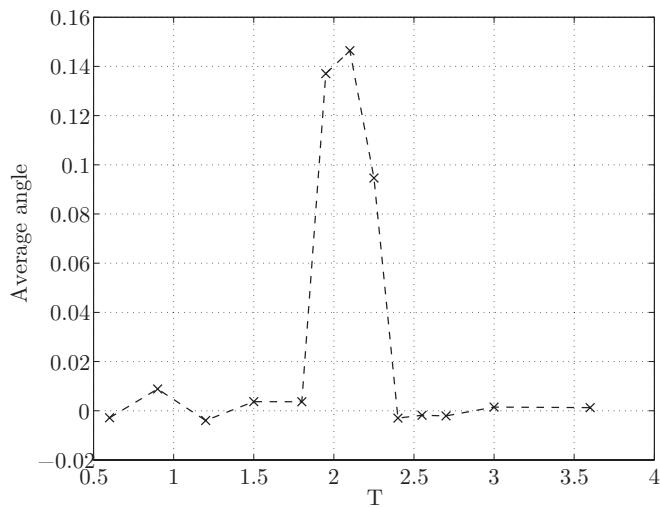


Figure 3.3: Average angle $\bar{\theta}$ versus pulsatile time period T . A bifurcation can be seen, with a peak around $T = 2.1$.

Figures 3.4a, 3.4c, 3.4b show the filament position at different times respectively for $T = 1$, $T = 2.1$, $T = 3$; only in the second case clear signs of asymmetry can be seen, while in the first and last ones the movement is symmetric. For better details, in fig. 3.5 the path of the free end of the filament is plotted, for $T = 2.1$; as the time passes the filament movement gets more and more asymmetric, until the free end draws an asymmetric eight figure in space.

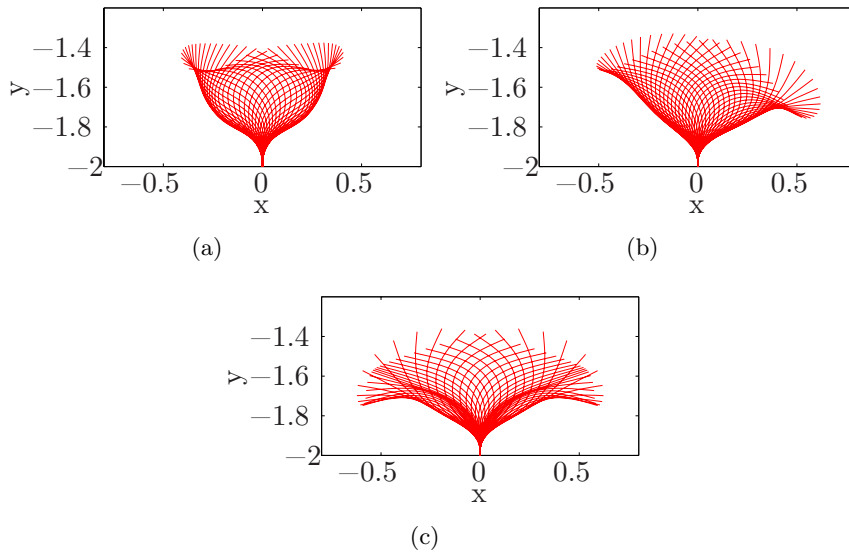


Figure 3.4: Filament position at different times for $T = 1$ (a), $T = 2.1$ (b), $T = 3$ (c). Asymmetry is clear for $T = 2.1$.

3.1.3 Varying the length of the filament

Another set of simulations has been run, everything else being equal, with a filament length $L_f = 0.6$ and with $T = 0.4, 0.6, 0.8, 1, 1.2, 1.35, 1.8, 2.1, 3$.

The results are plotted in fig 3.6 (red line) compared with those obtained in the past section (black line).

3.1. One filament

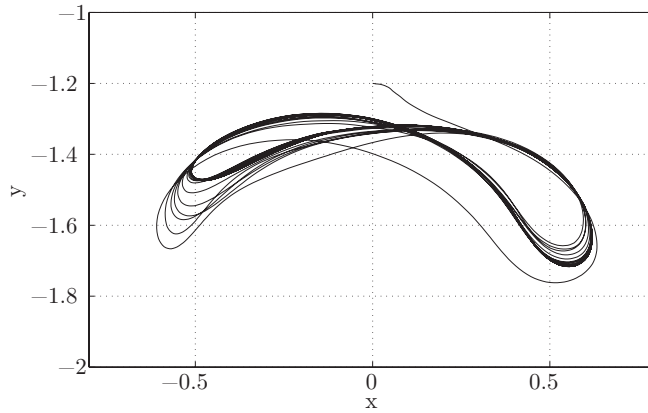


Figure 3.5: Filament free end path for $T = 2.1$.

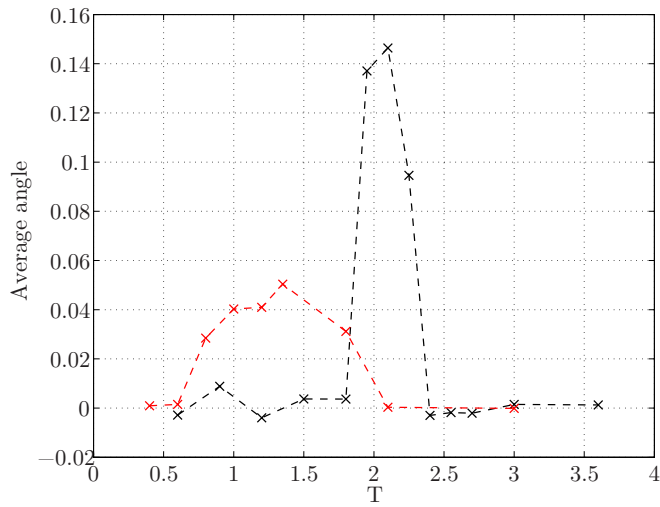


Figure 3.6: Average angle $\bar{\theta}$ versus pulsatile time period T for $L_f = 0.6$ (red line) and $L_f = 0.8$ (black line).

The maximum average angle is smaller (around 0.05 rad) and the peak appears for a shorter time period ($T = 1.35$).

There could be a link between the position of the peak (with respect to T) and the length of the filament: it seems that for shorter filaments the peak occurs for shorter time periods. Plotting the same data of fig. 3.6 versus the inverse of the Strouhal number (as defined at the beginning of this chapter), together with a third set of simulations with $L_f = 1$, the three lines shows a similar shape and the peak is found around the same value, between $St = 0.4$ and $St = 0.5$. (fig. 3.7).

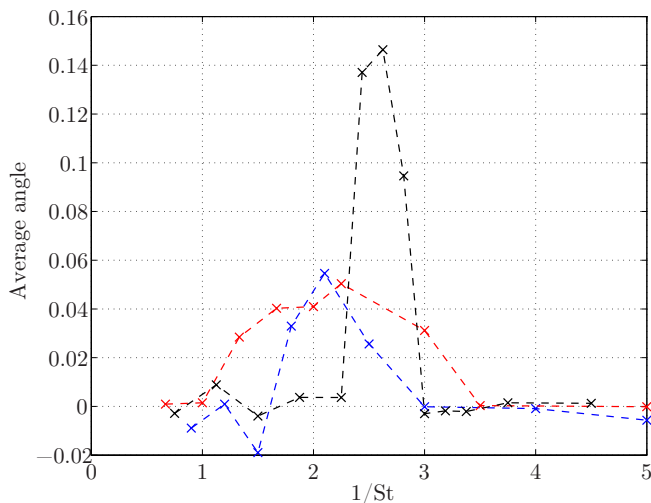


Figure 3.7: Average angle $\bar{\theta}$ versus $1/St$ for $L_f = 0.6$ (red line), $L_f = 0.8$ (black line) and $L_f = 1$ (blue line). The three peaks now share a similar value of St .

3.1.4 Asymmetry analysis

The case that showed the maximum average angle ($L_f = 0.8$, $T = 2.1$) has been investigated more to understand the motion of the fluid.

3.1. One filament

To do this, a script has been written in order to simulate a physical passive scalar. A passive scalar is a contaminant in a fluid flow that is present in such low concentrations that it has no dynamical effect (such as buoyancy) on the fluid motion itself; usually smoke or dye particle are used in experiments [26].

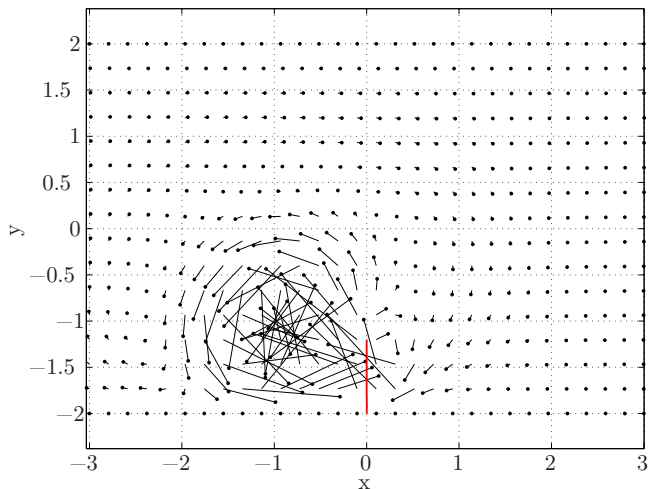


Figure 3.8: The initial position and the final position of a set of passive scalars is linked by a black line, a dot marks the final position after one period. The red line denotes the filament at rest.

To simulate this we followed a set of virtual particles; at every timestep the velocity of every particle is updated interpolating the eulerian velocity field and then the particle position is moved using a 3rd order Runge-Kutta method, enforcing the continuity equation [27] [28]. Each particle is followed for a whole time-period, during which they will move first towards one side and then towards the other. Without any filament interaction they would go back to the same position they started from, and this has been tested and confirmed. In the presence of the filament and after asymmetry kicks in, this is not true anymore. In fig. 3.8 the initial position and the final position of each virtual particle is linked by a black line, a dot marks the

final position, and the filament original position is plotted in red.

There is a clear vortical structure on the left side of the filament, rotating counter-clock-wise. Its center is roughly one unit to the left and one unit above the clamped end of the filament and the vortex has a diameter of approximately two units. Being the filament-height 0.8, it may well be influenced by the lower part of the vortex, in which the flow is moving towards the right; this qualitative observation is in agreement with the average bending of the filament, to the right side.

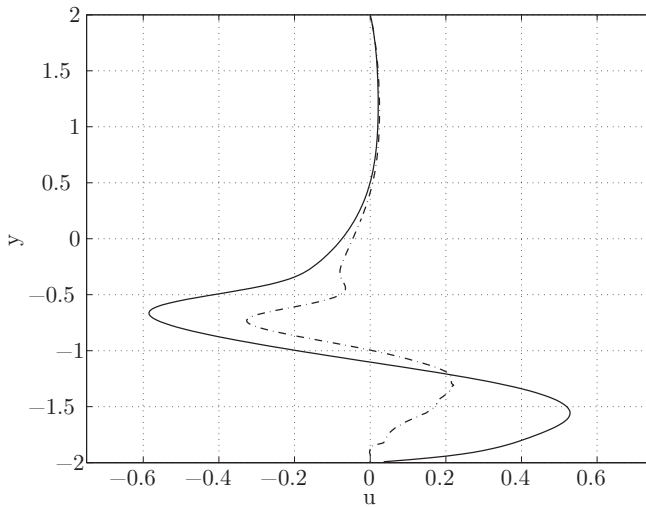


Figure 3.9: The u -velocity profiles of two channel sections at $x = -1$ (roughly corresponding to the center of the vortex) and at $x = 0$ (corresponding to the filament position) are plotted, as a continuous line and as a dash-dot line, respectively.

To further investigate these aspects, the u -component of the velocity field has been time-averaged over the same time-period; the velocity profiles of two channel sections at $x = -1$ (roughly corresponding to the center of the vortex) and at $x = 0$ (corresponding to the filament position when at rest) are plotted in fig. 3.9, as a continuous line and as a dash-dot line,

3.1. One filament

respectively. We can confirm that in the filament region the existing vortex pushes the filament to the right and is the apparent cause of the angular asymmetry. At $x = -1$, where the vortex generates the biggest velocities, u can exceed a value of 0.5, which is half the imposed \bar{u}_{max} .

3.1.5 Net force and pressure gradient

As we stated in section 1.4, the way this code imposes the pulsatile flow (via velocity boundary conditions) rules out the possibility of measuring a net flow when averaging the flow rate over time. This does not, on the other hand, prevent the existence of a non zero average pressure gradient inside the channel or a non zero force applied from the filament and the walls to the fluid.

Two scripts have thus been written, one to measure the pressure difference between the left side and the right side of the channel, to calculate the spatial-averaged x pressure gradient and to average it over time; the other to measure the viscous forces due to the channel walls and the horizontal forces due to the filament interaction and to average them. This corresponds to:

$$\nabla p_x(t) = \frac{1}{2hL} \int_{-h}^h [p(L/2, y, t) - p(-L/2, y, t)] dy, \quad (3.2)$$

$$\overline{\nabla p_x} = \frac{1}{kT} \int_{\tau}^{\tau+kT} \nabla p_x(t) dt, \quad k \in \mathbb{N}, \quad (3.3)$$

and

$$f_v(t) = \int_{-L/2}^{L/2} \mu \frac{\partial u(x, y, t)}{\partial y} \Big|_{y=-h} dx + \int_{-L/2}^{L/2} \mu \frac{\partial u(x, y, t)}{\partial y} \Big|_{y=h} dx, \quad (3.4)$$

$$f_f(t) = \int_0^{L_f} f_x(s, t) ds, \quad (3.5)$$

$$\overline{f_{v+f}} = \frac{1}{kT} \int_{\tau}^{\tau+kT} [f_f(t) + f_v(t)] dt, \quad k \in \mathbb{N}, \quad (3.6)$$

Chapter 3. Results - Velocity driven code

where f_v is the viscous force due to the horizontal walls, μ the dynamic viscosity, f_f the horizontal force due to the filament, f_x the horizontal force applied by the filament to the fluid per unit length and s a curvilinear coordinate of the filament.

If these quantities are measured in the right way, they should be linked, and precisely it should be:

$$2Lh\overline{\nabla p_x} = \overline{f_{v+f}}. \quad (3.7)$$

In figure 3.10 the trend of $\nabla p_x(t)$, $f_v(t)$ and $f_f(t)$ are plotted respectively in blue, red and black, during 10.5 time units, that is 5 time periods.

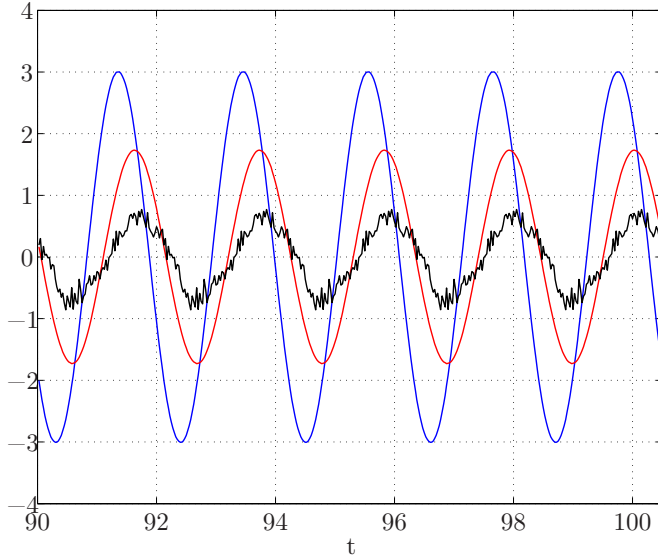


Figure 3.10: Trend of $\nabla p_x(t)$ (blue), $f_v(t)$ (red) and $f_f(t)$ (black) during 5 pulsatile time periods.

These values have been averaged over time, as in (3.3) and (3.6), yielding:

$$\overline{\nabla p_x} = 1.584 \cdot 10^{-4} \quad \overline{f_{v+f}} = 5.203 \cdot 10^{-3}$$

3.2. Two filaments

Upon enforcing (3.7):

$$2Lh\overline{\nabla p_x} = 5.0688 \cdot 10^{-3} \sim 5.203 \cdot 10^{-3} = \overline{f_{v+f}}$$

So that the two results are in remarkably good agreement. There is, thus, a net force acting from left to right, or, which is equivalent, a net positive pressure gradient that is needed to keep the desired pulsatile flow, due to the imposed velocity boundary conditions. An interesting thing to investigate is whether, if the pulsatile flow would be generated through a pressure gradient, a non-zero average net flow would develop. This will be the object of the next chapter.

3.2 Two filaments

To investigate the interaction between filaments we set up a series of simulations with two filaments on the same side of the channel, spaced apart by a certain distance d . All other parameters have been kept the same as the ones that generated the biggest average angle, most notably $T = 2.1$.

In fig. 3.11 the average angle of each filament is plotted, for various values of the distance between them. Due to the code structure, for distances smaller than 0.8 the free ends of the two filaments tend to stick to each other, because of the overlapping of the two discrete delta functions used to update their position, so the results for such distance values have not been plotted. When the two filaments are close together they tend to bend one towards the other, so that the right one bend on the opposite side with respect to the left one. This does not happen as the distance between them increases: when the distance is greater than 2 the two filaments behaves similarly to each other, which means the two filaments are decoupled.

In figures 3.12a, 3.12b, 3.12c, 3.12d the filament behaviour can be better seen: for both the distance values considered each filament moves asymmetrically, in a way that is similar to the one of the single filament, cf. figs. 3.4b and 3.5, the difference being that when they are close together the whole system behaves symmetrically, while when they are spaced enough apart it does not.

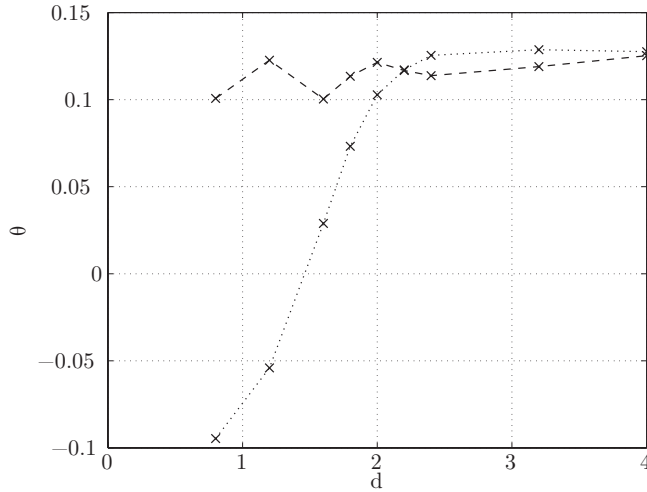


Figure 3.11: Left filament (dashed line) and right filament (dotted line) average angle, versus distance d between the two filaments.

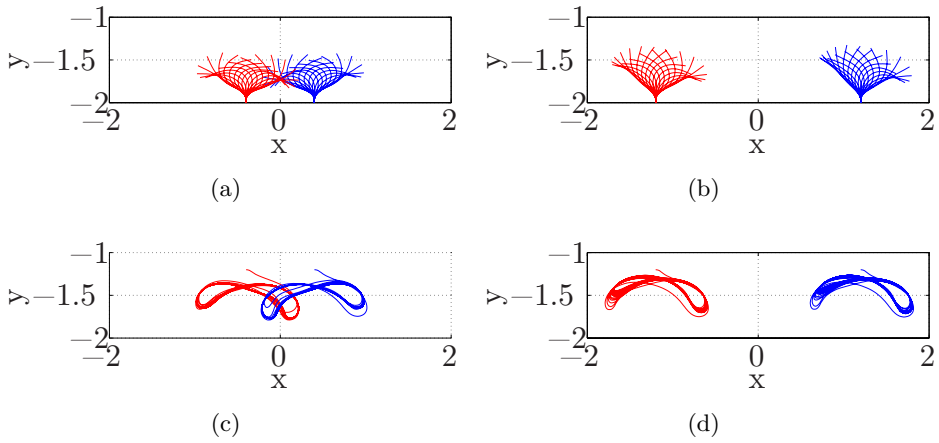


Figure 3.12: Filaments position at different time for $d = 0.8$ (a) and $d = 2.4$ (b); filaments free-ends trajectories for $d = 0.8$ (c) and $d = 2.4$ (d).

3.2. Two filaments

3.2.1 Sensitivity to initial condition

Next, we will examine more in depth the system composed by two filaments spaced apart of a distance $d = 0.8$, a case that shows a different and interesting behaviour compared to the single filament case. In particular, we want to verify whether the final configuration we saw depends on the initial position of the filaments or not. To do this three more simulations have been run, with the three initial conditions shown in figs. 3.13b, 3.13c and 3.13d, and the results have been compared with those already run, whose initial conditions are shown in 3.13a.

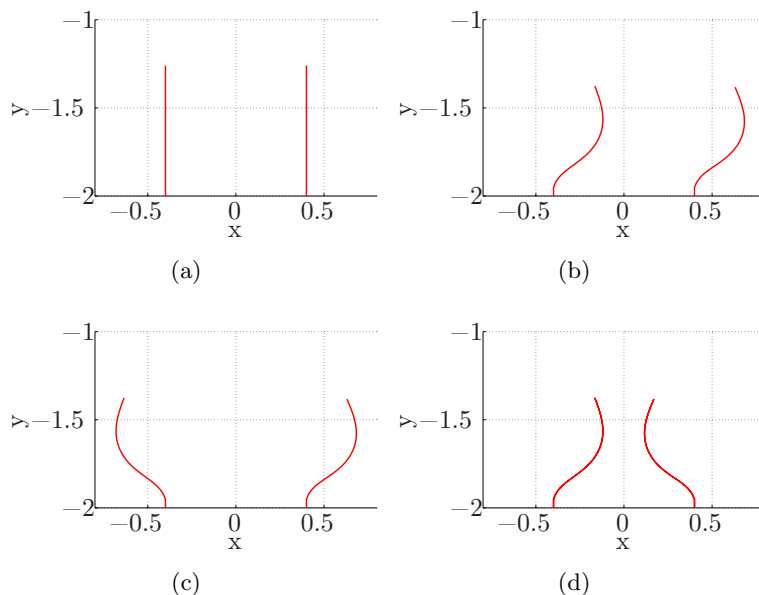


Figure 3.13: The three filaments initial positions for the new simulations (b, c, d) and the original one (a).

The results show that, after a short transient, the filaments initial positions exert no influence on the movement of the filament. In fig. 3.14 the horizontal distances between the two filament free ends are plotted versus

time, each line representing one of the four cases. Even if the observable chosen shows big differences between the cases at the beginning of the simulations, the difference becomes negligible after less than five time units; the sensitivity to the initial conditions is thus negligible, and this seems reasonable when considering that the filaments are passive and only driven by the flow.

It would be interesting to examine the situation at larger values of Re , where a possibly chaotic behaviour may change these conditions, but this is outside the scope of the present research. We thus move to consider the case of a channel flow driven by a periodic pressure gradient.

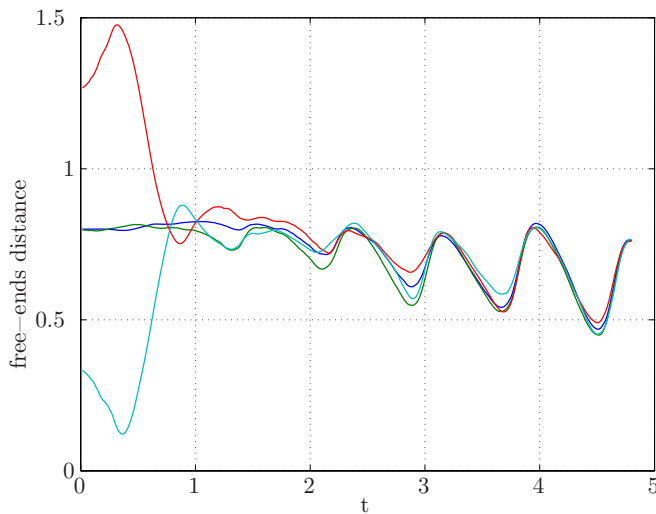


Figure 3.14: Filaments free-ends distance versus time for the initial conditions in fig. 3.13a (blue), 3.13b (green), 3.13c (red) and 3.13d (light blue).

Chapter 4

Results - Pressure driven code

We will now examine the results obtained with the second version of our code, in which the pulsatile flow is driven by a pulsatile pressure gradient, imposing periodic boundary conditions.

In the first place we will check whether the two versions of the code provide the same results under similar conditions, then we will study new parameters sets.

First of all we want to define how we will measure the average net flow that we are looking for. What we will do is to integrate the u velocity along y and average the value over an integer number k of periods. This yields to:

$$u_{net} = \frac{1}{kT} \int_{\tau}^{\tau+kT} \left[\int_{-h}^h u(x, y, t) dy \right] dt, \quad (4.1)$$

which is constant along x due to the incompressibility constraint. This is the observable we will measure and plot, indicating the average velocity inside the channel; it should be compared to \bar{u}_{max} , which is the velocity magnitude due to the pulsatile flow.

4.1. Comparison with previous code

4.1 Comparison with previous code

The comparison with the results obtained with the velocity driven code is made using the parameters already listed in tab. 3.2, the only difference being $L = 12$. This parameter acquires now a bigger importance: in the velocity driven code we choose a large enough value in order to have no significant boundary effects; now we need to take into account that, due to the periodic boundary conditions, we are simulating an infinite array of filaments, whose spacing between each other is L . Also, since we will observe an average net flow, the ratio between filaments and the walls length (where the friction tends to diminish the average net flow, if it exists) gets a new important role; because of these facts a bigger value has been chosen.

In fig. 4.1 the average angle obtained with the new code is plotted (blue line) together with the one from the previous code (black line).

The two resulting curves are very similar: both show a clear central peak, found for the same values of St ; the two peaks also share the same value of $\bar{\theta}$. In the left side of the plot the shapes of the two curves show some differences, because the new results exhibit asymmetry in this region. The reason for this will be studied in the next section.

The general agreement between the two codes is very good; the asymmetric phenomenon we are studying, then, is not due to boundary conditions effects.

The net velocity, as defined in the previous section, is plotted in fig. 4.2 (red line), together with the average angle values (blue line). The results show that the amplitude of the net velocity is very small, mainly due to the large length of the channel, which corresponds to filaments much spaced apart, so that their influence is small on the whole quantity of fluid. Nevertheless, the net velocity is mostly negative and this probably influences the average angle, that show small negative values in the left part of the graph.

Further analysis have been done varying the channel characteristic sizes and other parameters, but it is useful to first analyse these results in order to be able to make predictions and to explain new results.

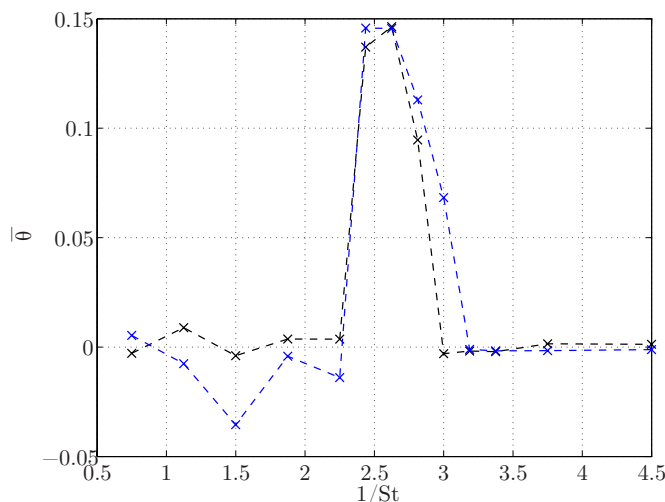


Figure 4.1: Average angle $\bar{\theta}$ versus $1/St$ obtained with the new code (blue line) and with the previous code (black line).

4.2 Average velocity fields

Depending on the Strouhal number, the flapping filament immersed in a pulsatile flow have different effects on the flow itself. In order to show this we will analyse the average velocity fields (u and v components), so that we can isolate the filaments effect from the pulsatile flow: being the latter symmetric, the associated average velocity fields would be null.

We noted that in the zone of intermediate values of St an asymmetric vortex is stable at one side of the filament; this also can be visualized in the average velocity fields. In figs. 4.3a and 4.3b the average fields (in the central area of the channel, which is longer, $L = 12$) for u and v are plotted respectively, for $T = 2.1$; through their analysis the existence of the vortex is confirmed in the new code too.

In the zone of short T we noticed a slightly different behaviour in the new simulations compared to the old ones. Looking at the average velocity

4.2. Average velocity fields

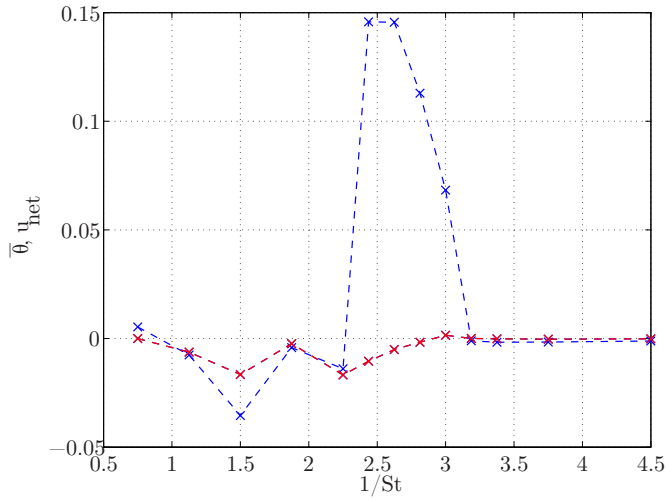


Figure 4.2: Average net velocity u_{net} (red line) and average angle $\bar{\theta}$ (blue line) versus $1/St$.

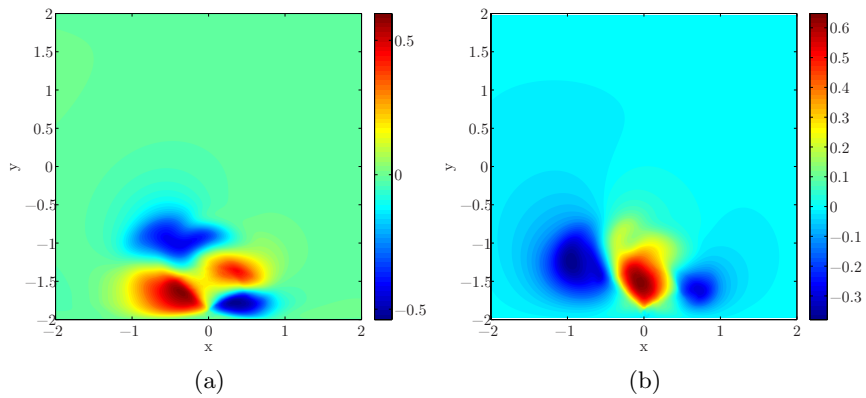


Figure 4.3: Average u field (a) and v field (b) in the central area of the channel, for $T = 2.1$. The filament creates a vortex on the left side.

fields (figs. 4.4a and 4.4b showing u and v fields respectively) we see that the filament pushes the fluid towards the top wall of the channel, generating a jet. Such a jet, or, better, due to the periodic boundary conditions, such a series of jets, can bend towards one side and find a new equilibrium in presence of the no-slip conditions at walls. This is exactly what happens in our simulations, the presence of the bent jet can be deduced especially from an accurate analysis of fig. 4.4b.

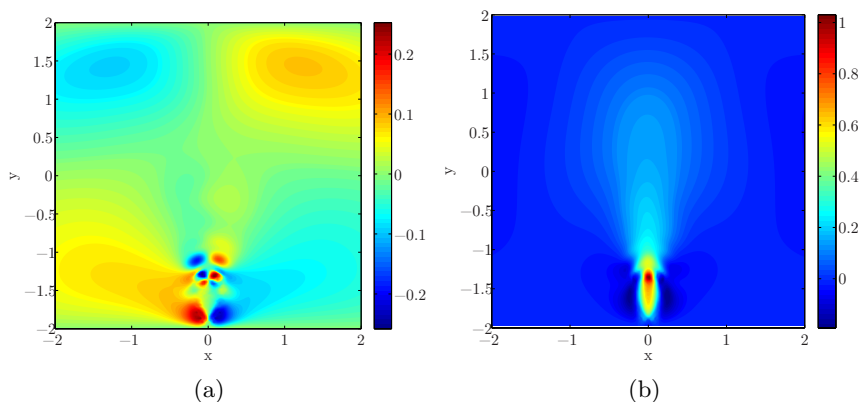


Figure 4.4: Average u field (a) and v field (b) in the central area of the channel, for $T = 0.6$. The filament creates a jet that is very slightly bent towards the left.

For long T the filament has the opposite effects on the flow. Looking at the average velocity fields (figs. 4.5a and 4.5b showing u and v fields respectively) we see that the filament pushes the fluid towards the sides of the channel, sucking it from the center. This effect, especially if the filaments are closer to each other, generates again vertical jet towards the top of the channel; in this case the jets are located in correspondence with the domain boundaries, that is between two periodic filaments.

It is important to notice the presence, in the top half of the channel, of two zones characterized by opposite u velocity: for shorter channels their

4.2. Average velocity fields

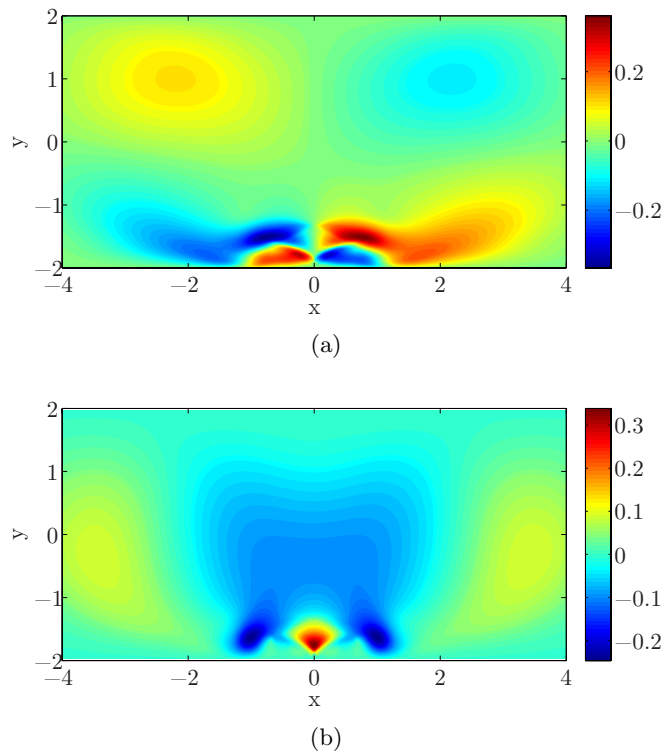


Figure 4.5: Average u field (a) and v field (b) in the central area of the channel, for $T = 3.6$. The filament moves the fluid towards the sides of the channel.

existence will become not stable and one of them two will start to dominate the whole upper part, generating net flow.

4.3 Channel length

We did multiple sets of simulations varying the value of L and keeping the other parameters equal to the ones listed in tab. 3.2. The values chosen for L are: 12, 6, 3, 2.

In figs. 4.6 and 4.7 the average angle $\bar{\theta}$ and average net velocity u_{net} are plotted respectively for the four values of L .

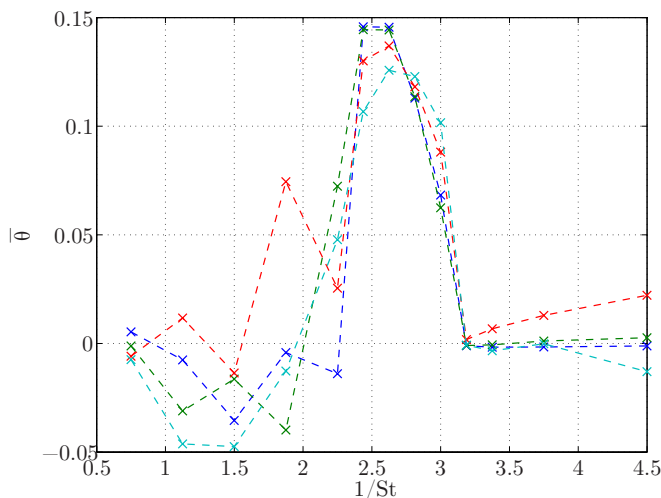


Figure 4.6: Average angle $\bar{\theta}$ versus $1/St$, for $L = 12$ (blue), $L = 6$ (green), $L = 3$ (red) and $L = 2$ (light blue).

Let's first analyse the average angle, and let's divide the $1/St$ range in three zones, the first one for small T and $1/St < 2$, the second one for intermediate T and $2 < 1/St < 3.5$, and the third one for large T and $1/St > 3.5$. While it is difficult to draw conclusions on the importance of L in the first zone, we can say something for the second and the third ones.

4.3. Channel length

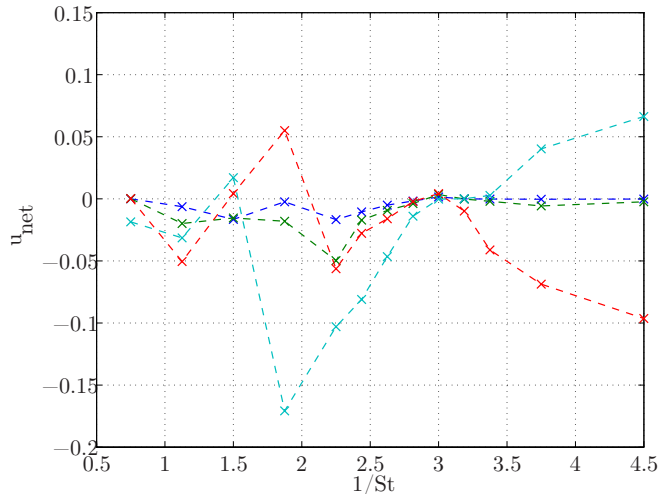


Figure 4.7: Average net velocity u_{net} versus $1/St$, for $L = 12$ (blue), $L = 6$ (green), $L = 3$ (red) and $L = 2$ (light blue).

For intermediate T , in the zone of largest asymmetry, the reduction of L generates a small reduction of $\bar{\theta}$; for large T there is a clear trend towards asymmetry as L gets smaller.

Looking at the average net flow u_{net} or, which is more clear, to the absolute value of u_{net} in fig. 4.8, we can see that there is a clear trend towards larger u_{net} for shorter channel. This is what we should expect, because the smaller the distance between two periodic filaments, the smaller the contribution of viscous dissipation compared to the asymmetric force generated by each filament. This is especially clear for intermediate values of T , where filaments spaced apart of $L = 2$ generate a significant average net flow of 0.173.

We can look at the average velocity fields in order to better comprehend the behaviour of the system.

Starting from $T = 0.6$, which belongs to the first of the zones already defined, the average u and v fields are plotted in figs. 4.9 and 4.10 respec-

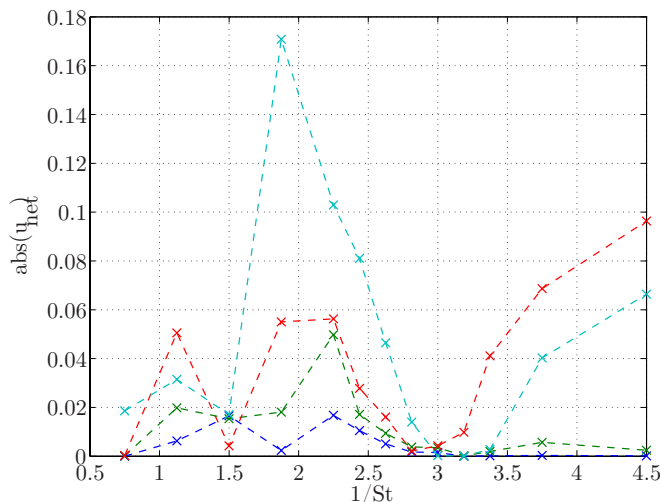


Figure 4.8: Absolute value of average net velocity u_{net} versus $1/St$, for $L = 12$ (blue), $L = 6$ (green), $L = 3$ (red) and $L = 2$ (light blue).

tively. We can see a similar vertical jet-like effect on the fluid, not much influenced by the length of the channel; we can expect that, because of its orientation, it will be influenced more by the value of $2h$: this will be confirmed in the next section.

For $T = 1.5$, the value that shows the maximum net velocity, the results are very much influenced by L . The average angle has a peak for $L = 3$, while the net velocity shows a peak for $L = 2$. In figs. 4.11 and 4.12 the average u and v fields are plotted respectively.

We can see that for large L the filament behaves again as a vertical jet, stronger than in the previous case; as the channel length drop, this configuration seem to be not stable anymore (starts to be bent for $L = 6$; this results in a small net flow in 4.7), so that the asymmetric vortices again are generated (most clear for $L = 2$). In the latter case the upper part of the channel is dragged by the top half of the vortex, thus a net flow origins.

For $T = 2.1$, which corresponds to the resulting maximum average

4.3. Channel length

angle, we would expect to see small changes in the average fields, because the value of the $\bar{\theta}$ decreases only slightly as L decreases. This is true, comparing figs. 4.13 and 4.14. The filament seem to be exerting only a local effect on the fluid, there are no jet-like effects; this is clear especially in figs. 4.13d and 4.14d where most part of the channel is unaffected by the filament presence.

Lastly, for $T = 3.6$ (figs. 4.15 and 4.16), we can separates two regimes, one for channel long enough is characterized by symmetric behaviour and no net flow or significant average angle. In this case the filament acts, as we already noted, as pushing the fluid towards the sides of the channel. The resulting motion is similar to a convective motion, with vertical rising streams on the two sides of the filament. If the distance between two filaments is not enough these rising streams will merge at the periodic boundaries of the channel. Letting L decrease more and this configuration seem to be not stable anymore, yielding to a new asymmetric flow characterised by significant $\bar{\theta}$ and u_{net} . To help us understand better the flow, in fig. 4.17 the streamlines path have been superimposed to the average u field for $L = 3$. The streamlines have been obtained using the Matlab function *streamline*.

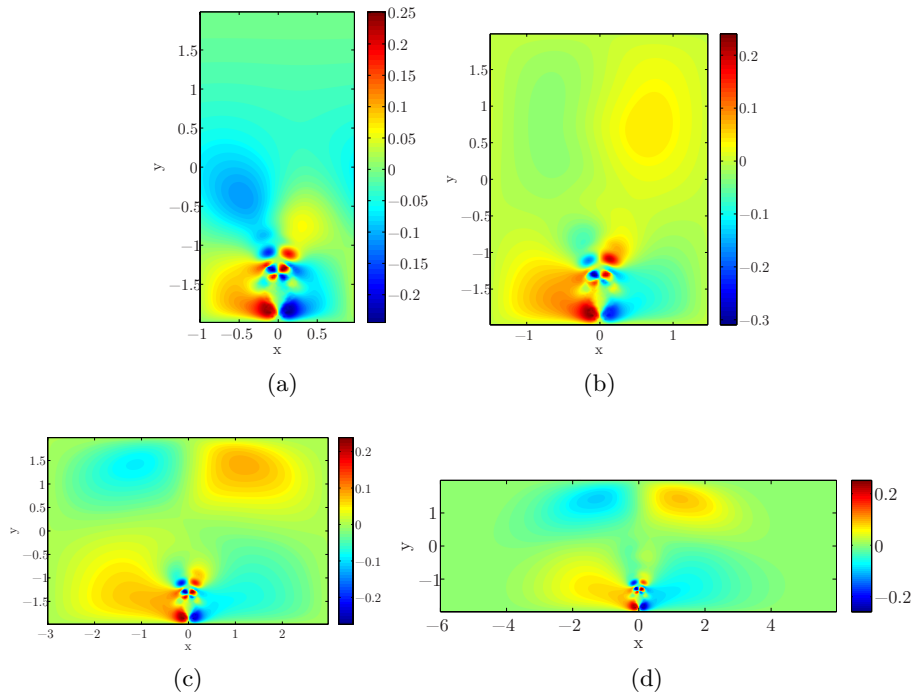


Figure 4.9: Average u field for $T = 0.6$ and $L = 2$ (a), $L = 3$ (b), $L = 6$ (c) and $L = 12$ (d).

4.3. Channel length

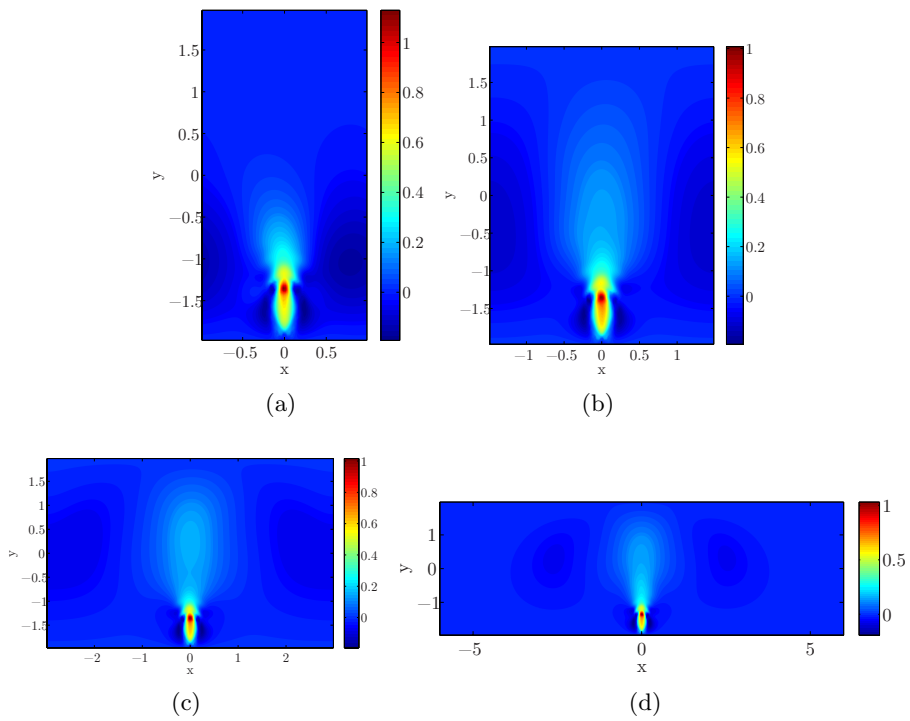


Figure 4.10: Average v field for $T = 0.6$ and $L = 2$ (a), $L = 3$ (b), $L = 6$ (c) and $L = 12$ (d).

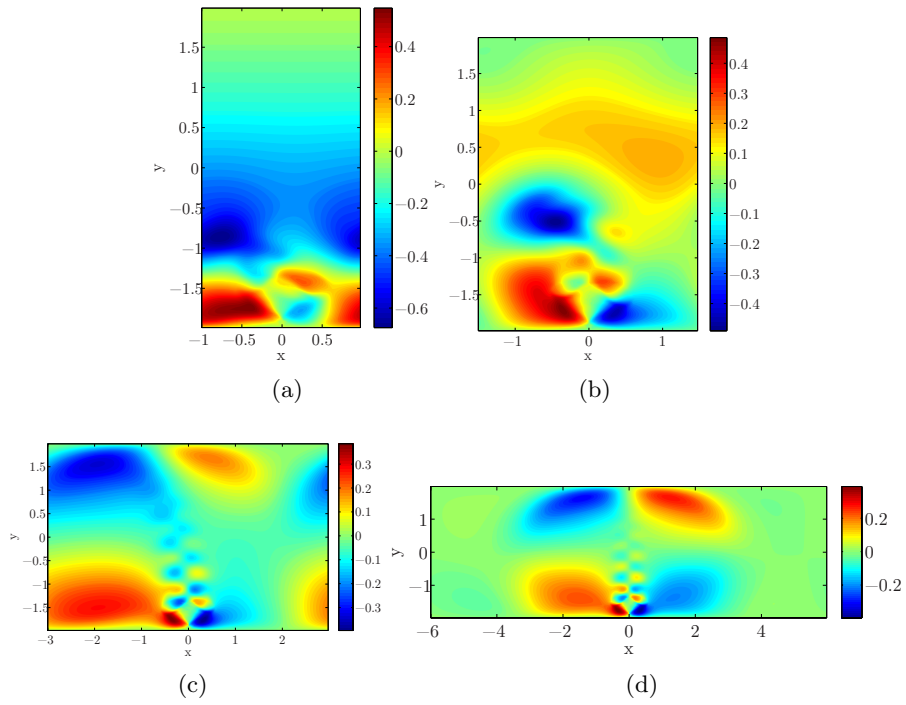


Figure 4.11: Average u field for $T = 1.5$ and $L = 2$ (a), $L = 3$ (b), $L = 6$ (c) and $L = 12$ (d).

4.3. Channel length

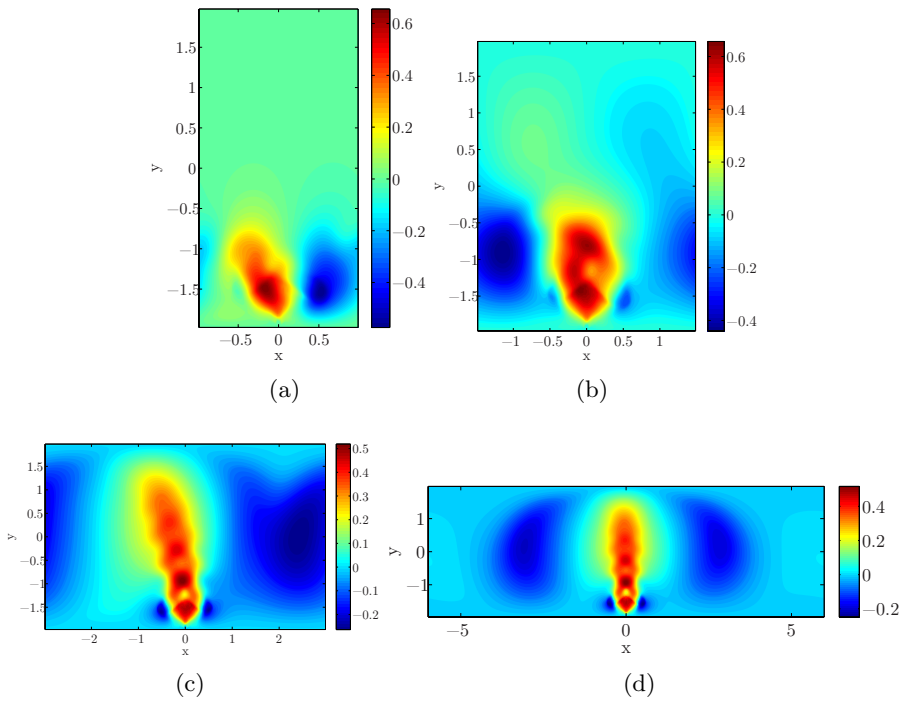


Figure 4.12: Average v field for $T = 1.5$ and $L = 2$ (a), $L = 3$ (b), $L = 6$ (c) and $L = 12$ (d).

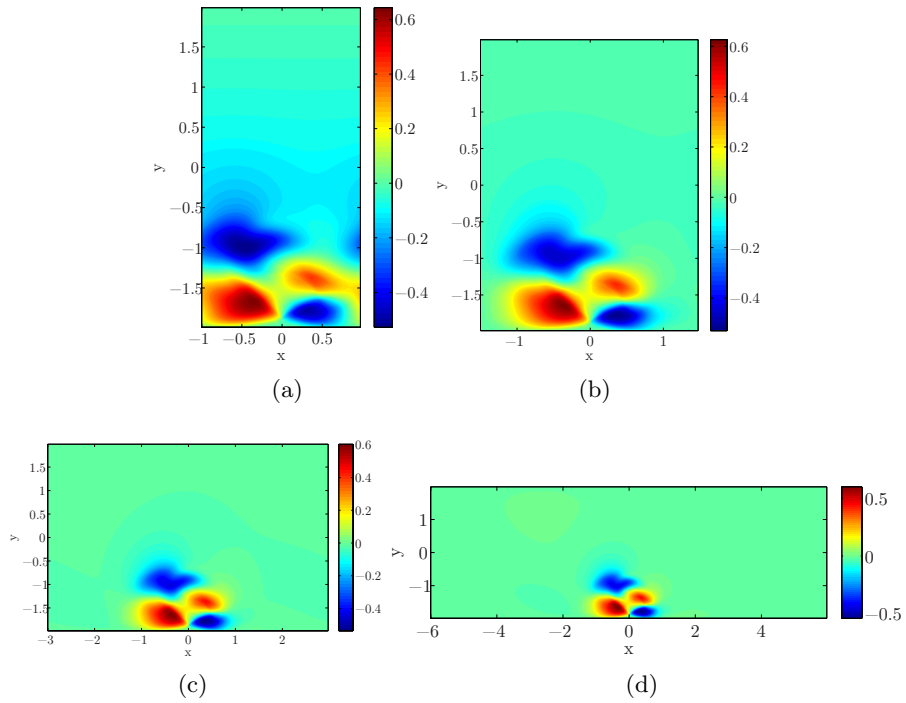


Figure 4.13: Average u field for $T = 2.1$ and $L = 2$ (a), $L = 3$ (b), $L = 6$ (c) and $L = 12$ (d).

4.3. Channel length

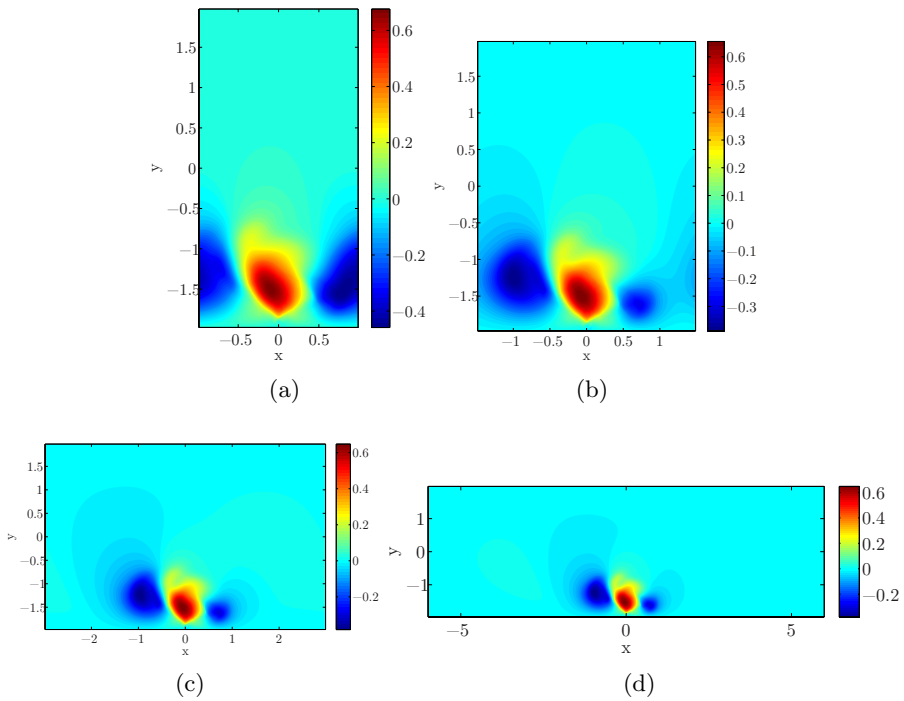


Figure 4.14: Average v field for $T = 2.1$ and $L = 2$ (a), $L = 3$ (b), $L = 6$ (c) and $L = 12$ (d).

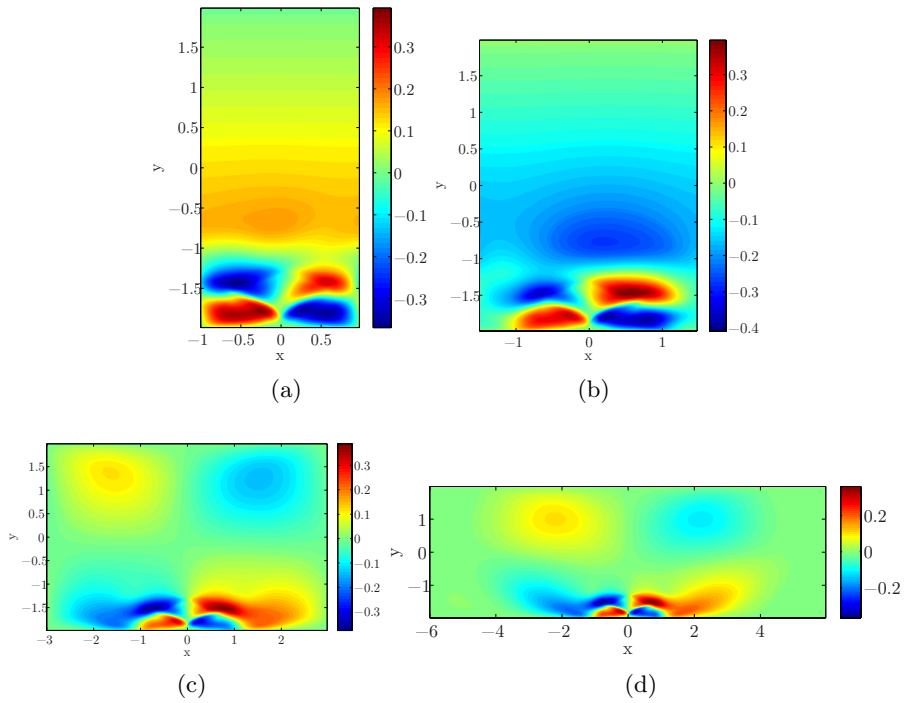


Figure 4.15: Average u field for $T = 3.6$ and $L = 2$ (a), $L = 3$ (b), $L = 6$ (c) and $L = 12$ (d).

4.3. Channel length

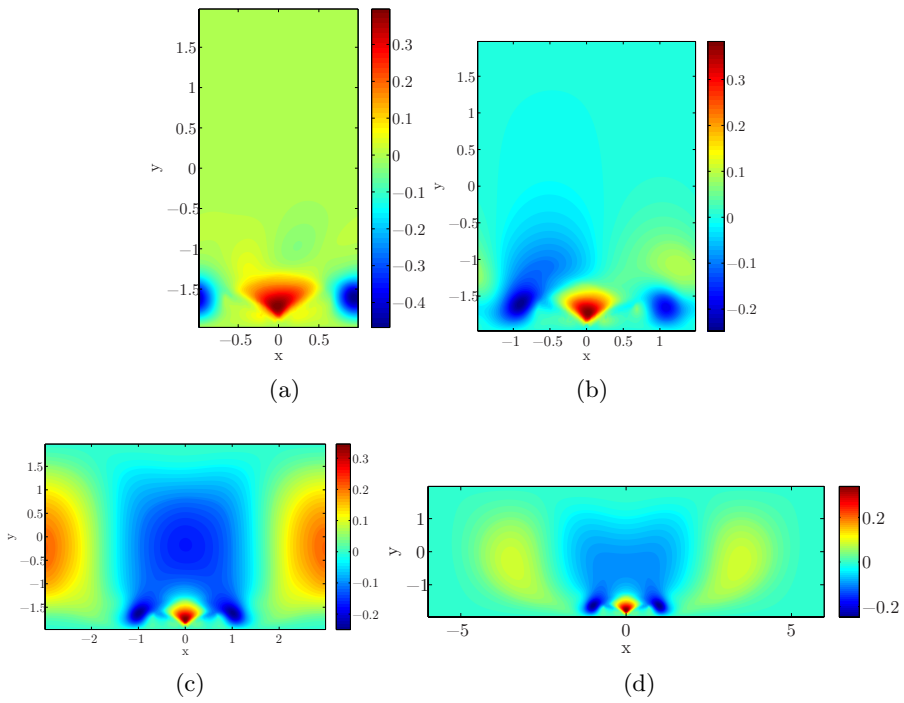


Figure 4.16: Average v field for $T = 3.6$ and $L = 2$ (a), $L = 3$ (b), $L = 6$ (c) and $L = 12$ (d).

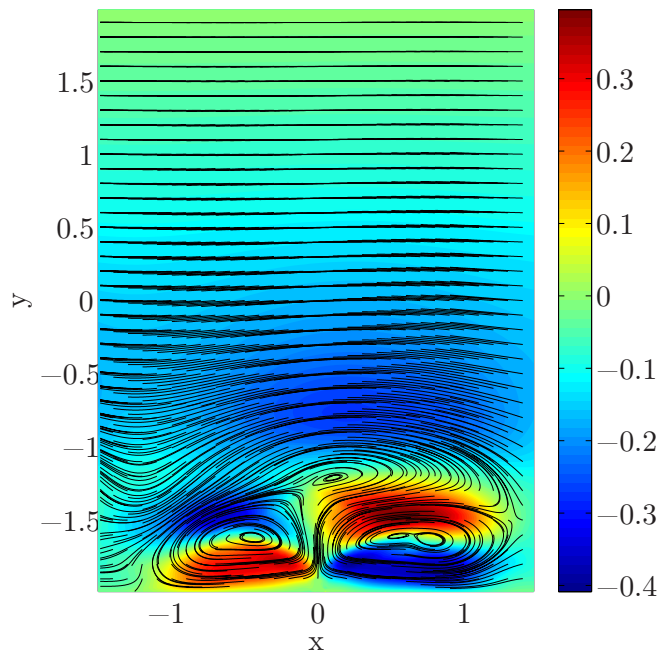


Figure 4.17: Streamlines path overimposed to the average u field for $L = 3$ and $T = 3.6$. The streamlines have been obtained using the Matlab function *stramline*.

4.4. Channel height

4.4 Channel height

The channel height, $2h$ has been kept fixed until now, its valued being 4. In this section we will investigate its influence on the simulations. The set of parameters that have been used are listed in tab 4.1.

Parameter	Value
<i>Channel</i>	
Length, L	2
Height, $2h$	2, 4, 8
Number of filaments, N_f	1
<i>Filament</i>	
Length, L_f	0.8
Density, ρ_f	0
Elastic stiffness, K_{elas}	100
Bending stiffness, K_{beam}	$5 \cdot 10^{-3}$
<i>Flow</i>	
Characteristic velocity, \bar{u}_{max}	1
Reynolds number, Re	200
Time-period, T	0.6, 0.9, 1.2, 1.5, 1.8, 2.1, 2.7, 3.6

Table 4.1: Parameters used for the simulations.

Looking at the average angle $\bar{\theta}$ as a function of $1/St$ (fig. 4.18), we can see that for large values of $1/St$ the height of the channel $2h$ has small influence on $\bar{\theta}$; for small values of $1/St$, on the other hand, the differences grow bigger.

One way to explain this is to recall that for short periods the filament acts on the fluid pushing it towards the top of the channel, so that the distance from the filament end to the top of the channel has a rather strong impact on the system. On the other hand, for long time periods the filament pushes the fluid towards the left and right sides of the channel, so that its height is less relevant. In figs. 4.20a, and 4.20b the average u and v fields are shown respectively, for $2h = 2$. They confirm that that the filament

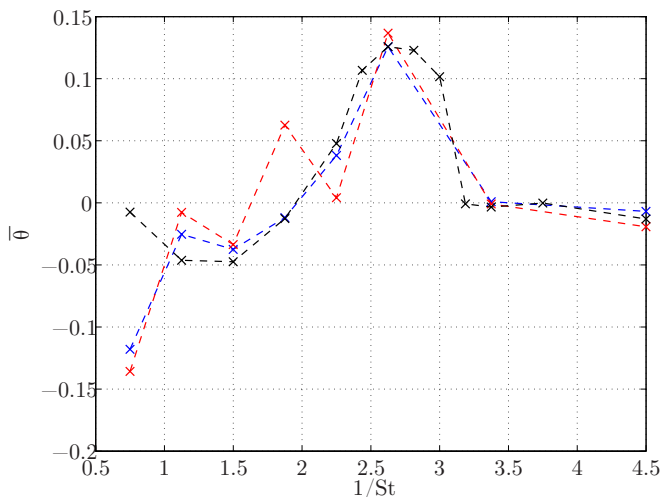


Figure 4.18: Average angle $\bar{\theta}$ as a function of $1/St$ for $2h = 2$ (red), $2h = 4$ (black, data from past simulations), $2h = 8$ (blue).

basically act as a jet whose height is enough to interact with the top wall (cf. with fig. 4.10a).

Regarding the average velocity u_{net} , the major differences are found for $1/St = 1.875$, that is when the maximum net flow is reached (fig. 4.19). The lowest value is found for the least high channel, which can be related to the presence of the top boundary layer too close to the filament, so that the asymmetric vortex magnitude is lowered. Comparing the other two cases, we can state that for $2h = 4$ the average velocity is larger, but since its value for $2h = 8$ is larger than half of the former one, we can derive that the biggest net flow is found for $2h = 8$. In figs. 4.21a and 4.21b the average u field is compared for the last two cases. We can see that for $2h = 8$ there is a bigger zone, in the upper part of the channel, where the average u value is small and negative; this has both the effect to increase the total net flow and to decrease the average net velocity magnitude.

4.4. Channel height

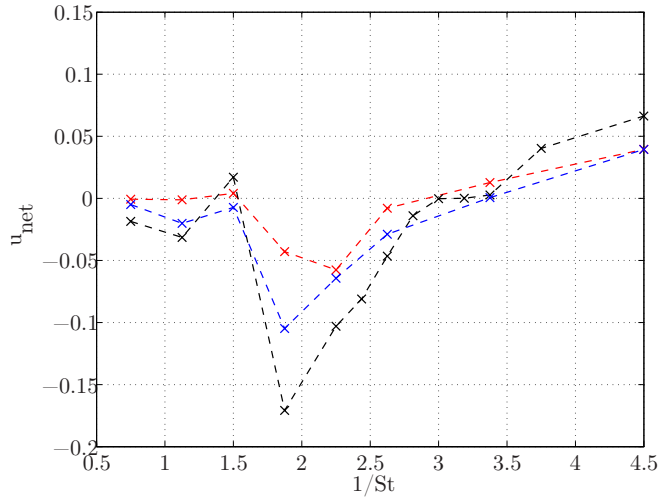


Figure 4.19: Net velocity u_{net} as a function of $1/St$ for $2h = 2$ (red), $2h = 4$ (black, data from past simulations), $2h = 8$ (blue).

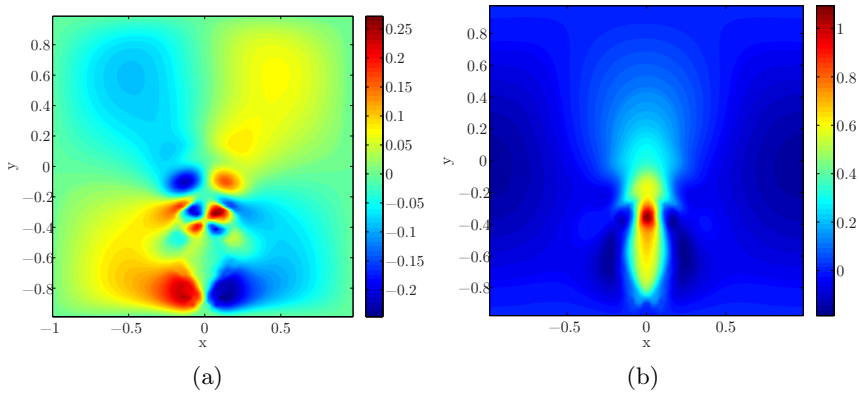


Figure 4.20: Average u field (a) and v field (b) for $T = 0.6$ and $2h = 2$. The filament creates a jet towards the top wall of the channel.

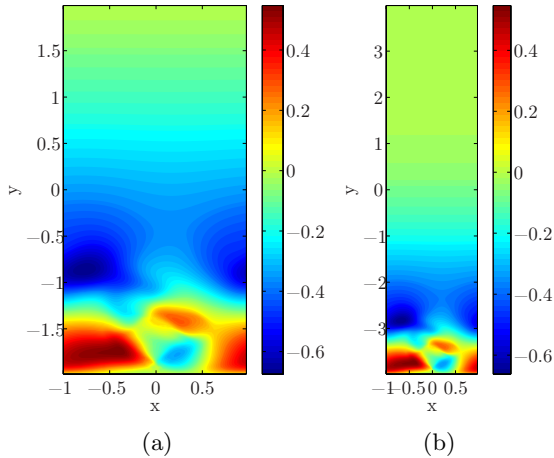


Figure 4.21: Average u field for $2h = 4$ (a) and $2h = 8$ (b); $1/St = 1.875$.

4.5 Bending stiffness

The bending stiffness K_{beam} has, until now, remained constant at $k_{beam} = 0.005$. In this section we will investigate the results of a ten-fold increase of the bending stiffness, up to $K_{beam} = 0.05$. The other parameters are the one listed in 3.2, with $L = 2$.

The obtained average angle $\bar{\theta}$ and average net velocity u_{net} are plotted in figs. 4.22 and 4.23 respectively.

Their general shape is similar, albeit they differ from each other noticeably. The average angle is generally larger when simulating the stiffer filament, but it has the same general shape; we can say the same for the shape of u_{net} , even if in the region from $1/St = 2$ to $1/St = 3$ the net flow is two to four times the one observed for the softer filament.

Analysing the average net fields for $T = 2.1$ (that is $1/St = 2.625$), fig. 4.24, we can observe that it is way more similar to the one observed, in the case of softer filament, for $T = 1.5$ instead of $T = 2.1$ (cf. with figs. 4.11, 4.12, 4.13, 4.14). This can be explained with the fact that, as the stiffness

4.6. Reynolds number

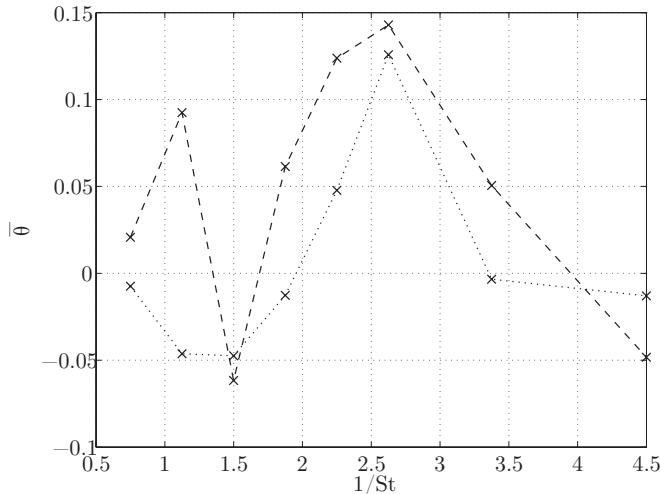


Figure 4.22: Average angle $\bar{\theta}$ as a function of $1/St$ for $K_{beam} = 0.005$ (dotted line) and $K_{beam} = 0.05$ (dashed line).

grows, the filament displacement due to the pulsatile flow gets smaller, so that in order to get a similar movement a longer T is needed.

4.6 Reynolds number

Until now the Reynolds number has always remained the same, at $Re = 200$; in this section we will study the influence of these parameters. The parameters used in this set of simulations are those listed in tab. 4.2.

We measured the resulting average angle $\bar{\theta}$ and the average net velocity u_{net} , which are shown in figs. 4.25 and 4.26 respectively.

We can say that for low values of Re the results show no asymmetry, then starting from $Re = 60$ we can see a (albeit very small) non zero net flow; for higher values of Re the asymmetric behaviour gets more and more noticeable, but there seems not to be a clear threshold that separates the asymmetric part from the symmetric one.

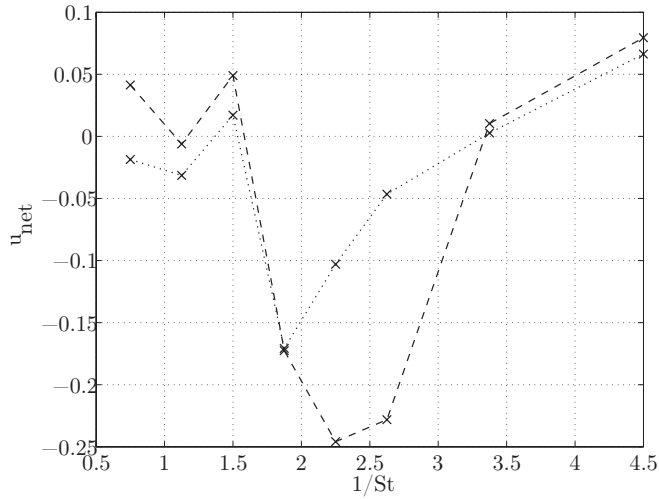


Figure 4.23: Average net velocity u_{net} as a function of $1/St$ for $K_{beam} = 0.005$ (dotted line) and $K_{beam} = 0.05$ (dashed line).

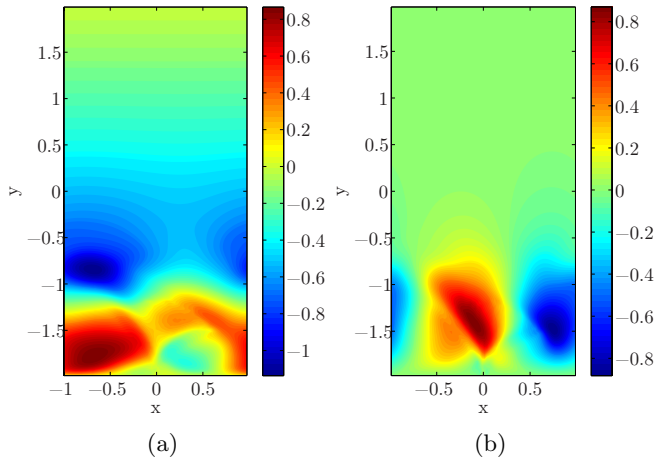


Figure 4.24: Average u (a) and v (b) fields for $T = 2.1$ and $K_{beam} = 0.05$.

4.6. Reynolds number

Parameter	Value
<i>Channel</i>	
Length, L	2
Height, $2h$	4
Number of filaments, N_f	1
<i>Filament</i>	
Length, L_f	0.8
Density, ρ_f	0
Elastic stiffness, K_{elas}	100
Bending stiffness, K_{beam}	$5 \cdot 10^{-3}$
<i>Flow</i>	
Characteristic velocity, \bar{u}_{max}	1
Reynolds number, Re	25, 50, 60, 70, 75, 80, 90, 100
Time-period, T	1.8

Table 4.2: Parameters used for the simulations.

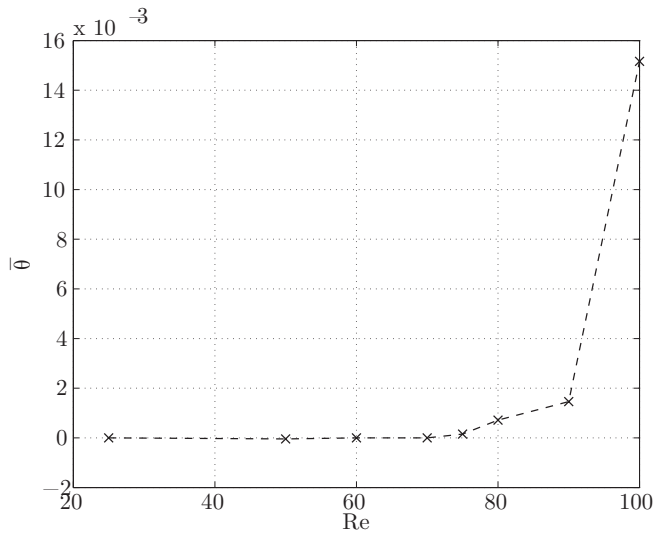


Figure 4.25: Average angle $\bar{\theta}$ as a function of Reynolds number Re .

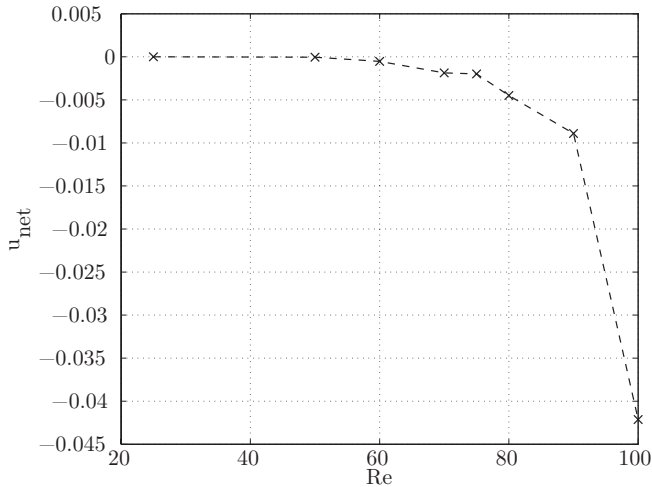


Figure 4.26: Net velocity u_{net} as a function of Reynolds number Re .

4.7 Multiple filaments

Imposing the periodic boundary conditions on the left and right sides of the channel we are virtually simulating an infinite set of equispaced filaments. Doing so we also impose that each filament moves exactly the same as the other ones. We will now simulate more than one filament in the same periodic window, so that they will be free to move differently from each other. The simulation parameters are listed in tab 4.3.

To describe the differences in the filaments movements we calculated the maximum difference in the x position of the free-end of every couple of filaments. In the case of two filaments, this means:

$$|\Delta x|(t) = |X_1(e, t) - X_2(e, t) + d|, \quad (4.2)$$

where e is the index that denotes the end node of the filament. For more than two filaments the same operation is done for every couple of filaments and then the maximum value for every time-step is taken.

4.7. Multiple filaments

Parameter	Value
<i>Channel</i>	
Length, L	2
Height, $2h$	4
Number of filaments, N_f	2, 3, 4
Distance between filaments, d	2
<i>Filament</i>	
Length, L_f	0.8
Density, ρ_f	0.
Elastic stiffness, K_{elas}	100
Bending stiffness, K_{beam}	$5 \cdot 10^{-3}$
<i>Flow</i>	
Characteristic velocity, \bar{u}_{max}	1
Reynolds number, Re	200
Time-period, T	1.8

Table 4.3: Parameters used for the simulations.

In fig. 4.27 the results for the four filaments case are shown; the differences between each filaments are negligible and almost comparable to the numerical precision of the code.

Another test has been run with two filament using two slightly different initial positions. The absolute value of the difference between the movement of each free-end have been again measured and plotted in fig 4.28. After the initial transient the differences get smeared out, so the two filaments tend to behave in the same way.

We can then say that the periodic boundary conditions we impose are not different from what we would observe if we would simulate a quasi-infinite number of filaments equispaced.

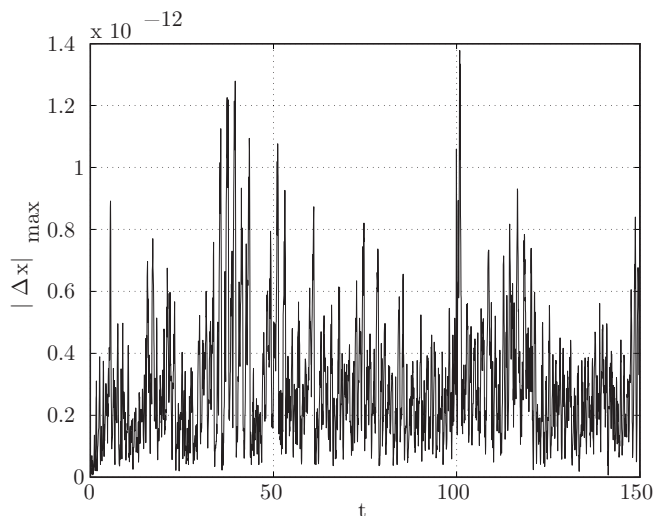


Figure 4.27: Maximum difference in the behaviour of the filaments versus time.

4.8 Filaments on both sides

We will now conclude this section studying the effect of the presence of filaments on both sides of the channel. The parameters used are the one listed in tab. 4.1, with $2h = 4$. In figs. 4.29 and 4.30 the average angle and the average net velocity are plotted, respectively.

Comparing the average angle of each filament, we can see that for large T they get to the same values which are very close to the ones obtained in the case with one filament. This means that in these conditions there is not a strong interaction between the two filaments. On the other hand, for small T , the values are quite different from each others, meaning that a significant interaction is taking place. This is something we should expect: as we saw in sec. 4.2 for short T the filaments move the fluid towards the opposite wall of the channel, so towards the other filament; again, for large T the fluid is pushed towards the sides, so the interaction is less probable.

4.8. Filaments on both sides

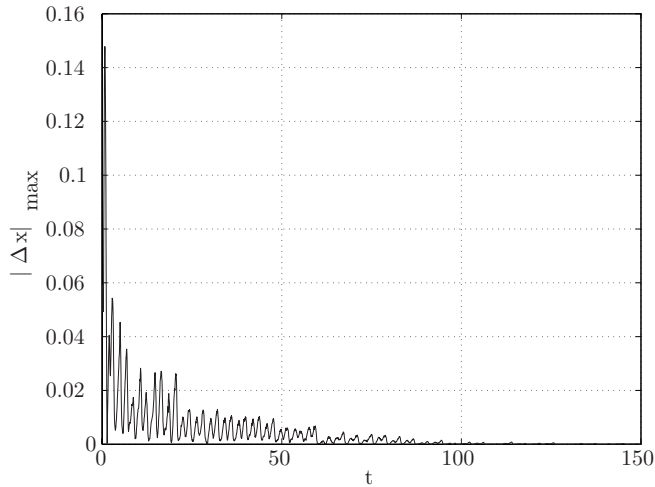


Figure 4.28: Maximum difference in the behaviour of the filaments versus time, for slightly different initial positions.

As for u_{net} it is interesting to see that the peak is roughly twice in magnitude compared to the one filament case, so that we can say that both filaments act coherently on the flow. The resulting average flow fields are plotted in fig. 4.31

As we can see in the center zone of the channel a fast flowing zone exists, with velocity values bigger than 0.6, which is 60% of \bar{u}_{max} .

Again to better understand the dynamics of the flow, we can superimpose the path of the streamlines to the u average field, yielding to the plot in fig. 4.32. The streamlines are mostly horizontal in a large region; in this space the net flow generated could efficiently transport particles along the channel.

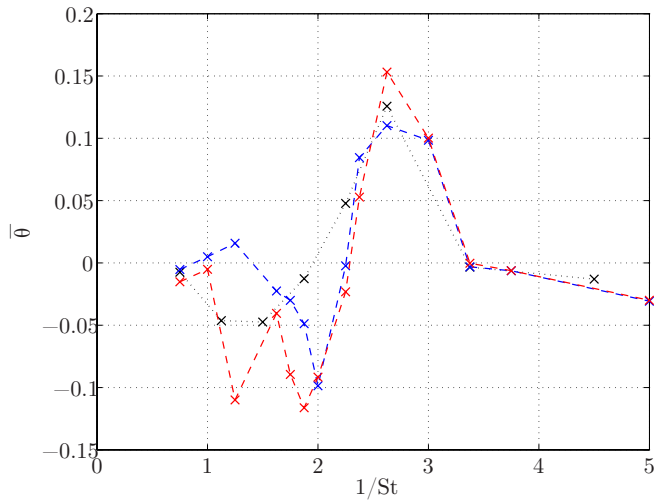


Figure 4.29: Average angle $\bar{\theta}$ versus $1/St$ for the lower filament (blue) and the upper filament (red), compared to the case of one filament (dotted line).

4.8. Filaments on both sides

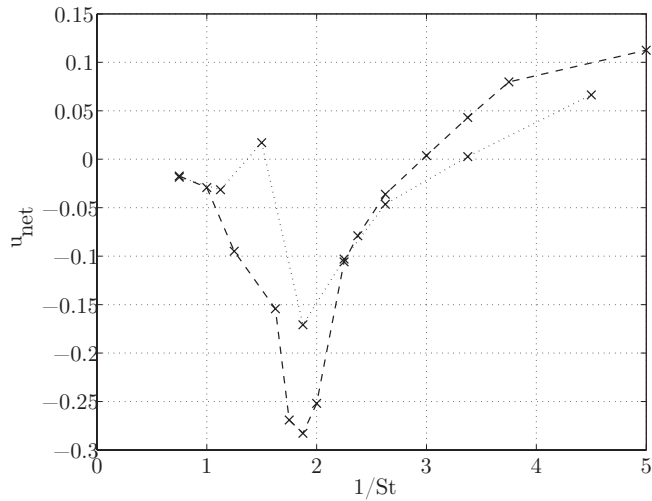


Figure 4.30: Average net velocity u_{net} versus $1/St$ for the two filaments case (dashed line) compared to the case of one filament (dotted line).

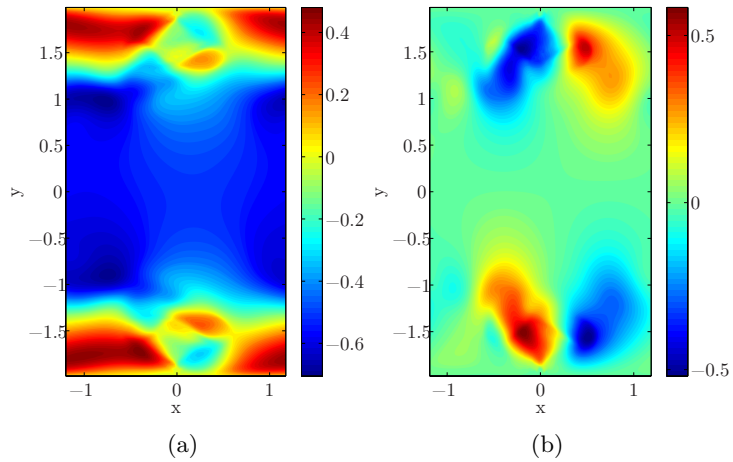


Figure 4.31: Average u (a) and v (b) fields for $T = 1.5$.

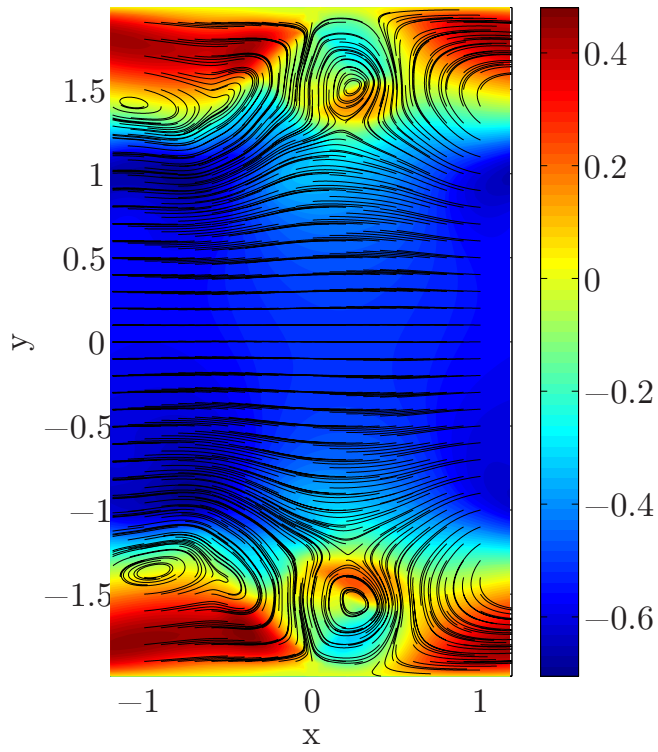


Figure 4.32: Streamlines path overlaid to the u average field, for $T = 1.5$.

Chapter 5

Further analysis

Deeper studies have been carried out based on the results that we showed in the past sections. We will use the Finite-Time Lyapunov Exponent (FTLE) technique first, then we will propose a model for the global effect of the filament moving inside the channel.

5.1 FTLE

The Lyapunov exponent of a dynamical system is a quantity that characterizes the rate of separation of infinitesimally close trajectories. Quantitatively, two trajectories with initial separation $\delta\mathbf{x}_0$ can diverge at a rate given by:

$$|\delta\mathbf{x}(t)| \approx e^{\lambda t} |\delta\mathbf{x}_0| \quad (5.1)$$

where λ is the Lyapunov exponent. The Lyapunov exponent is generally defined as:

$$\lambda = \lim_{t \rightarrow \infty} \lim_{\delta\mathbf{x}_0 \rightarrow 0} \frac{1}{t} \ln \frac{|\delta\mathbf{x}(t)|}{|\delta\mathbf{x}_0|}. \quad (5.2)$$

In Fluid Dynamics, usually, the Finite-Time Lyapunov Exponent (FTLE) is used. It measures the rate of separation of infinitesimally close trajectories over the time interval $[t, t + \tau]$, τ being the time spent following the trajectories before calculating the exponent. The FTLE is generally

5.1. FTLE

function of space and time; in our case, however, we will apply it to the time-averaged velocity field, so it will be function of space only. The obtained map indicates the rate of separation of massless particle starting close together, after being transported along the flow (advection) during the finite time interval τ . High values of the FTLE are found along repelling manifolds embedded in the flow. The manifolds determine the local behaviour of the flow and are called Lagrangian Coherent Structures (LCS). Contours of FTLE correspond to precise vortex boundaries and reveal LCS [29, 30] in a similar fashion as visualization techniques based on injection of “tracers”, such as dye or smoke.

In fig. 5.1 the working principle of this technique is showed for a double vortex flow between walls; it shows (a) the trajectories of three initially close points over a short interval of time. The points B and C are initially close, but since they are located on either side of the vertical line separating the two vortices, they quickly diverge from each other when advected by the flow. On the other hand, the points initially located at A and B remain relatively close together when advected by the flow. The FTLE values are then plotted (b), confirming the existence of the vertical separating line characterized by high value of FTLE, and showing the vortices presence.

We mapped the FTLE for four values of T and two values of L , obtaining eight configurations, whose general behaviour can be summarized as in table 5.1. The other parameters are the ones listed in tab. 3.2.

In Figs. 5.2 and 5.3 the resulting FTLE fields are plotted, and we can compare them with the general behaviour of the system. To obtain the plots we used the averaged velocity fields.

Starting from $L = 12$, for $T = 0.6$ and $T = 3.6$ the symmetric behaviour of the system is confirmed by the FTLE contours; for $T = 1.5$ the existence of a stronger jet-like effect is clear and also the small asymmetry that comes with it; for $T = 2.1$ the asymmetry is way more pronounced and also the asymmetric vorticious structures are properly outlined. It is interesting to notice that in all the cases there is a line characterized by higher values of FTLE that begins with the clamped end of the filament; this is in agreement with the explanation we gave for the two-vortices setup: since the flow can not cross the filament, its presence will make the trajectory of two particles

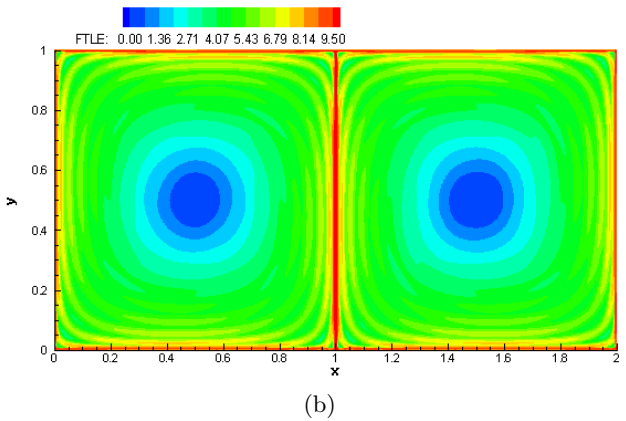
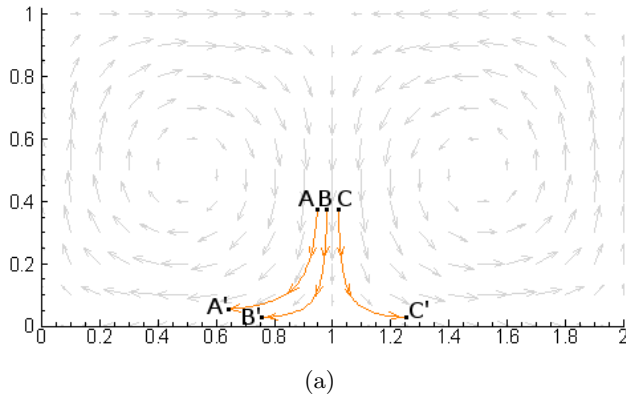


Figure 5.1: Trajectories of three initially close points (a); to be noticed how the points B and C quickly diverge from each other, compared to A and B. The FTLE field associated to the flow (b) outlines the vorticious structures and the vertical separating line. Courtesy of <http://mmae.iit.edu/shadden/LCS-tutorial/>.

5.1. FTLE

	$L = 12$	$L = 2$
$T = 0.6$	No asymmetry in the movement of the filament; filament acting as a narrow vertical jet.	No asymmetry in the movement of the filament; negligible net flow; filament acting as a narrow vertical jet.
$T = 1.5$	Small asymmetry in the movement of the filament; filament acting as a stronger vertical jet.	Small asymmetry in the movement of the filament; very significant net flow; filament acting as a stronger vertical jet.
$T = 2.1$	Very significant average angle of the filament; generation of asymmetric vorticious structures.	Very significant average angle of the filament; small net flow; generation of asymmetric vorticious structures.
$T = 3.6$	Small asymmetry in the movement of the filament.	No asymmetry in the movement of the filament; no net flow.

Table 5.1: General behaviour of the system for chosen values of L and T .

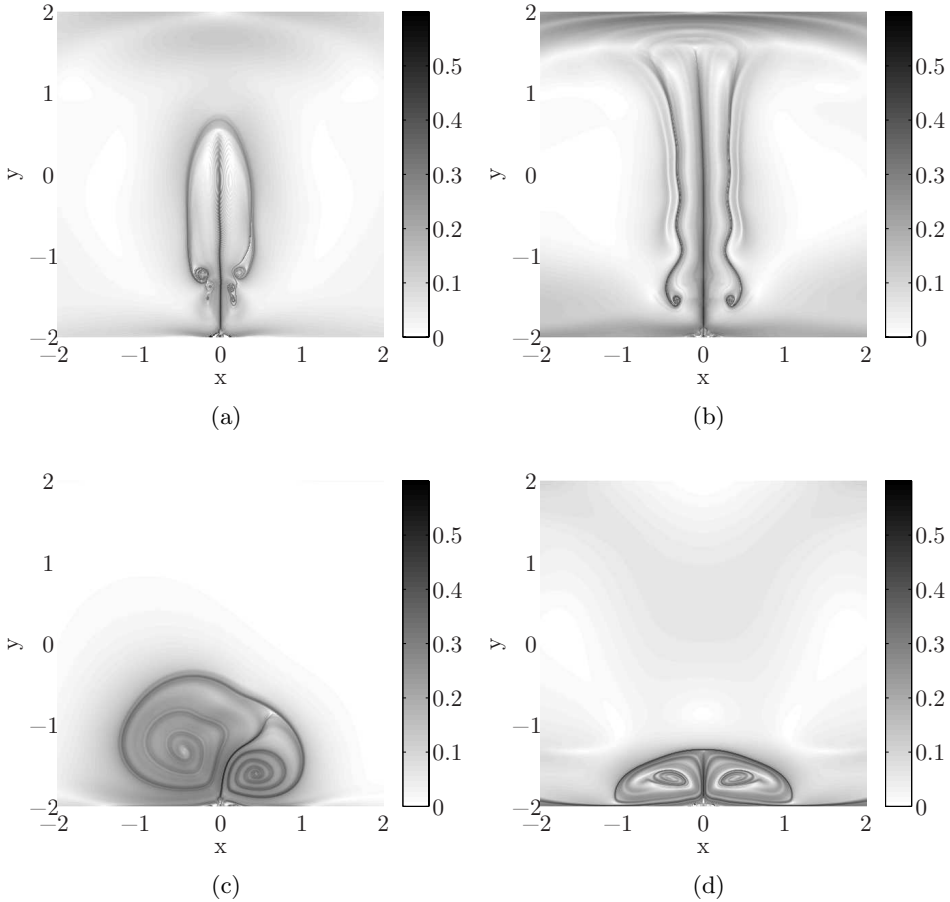


Figure 5.2: FTLE values for $L = 12$ and $T = 0.6$ (a), $T = 1.5$ (b), $T = 2.1$ (c), $T = 3.6$ (d). Only the central area of the domain is plotted, between $x = -2$ and $x = 2$.

5.1. FTLE

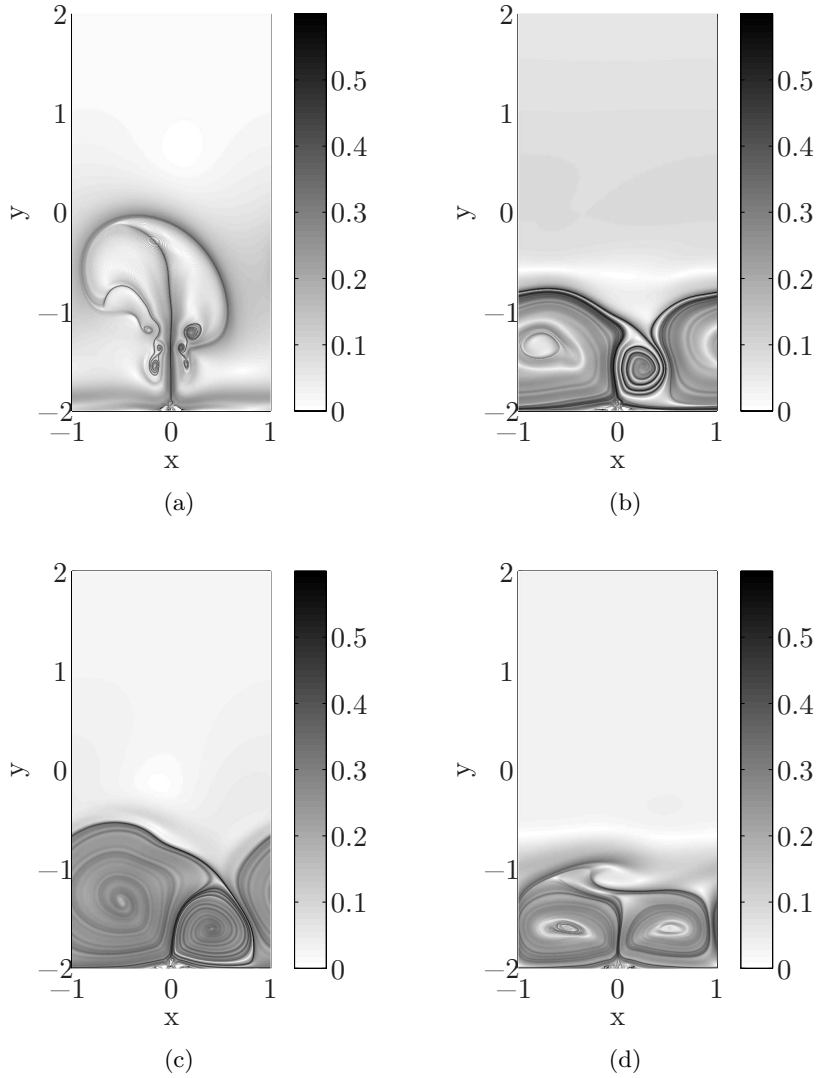


Figure 5.3: FTLE values for $L = 2$ and $T = 0.6$ (a), $T = 1.5$ (b), $T = 2.1$ (c), $T = 3.6$ (d).

near to the filament but on different sides diverge significantly. This darker line also outlines the filament when its movement is asymmetric: in fig. 5.2c the line is bent towards the right as the filament is, on average.

Now looking at the case of $L = 2$, in which the interaction between filaments is stronger and the generated net flow is bigger, we can again compare the FTLE contours with resulting flow. For $T = 0.6$ and $T = 3.6$ we see qualitatively similar results compared to the ones for $L = 12$; for $T = 2.1$ we can again outline the bent darker separation line that is bent towards the right as the filament is, while the vorticious structures maintain the shape we just observed; for $T = 1.5$ the biggest difference is found compared to fig. 5.2b: the jet-like effect of the filament turns into asymmetric vortices able to generate a steady streaming. Very interesting is the fact that in this case, the separating darker line is almost vertical, in agreement with the filament showing very small asymmetry in its movement.

The FTLE allowed us to better visualize the flow structures generated in the channel and confirmed our previous observation, showing good agreement with the results already obtained.

5.2 Modelling the filament

As we showed before and we confirmed through the analysis of FTLE data, the maximum magnitude of net flow is reached for values of T that does not generate a strongly asymmetric motion of the filament. Because of this, asymmetry in its movement can't be accounted as the cause of the relatively strong net flow measured. To look for a reason we analysed again the average flow field of an isolated filament led by a pulsatile flow, for $T = 1.5$, which is shown in fig. 4.12d. In this circumstance, the filament acts on average as exerting a vertical force on the fluid, pushing it towards the top wall and generating a vertical jet inside the channel. This effect is maximum exactly for $T = 1.5$. To clarify whether or not this is the cause that drives the generation of net flow, we simplified our system into a model that takes into account only this effect. We took away both the filament and the pulsatile flow, and added, in a small region corresponding to the

5.2. Modelling the filament



Figure 5.4: Scheme of the simplified model, the elastic filament and the pulsatile flow are not taken into account and substituted by a vertical surface force acting on the shaded rectangle. To the left and right sides of the channel periodic boundary conditions are imposed.

upper half of the filament, a surface force pointing to the top, as sketched in fig. 5.4, maintaining the periodic boundary conditions on the sides of the channel. The model simulations have been run on COMSOL Multiphysics.

We run four simulations in order to reproduce the results found for $L = 12$, $L = 6$, $L = 3$ and $L = 2$, for $T = 1.5$. The comparison between the original results and the model are shown in figs. 5.8, 5.7, 5.6, 5.5, where the velocity fields are plotted together with the streamlines path.

The figures show that the results match remarkably well, considering the very high degree of simplification of the proposed model, where both the filament and the pulsatile flow are not considered. Also, the area where the vertical surface force is applied and the magnitude of this force are chosen as a first try, while they can be fine tuned to better model the filament effect on the pulsatile flow. For $L = 12$ and $L = 6$ there are minor differences between the two systems; for $L = 3$ and $L = 2$ the differences become noticeable, but still the velocity fields agree qualitatively with each other in

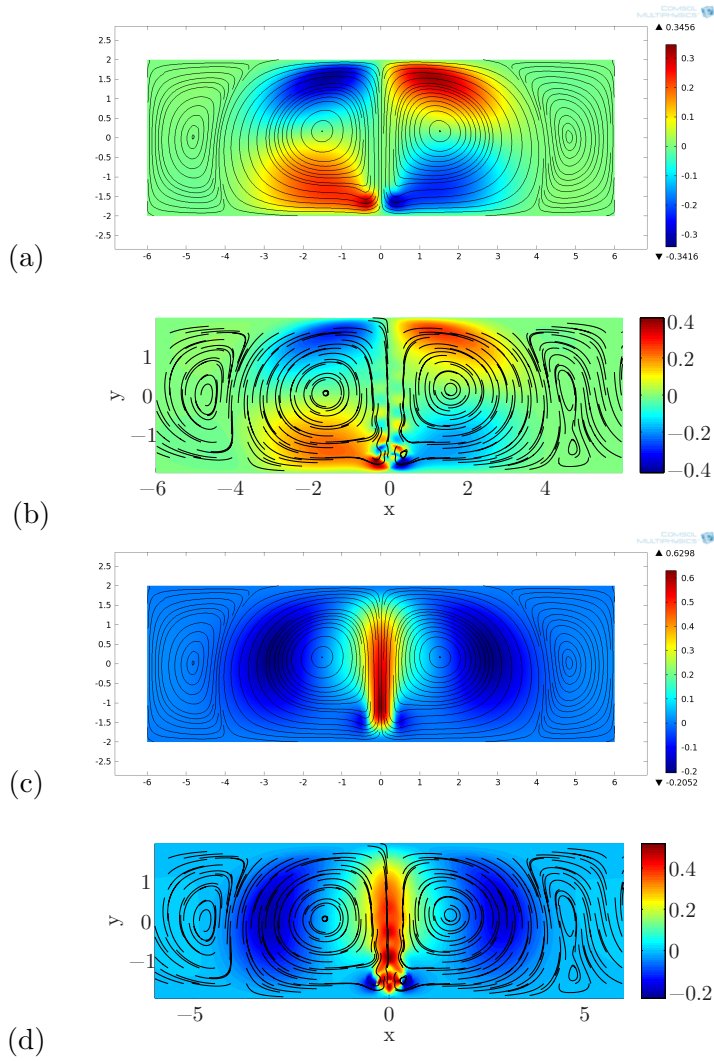


Figure 5.5: Average u and v velocity fields with streamlines obtained from the simplified model based on vertical jet and periodic boundaries (a and c), compared with the ones obtained simulating the complete system (b and d). $L = 12$.

5.2. Modelling the filament

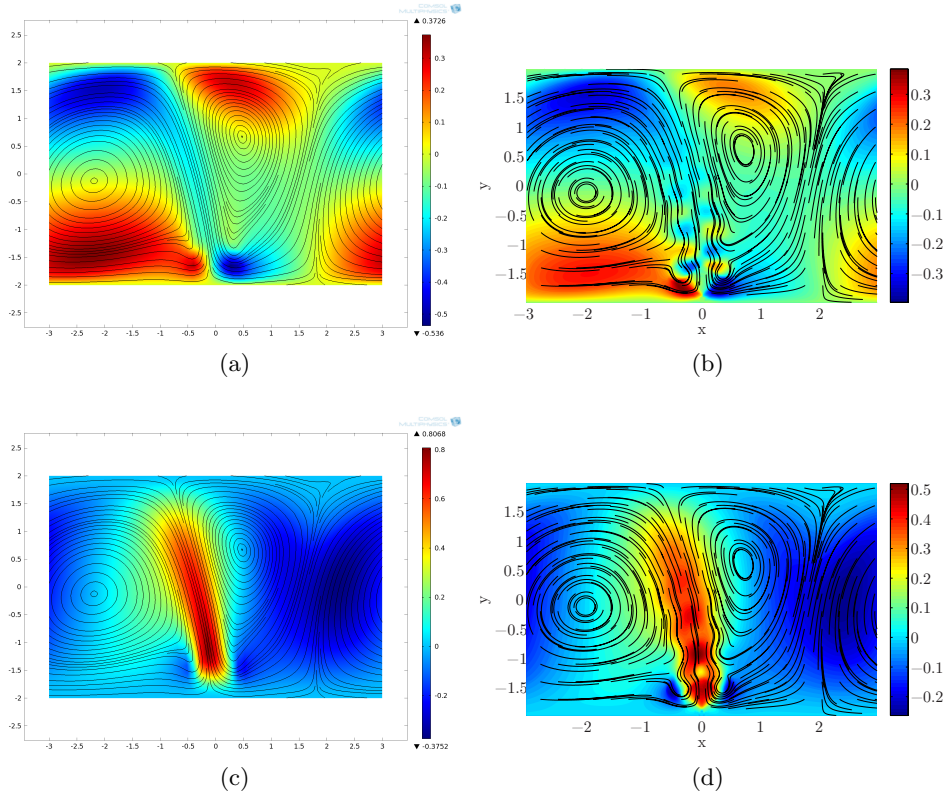


Figure 5.6: Average u and v velocity fields with streamlines obtained from the simplified model based on vertical jet and periodic boundaries (a and c), compared with the ones obtained simulating the complete system (b and d). $L = 6$.

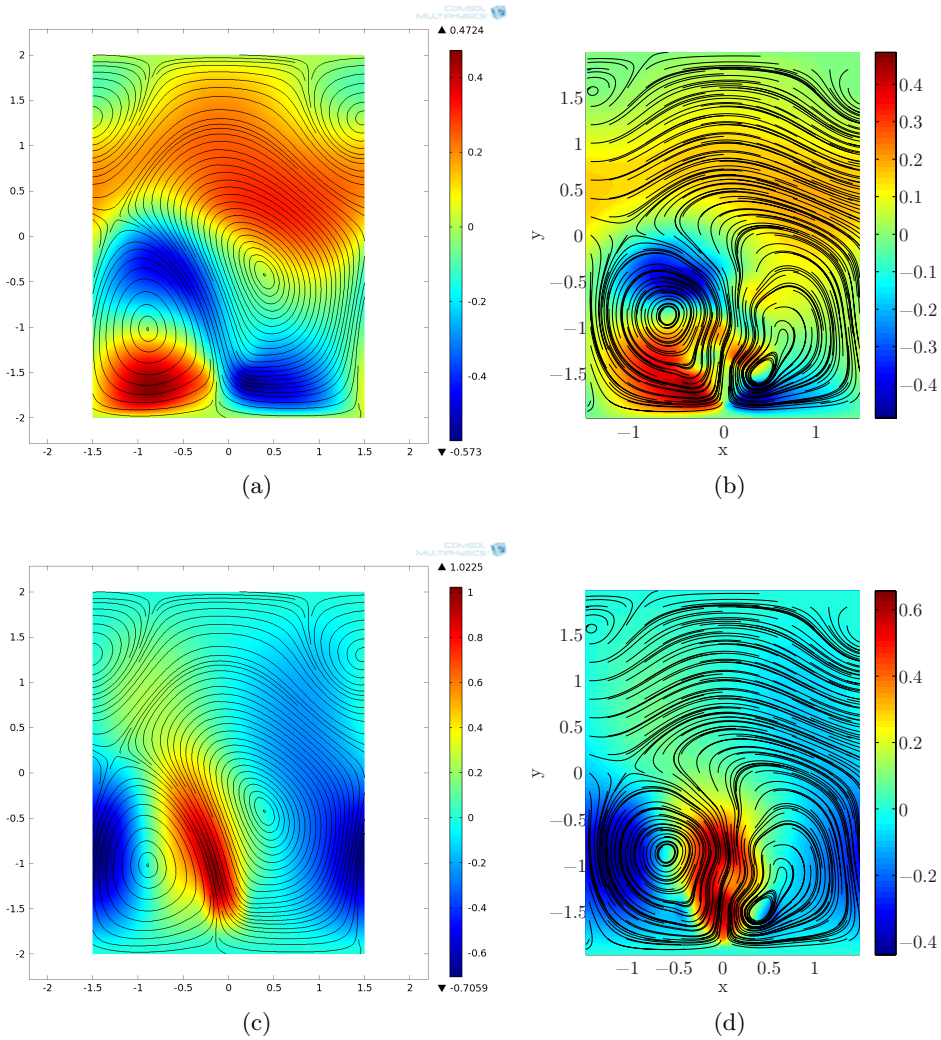


Figure 5.7: Average u and v velocity fields with streamlines obtained from the simplified model based on vertical jet and periodic boundaries (a and c), compared with the ones obtained simulating the complete system (b and d). $L = 3$.

5.2. Modelling the filament

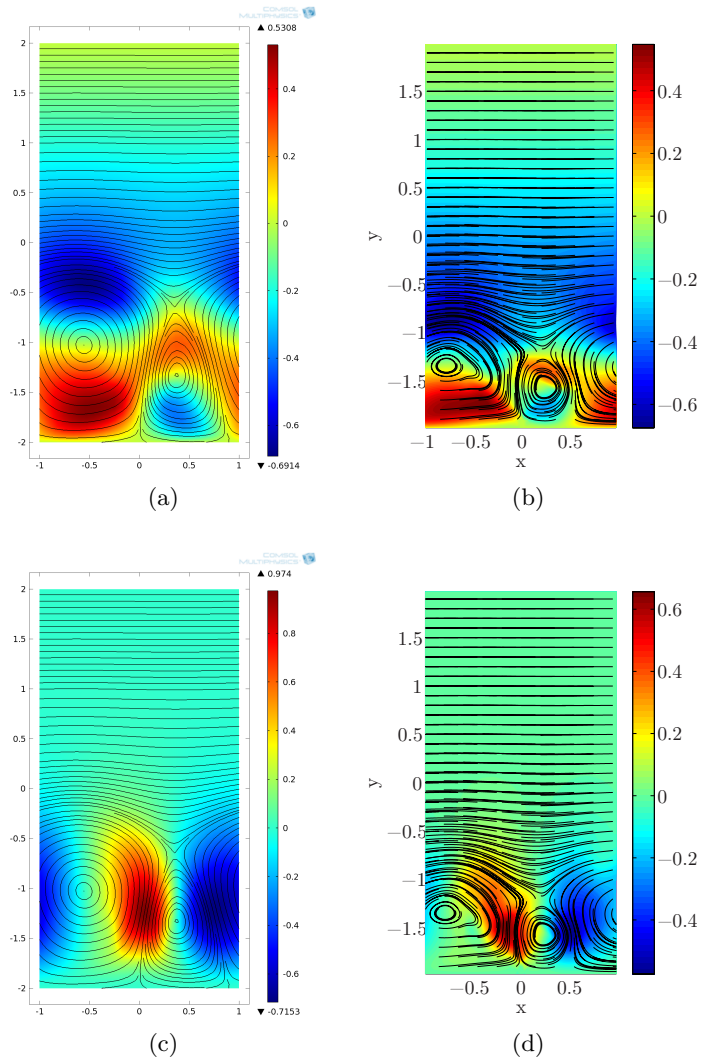


Figure 5.8: Average u and v velocity fields with streamlines obtained from the simplified model based on vertical jet and periodic boundaries (*a* and *c*), compared with the ones obtained simulating the complete system (*b* and *d*). $L = 2$.

both cases. Very interestingly, the velocity field obtained from the model shows a significant net flow, especially, as should be expected, for $L = 2$. In all the cases the magnitude of the net flow observed in the model is in good agreement with the one obtained from complete simulations.

Thus this model can be considered a valid representation of the original system and gives us a reason and an explanation for the strong peak net flow we measured in our test case: the pulsatile flow makes the filament flap in such a way that it has a strong propulsive effect on the fluid; this effect, when the periodic boundaries are close to the filament, gives birth to the asymmetric flow we observed, leading to significant net flow.

Chapter 6

Conclusions

We can now draw some conclusions from the analysis we have performed and the results obtained and outline possible future development of this analysis.

The case of study has proven to be very interesting in its dynamics, allowing us to investigate unforeseen effects and their consequences. The method we choose to carry out our investigation has demonstrated to be appropriate and reliable, and has allowed us to capture the behaviour of the system with adequate fidelity.

The results obtained are very interesting because they describe an unexpected effect of the interaction between the flexible filament and the pulsatile flow in which it is immersed, yielding an asymmetry of the system. Clear signs of symmetry breaking have arisen and the parameters sets that permit such effect have been isolated. We have observed two kinds of asymmetry, in the filament movement or in the channel average flow; the two of them are not necessarily present at the same time and we showed that there could be significant asymmetry in the channel velocity even if the filament flapping is essentially symmetric. The Finite Time Lyapunov Exponent analysis has confirmed our findings and allowed us better visualize the vortical structures present in the fluid domain.

A model has been proposed to simplify the original system into a much

Chapter 6. Conclusions

simpler one where we take into account the filament effects together with the pulsatile flow without introducing them explicitly in the simulations. This model has shown good agreement with the original system for the parameters sets that we have compared. In the future, our goal is to further investigate this interesting problem, broadening the space of parameters and implementing new techniques of analysis. Also, the model we have proposed can be extended and put to test with a more ample set of simulation results. Starting from the model, an interesting investigation would be to understand the reasons leading such a simple configuration to an asymmetric behaviour; this could also explain the symmetry breaking in the original case of study.

Acknowledgements

First of all, I would like to thank Professor Alessandro Bottaro for giving me the opportunity to write this thesis in collaboration with the Royal Institute of Technology of Stockholm. Also I'm grateful to him for his continuous support, for his availability, and for the patience he showed during the review of this thesis and for the great courses he teaches.

I would like to express my gratitude to Professor Shervin Bagheri and his PhD student Uģis Lācis for suggesting me a very interesting case of study and for helping and supporting me during the progression of the work in the best possible way. I also feel grateful to the other colleagues at KTH Mechanics that have allowed me to enjoy a great work environment.

I thank Professor Andrea Mazzino, Jan Pralits and Damiano Natali for the fruitful discussions.

I acknowledge the C. M. Leric Foundation for the generous funding they provided.

This thesis is also the final result of the five-years long course of studies at the University of Genoa, thus I would like to thank the fellow students that shared this experience with me, especially Giorgio and Alberto, of whom I hope not to lose the sight.

I am very thankful to my family and to my old and new friends, for having supported me in different but equally essential ways during these years.

Finally, I am profoundly grateful to Benedetta: without her this thesis would be the same, but I would not.

References

- [1] A. R. Collar, *The first fifty years of aeroelasticity*, Aerospace, 2-5, pp. 12-20, 1978.
- [2] Y. C. Fung, *An introduction to the theory of aeroelasticity*, Dover, 1994.
- [3] O. H. Amann, T. von Karman, G. B. Woodruff, *The failure of the Tacoma Narrows bridge*, Federal Works Agency, 1941.
- [4] F. B. Farquharson, F. C. Smith, G. S. Vincent, *Aerodynamic stability of suspension bridges with special reference to the Tacoma Narrows Bridge*, Bulletin, 1950.
- [5] S. Piperno, C. Farhat, and B. Larrouturou. *Partitioned procedures for the transient solution of coupled aroelastic problems Part I: Model problem, theory and two-dimensional application*, Computer methods in applied mechanics and engineering, 124, pp. 79-112, 1995.
- [6] P. Causin, J.F. Gerbeau, and F. Nobile. *Added-mass effect in the design of partitioned algorithms for fluid-structure problems*, Computer methods in applied mechanics and engineering, 194, pp.4506-4527, 2005.
- [7] C. S. Peskin. *Flow patterns around heart valves: a numerical method*. J. Comp. Phys., 10, 252-271, 1972.

References

- [8] Bletzinger K.U., R. Wuchner, Kupzok A. *A framework for stabilized partitioned analysis of thin membrane-wind interaction*, International Journal for Numerical Methods in Fluids, 54, pp. 6-8, 2007.
- [9] J. Zhang, S. Childress, A. Libchaber and M. Shelley, *Flexible filaments in a flowing soap film as a model for one-dimensional flags in a two-dimensional wind*. Nature 408, pp. 835-839, 2000.
- [10] *Computational Fluid Dynamics*,
http://en.wikipedia.org/wiki/Computational_fluid_dynamics .
- [11] Chorin, A. J., *Numerical Solution of the Navier-Stokes Equations*, Math. Comp. 22, pp. 745–762, 1968.
- [12] R. Témam, *Sur l'approximation de la solution des équations de Navier-Stokes par la méthode des pas fractionnaires*, Arch. Rational Mech. Anal. 32, pp. 135–153, 1969.
- [13] J. B. Perot, *An analysis of the fractional step method*, J. Comput. Phys., 108, pp. 51-58, 1993.
- [14] H. P. Langtangen, K.-A. Mardal, R. Winther, *Numerical methods for incompressible viscous flow*, Advances in Water Resources, Volume 25, Number 8, pp. 1125-1146, 2002.
- [15] F. H. Harlow, J. E. Welch, *Numerical Calculation of Time Dependent Viscous Incompressible Flow of Fluid with Free Surface*, The Physics of Fluids 8-12, 1965.
- [16] E. Newren, A. Fogelson, R. Guy, R. Kirby, *A comparison of implicit solvers for the immersed boundary equations*, Computer Methods in Applied Mechanics and Engineering, Vol. 197, No. 25-28, pp. 2290-2304, 2008.
- [17] A.M. Roma, C.S. Peskin, M.J. Berger, *An adaptive version of the immersed boundary method*, J. Comput. Phys. 153, 509–534, 1999.

References

- [18] L. Zhu, C. S. Peskin, *Simulation of a Flapping Flexible Filament in a Flowing Soap Film by the Immersed Boundary Method*, Journal of Computational Physics, 179-2, pp. 452-468, 2002.
- [19] Y. Kim, C. S. Peskin, *Penalty immersed boundary method for an elastic boundary with mass*, Physics of fluids 19, 2007.
- [20] Mathworks inc., *MATLAB, the language of technical computing*, <http://www.mathworks.com/products/matlab/> .
- [21] S. Bagheri, A. Mazzino, A. Bottaro, *Spontaneous symmetry breaking of a hinged flapping filament generates lift*, Phys. Rev. Lett. 109, 2012.
- [22] Z. Yu, *A DLM/FD method for fluid/flexible-body interactions*, J. Comput. Phys., 207, Issue 1, pp. 1-27, 2005.
- [23] C. H. Von Kerczek, *The instability of oscillatory plane Poiseuille flow*, Journal of Fluid Mechanics, 116, pp. 91-114, 1982.
- [24] P. J. Schmid, D. S. Henningson, *Stability and Transition in Shear Flows*, Applied Mathematical Sciences, Vol. 142, Springer, 2001.
- [25] COMSOL Inc., *COMSOL Multiphysics*, <http://www.comsol.com/> .
- [26] Z. Warhaft, *Passive scalars in turbulent flows*, Annual Rev. Fluid Mech., 32, pp. 203-240, 2000.
- [27] U. M. Ascher, S. J. Ruuth, R. J. Spiteri, *Implicit-explicit Runge-Kutta methods for time-dependent partial differential equations*, Journal of Applied Numerical Mathematics, 25, pp 151-167, 1997.
- [28] G.E. Karniadakis, M. Israeli, and S.A. Orszag. *High-order splitting methods for the incompressible Navier-Stokes equations*, J. Computational Phys., 97, pp. 414-443, 1991.

References

- [29] G. Haller, *Lagrangian structures and the rate of strain in a partition of two-dimensional turbulence*, Phys. Fluids, 13, 3365 (2001).
- [30] G. Boffetta, G. Lacorata, G. Redaelli and A. Vulpiani, *Barriers to transport: a review of different techniques*, Physica D 159, 58 (2001).

List of Figures

1.1	Picture of the first Tacoma Narrows Bridge showing the aeroelastic flutter in strong wind that will cause it to collapse. 1940.	2
1.2	Case of study.	4
1.3	Filament flapping in a flowing soapfilm due to two-way interaction [9].	7
2.1	Colocated (a) and staggered (b) grid. x -velocity component is evaluated at \leftarrow , y -velocity component at \uparrow , whereas pressure at \times	19
2.2	Staggered grid with periodic (a) and Dirichlet boundary conditions (b). The dashed line border the computational domain.	20
2.3	Example immersed boundary curve, Γ , described by the function $\mathbf{X}(s, t)$, immersed in a fluid-filled region Ω	22
2.4	Representation of the channel with its dimensions and coordinates system.	27
2.5	Unwanted vorticity due to the inlet and outlet velocity profiles. Black lines are vorticity contour-lines. $Re = 200$	28
2.6	Velocity profiles for $t/T=0.25$ (blue), $t/T=0.5$ (green), $t/T=0.75$ (red), $t/T=1$ (light blue), $L = 8$, $h = 2$, $Re = \frac{\bar{u}_{max} h \rho_{flow}}{\mu} = 200$	29
2.7	No unwanted vorticity outside the boundary layer. Black lines are vorticity contour-lines. $Re = 200$	30

List of Figures

2.8	Convergence study for various grid spacings: 1/20 (blue), 1/40 (green), 1/60 (red), 1/80 (light blue, dashed).	31
2.9	Convergence study for various grid spacings: 1/20 (blue), 1/40 (green), 1/60 (red), 1/80 (light blue, dashed). Detail. .	32
2.10	Comparison between Zu's results (left) and ours' (right) at various time-steps.	35
2.11	Comparison between Zu's results (left) and ours' (right) at various time-steps, continued.	36
2.12	Velocity profiles comparison between the pressure driven code (blue line) and the velocity driven code (red crosses). .	39
2.13	Value of \bar{u}_{1max} for γ between 0 and 100.	41
2.14	Velocity profiles comparison between the pressure driven code (blue line) and the velocity driven code (red crosses).	42
2.15	Velocity fields comparison, using COMSOL code, left, and our MATLAB code, right.	43
2.16	Velocity profiles comparison between the two codes at $y = 0.5$. In continuous lines the results from the MATLAB code, in crossed lines the ones from COMSOL. In blue the u -component, in red the v -component.	43
2.17	Velocity profiles comparison between the two codes at $x = -1$. In continuous lines the results from the MATLAB code, in crossed lines the ones from COMSOL. In blue the u -component, in red the v -component.	44
3.1	Filament free end angle θ (in radians) versus time for Reynolds number 80 (blue), 120 (green), 240 (red) and 400 (light blue).	47
3.2	Snapshot of the vorticity in the channel $Re = 400$	48
3.3	Average angle $\bar{\theta}$ versus pulsatile time period T . A bifurcation can be seen, with a peak around $T = 2.1$	50
3.4	Filament position at different times for $T = 1$ (a), $T = 2.1$ (b), $T = 3$ (c). Asymmetry is clear for $T = 2.1$	51
3.5	Filament free end path for $T = 2.1$	52
3.6	Average angle $\bar{\theta}$ versus pulsatile time period T for $L_f = 0.6$ (red line) and $L_f = 0.8$ (black line).	52

List of Figures

3.7	Average angle $\bar{\theta}$ versus $1/St$ for $L_f = 0.6$ (red line), $L_f = 0.8$ (black line) and $L_f = 1$ (blue line). The three peaks now share a similar value of St	53
3.8	The initial position and the final position of a set of passive scalars is linked by a black line, a dot marks the final position after one period. The red line denotes the filament at rest.	54
3.9	The u -velocity profiles of two channel sections at $x = -1$ (roughly corresponding to the center of the vortex) and at $x = 0$ (corresponding to the filament position) are plotted, as a continuous line and as a dash-dot line, respectively.	55
3.10	Trend of $\nabla p_x(t)$ (blue), $f_v(t)$ (red) and $f_f(t)$ (black) during 5 pulsatile time periods.	57
3.11	Left filament (dashed line) and right filament (dotted line) average angle, versus distance d between the two filaments.	59
3.12	Filaments position at different time for $d = 0.8$ (a) and $d = 2.4$ (b); filaments free-ends trajectories for $d = 0.8$ (c) and $d = 2.4$ (d).	59
3.13	The three filaments initial positions for the new simulations (b, c, d) and the original one (a).	60
3.14	Filaments free-ends distance versus time for the initial conditions in fig. 3.13a (blue), 3.13b (green), 3.13c (red) and 3.13d (light blue).	61
4.1	Average angle $\bar{\theta}$ versus $1/St$ obtained with the new code (blue line) and with the previous code (black line).	65
4.2	Average net velocity u_{net} (red line) and average angle $\bar{\theta}$ (blue line) versus $1/St$	66
4.3	Average u field (a) and v field (b) in the central area of the channel, for $T = 2.1$. The filament creates a vortex on the left side.	66
4.4	Average u field (a) and v field (b) in the central area of the channel, for $T = 0.6$. The filament creates a jet that is very slightly bent towards the left.	67

List of Figures

4.5	Average u field (a) and v field (b) in the central area of the channel, for $T = 3.6$. The filament moves the fluid towards the sides of the channel.	68
4.6	Average angle $\bar{\theta}$ versus $1/St$, for $L = 12$ (blue), $L = 6$ (green), $L = 3$ (red) and $L = 2$ (light blue).	69
4.7	Average net velocity u_{net} versus $1/St$, for $L = 12$ (blue), $L = 6$ (green), $L = 3$ (red) and $L = 2$ (light blue).	70
4.8	Absolute value of average net velocity u_{net} versus $1/St$, for $L = 12$ (blue), $L = 6$ (green), $L = 3$ (red) and $L = 2$ (light blue).	71
4.9	Average u field for $T = 0.6$ and $L = 2$ (a), $L = 3$ (b), $L = 6$ (c) and $L = 12$ (d).	73
4.10	Average v field for $T = 0.6$ and $L = 2$ (a), $L = 3$ (b), $L = 6$ (c) and $L = 12$ (d).	74
4.11	Average u field for $T = 1.5$ and $L = 2$ (a), $L = 3$ (b), $L = 6$ (c) and $L = 12$ (d).	75
4.12	Average v field for $T = 1.5$ and $L = 2$ (a), $L = 3$ (b), $L = 6$ (c) and $L = 12$ (d).	76
4.13	Average u field for $T = 2.1$ and $L = 2$ (a), $L = 3$ (b), $L = 6$ (c) and $L = 12$ (d).	77
4.14	Average v field for $T = 2.1$ and $L = 2$ (a), $L = 3$ (b), $L = 6$ (c) and $L = 12$ (d).	78
4.15	Average u field for $T = 3.6$ and $L = 2$ (a), $L = 3$ (b), $L = 6$ (c) and $L = 12$ (d).	79
4.16	Average v field for $T = 3.6$ and $L = 2$ (a), $L = 3$ (b), $L = 6$ (c) and $L = 12$ (d).	80
4.17	Streamlines path overimposed to the average u field for $L = 3$ and $T = 3.6$. The streamlines have been obtained using the Matlab function <i>stramline</i>	81
4.18	Average angle $\bar{\theta}$ as a function of $1/St$ for $2h = 2$ (red), $2h = 4$ (black, data from past simulations), $2h = 8$ (blue).	83
4.19	Net velocity u_{net} as a function of $1/St$ for $2h = 2$ (red), $2h = 4$ (black, data from past simulations), $2h = 8$ (blue).	84

List of Figures

4.20	Average u field (a) and v field (b) for $T = 0.6$ and $2h = 2$. The filament creates a jet towards the top wall of the channel.	84
4.21	Average u field for $2h = 4$ (a) and $2h = 8$ (b); $1/St = 1.875$.	85
4.22	Average angle $\bar{\theta}$ as a function of $1/St$ for $K_{beam} = 0.005$ (dotted line) and $K_{beam} = 0.05$ (dashed line).	86
4.23	Average net velocity u_{net} as a function of $1/St$ for $K_{beam} = 0.005$ (dotted line) and $K_{beam} = 0.05$ (dashed line).	87
4.24	Average u (a) and v (b) fields for $T = 2.1$ and $K_{beam} = 0.05$.	87
4.25	Average angle $\bar{\theta}$ as a function of Reynolds number Re .	88
4.26	Net velocity u_{net} as a function of Reynolds number Re .	89
4.27	Maximum difference in the behaviour of the filaments versus time.	91
4.28	Maximum difference in the behaviour of the filaments versus time, for slightly different initial positions.	92
4.29	Average angle $\bar{\theta}$ versus $1/St$ for the lower filament (blue) and the upper filament (red), compared to the case of one filament (dotted line).	93
4.30	Average net velocity u_{net} versus $1/St$ for the two filaments case (dashed line) compared to the case of one filament (dotted line).	94
4.31	Average u (a) and v (b) fields for $T = 1.5$.	94
4.32	Stramlines path overimposed to the u average field, for $T = 1.5$.	95
5.1	Trajectories of three initially close points (a); to be noticed how the points B and C quickly diverge from each other, compared to A and B. The FTLE field associated to the flow (b) outlines the vorticious structures and the vertical separating line. Courtesy of http://mmae.iit.edu/shadden/LCS-tutorial/ .	99
5.2	FTLE values for $L = 12$ and $T = 0.6$ (a), $T = 1.5$ (b), $T = 2.1$ (c), $T = 3.6$ (d). Only the central area of the domain is plotted, between $x = -2$ and $x = 2$.	101

List of Figures

5.3	FTLE values for $L = 2$ and $T = 0.6$ (<i>a</i>), $T = 1.5$ (<i>b</i>), $T = 2.1$ (<i>c</i>), $T = 3.6$ (<i>d</i>).	102
5.4	Scheme of the simplified model, the elastic filament and the pulsatile flow are not taken into account and substituted by a vertical surface force acting on the shaded rectangle. To the left and right sides of the channel periodic boundary conditions are imposed.	104
5.5	Average u and v velocity fields with streamlines obtained from the simplified model based on vertical jet and periodic boundaries (<i>a</i> and <i>c</i>), compared with the ones obtained simulating the complete system (<i>b</i> and <i>d</i>). $L = 12$.	105
5.6	Average u and v velocity fields with streamlines obtained from the simplified model based on vertical jet and periodic boundaries (<i>a</i> and <i>c</i>), compared with the ones obtained simulating the complete system (<i>b</i> and <i>d</i>). $L = 6$.	106
5.7	Average u and v velocity fields with streamlines obtained from the simplified model based on vertical jet and periodic boundaries (<i>a</i> and <i>c</i>), compared with the ones obtained simulating the complete system (<i>b</i> and <i>d</i>). $L = 3$.	107
5.8	Average u and v velocity fields with streamlines obtained from the simplified model based on vertical jet and periodic boundaries (<i>a</i> and <i>c</i>), compared with the ones obtained simulating the complete system (<i>b</i> and <i>d</i>). $L = 2$.	108

Contents

Abstract	v
Sommario	vii
1 Introduction	1
1.1 Aeroelasticity	1
1.2 Case of study	3
1.3 Filament and flow interaction	5
1.4 Symmetry breaking	7
2 Method	9
2.1 The Navier-Stokes equations	10
2.1.1 Non-dimensionalization of the Navier-Stokes Equations	11
2.2 Numerical method	13
2.2.1 The fractional step method	14
2.2.2 Staggered grid	17
2.2.3 Boundary conditions	20
2.2.4 The Immersed Boundary Method	21
2.3 Filament governing equations	24
2.4 Numerical implementation	26
2.5 Velocity driven code	26
2.5.1 Velocity profile generation	28
2.6 Grid and convergence study	31

Contents

2.7	Comparison with previous works	32
2.8	Pressure driven code	34
2.8.1	Steady flow	37
2.8.2	Pulsatile flow	38
2.9	Validation with COMSOL	41
3	Results - Velocity driven code	45
3.1	One filament	46
3.1.1	Steady-flow case	46
3.1.2	Strouhal number bifurcation	48
3.1.3	Varying the length of the filament	51
3.1.4	Asymmetry analysis	53
3.1.5	Net force and pressure gradient	56
3.2	Two filaments	58
3.2.1	Sensitivity to initial condition	60
4	Results - Pressure driven code	63
4.1	Comparison with previous code	64
4.2	Average velocity fields	65
4.3	Channel length	69
4.4	Channel height	82
4.5	Bending stiffness	85
4.6	Reynolds number	86
4.7	Multiple filaments	89
4.8	Filaments on both sides	91
5	Further analysis	97
5.1	FTLE	97
5.2	Modelling the filament	103
6	Conclusions	111
	Acknowledgements	113

